

OPTIMIZATION OF COMPLIANT JOINTS USED IN MINIATURE FOLDABLE ROBOTICS

A THESIS SUBMITTED TO
THE GRADUATE SCHOOL OF ENGINEERING AND SCIENCE
OF BILKENT UNIVERSITY
IN PARTIAL FULFILLMENT OF THE REQUIREMENTS FOR
THE DEGREE OF
MASTER OF SCIENCE
IN
MECHANICAL ENGINEERING

By
Cem Karakadıođlu
March 2018

OPTIMIZATION OF COMPLIANT JOINTS USED IN MINIATURE
FOLDABLE ROBOTICS

By Cem Karakadiođlu

March 2018

We certify that we have read this thesis and that in our opinion it is fully adequate,
in scope and in quality, as a thesis for the degree of Master of Science.

Onur Özcán(Advisor)

Ali Javili

Özgür Ünver

Approved for the Graduate School of Engineering and Science:

Ezhan Karařan
Director of the Graduate School

ABSTRACT

OPTIMIZATION OF COMPLIANT JOINTS USED IN MINIATURE FOLDABLE ROBOTICS

Cem Karakadiođlu

M.S. in Mechanical Engineering

Advisor: Onur Özcán

March 2018

In small scale and more specifically in miniature robotics applications, compliant mechanisms are highly preferred because of their advantages such as, less moving parts, friction losses, assembly time and effort, but their biggest challenge need to be addressed which is fatigue failure under cyclic loads. As the first step of this work, a new miniature, foldable, quadruped robot, MinIAQ, was developed whose legs are individually controlled by custom motors and encoders. The locomotion mechanism used in this robot is based on a simple four bar mechanism that consists of flexure joints instead of ideal revolute joints. These joints allow a single degree of freedom rotation provided by the bending of flexure members. Even though they are much more efficient and easier to make in small scale, such compliant joints suffer from fatigue failure, if subjected to long period of cyclic loads. Moreover, flexure joints and their use in robotic applications have not been modeled before using large deflection beam theory methods, which results with a limited understanding of the robot kinematics using compliant joints.

In this thesis, elliptic integral solution of nonlinear large deflections are used to model the flexure joints used in miniature compliant mechanisms. The elliptic integral kinematic solutions are verified with experimental and FEA results by using a simple leg mechanism. With varying the geometric parameters for this simple compliant mechanism, results obtained from elliptic integral solution and experiments are presented and discussed. Since flexure joints store strain energy throughout bending, they act as torsion springs. The elliptic integral kinematic solution takes this bending moment into account and the results yield accurate load capacity of the compliant mechanism. The necessary input torque to operate the compliant mechanism can also be predicted in a more accurate manner. Using the model developed, the stresses on a compliant joint can be calculated for any

mechanism. As a case study, an optimization is done for MinIAQ's compliant joints based on its geometric parameters to withstand desired number of cycles before failure.

Keywords: miniature robotics, origami robotics, foldable robotics, compliant joints, flexure hinges, compliant mechanisms, optimization.

ÖZET

MİNYATÜR KATLANABİLİR ROBOTLARDA KULLANILAN ESNEK EKLEMLERİN OPTİMİZASYONU

Cem Karakadıođlu

Makine Mühendisliđi, Yüksek Lisans

Tez Danışmanı: Onur Özcan

Mart 2018

Esnek mekanizmalar küçük ölçekli ve özellikle minyatür robotik uygulamalarında hareketli parça sayısı, sürtünme kayıpları, montaj süresi ve kolaylığı gibi avantajları nedeniyle tercih edilmektedir, ancak esnek eklemlerdeki en büyük sorun olan uzun süreli periyodik yükler altında yorulma ve kopmanın giderilmesi gerekmektedir. Bu çalışmada ilk olarak minyatür, katlanabilir, dört ayaklı, dört motordan güç alan MinIAQ robotu geliştirildi ve bu robotta bahsi geçen esnek eklemler kullanıldı. Robotun hareket mekanizması, dönel yerine esnek eklemlerin kullanıldığı basit bir dört çubuk mekanizmasına dayanmaktadır. Bu eklemler, esnek kirişin eğilmesi sayesinde tek serbestlik dereceli rotasyon sağlarlar. Küçük ölçekte çok daha verimli ve kolay montaj olsa da esnek eklemler uzun süreli periyodik harekete maruz kaldıklarında yorulmaya uğrar ve koparlar. Ayrıca, robotik uygulamalarında kullanılan esnek eklemler daha önce geniş açılı kiriş teorisi modelleri ile modellenmediğinden robot kinematığında kullanılan esnek mekanizmalar hakkında sınırlı bir anlayış vardır.

Bu tezde, minyatür esnek mekanizmalarda kullanılan esnek elemanları modellemek için lineer olmayan geniş açılı eğilmeler eliptik integral çözümleri kullanılarak modellenmiştir. Örnek olarak, basit bir esnek bacak mekanizması için eliptik integral kinematik analiz sonuçları, deneysel ve sonlu elemanlar analizi sonuçları ile karşılaştırılarak doğrulanmıştır. Bu mekanizmadaki esnek eklemin geometrik parametrelerinden bir tanesi değişirken diğerlerinin sabit kalması ile yapılan parametrik deneyler ve eliptik integral kinematik analiz sonuçları gösterilmiş ve yorumlanmıştır. Esnek eklemler eğilerek gerinim enerjisini depoladıkları için burulma yayı gibi davranırlar. Eliptik integral kinematik çözümü bu yayın içerdiği

momenti de hesaba katmakta ve böylece yük taşıma kapasitesi ve gerekli motor torku için doğru sonuçlar vermektedir. Ayrıca, bu modeli kullanarak eklem üzerindeki düzlemsel stresler de elde edilir. Örnek bir çalışma olarak, MinIAQ robotunda kullanılan esnek mekanizma için eklemlerin geometrik parametrelerine dayalı bir optimizasyon yapılmış ve istenen sayıda periyodik döngü ömrünü sağlaması sağlanmıştır.

Anahtar sözcükler: minyatür robotlar, origami robotlar, katlanabilir robotlar, esnek eklemler, esnek mekanizmalar, optimizasyon.

Acknowledgement

Firstly, and mostly, I would like to thank Prof. Onur Özcan for his endless support and encouragement throughout this work. In the three years I worked with him, he consistently allowed the work done on this thesis to be my own work and steered me in the right direction whenever I needed it. As a person very sociable and as an academic advisor he is one of the most influential person I have ever met.

Also, departmental personnel in Mechanical Engineering Machine Shop, especially Şakir Baytaroğlu and Şakir Duman, deserve a special mention for the countless helps for the experimental steps of this thesis. Without them, the work in this thesis would be impossible.

I also thank the members of the Miniature Robotics Research Group, especially Mohammad Askari for being the perfect lab-partner, Levent Dilaveroğlu, Mert Ali İhsan Kalın, Ahmet Furkan Güç for their friendship and as laboratory partners and I wish them the best in their life.

I would like to thank all my friends in Bilkent University, especially in the Mechanical Engineering department, for their support and friendship. I am very grateful for the memories and beautiful times we had together and i am looking forward for the coming ones.

Last but not the least, I would like to thank my family: my parents and to my brother for their endless belief in me, and their support during my whole life. They provided me with unfailing support and continuous encouragement and especially through the process of researching and writing this thesis and I cannot be grateful enough.

I also thank to TÜBİTAK for financially supporting this research work under 1001 Programme (Grant No. 215M366).

Contents

- 1 Introduction** **1**
 - 1.1 Objectives and Contributions of the Thesis 1
 - 1.2 Organization of the Thesis 2

- 2 Design and Manufacturing of MinIAQ** **5**
 - 2.1 Historical Background of Miniature Foldable Robots 5
 - 2.2 Design of MinIAQ 7
 - 2.2.1 Material Selection 8
 - 2.2.2 Actuation Mechanism and Leg Design 9
 - 2.2.3 Design Elements for Higher Frame Stiffness and Rigidity . 11
 - 2.2.4 Design of Electronics and PCB 14
 - 2.2.5 Custom Encoder Design and Control Input Signal 16
 - 2.3 Fabrication and Assembly 17
 - 2.3.1 Fabrication of Electronics and PCB 17

2.3.2	Fabrication and Assembly of the Robot	19
2.4	Improved Latest Version, MinIAQ-II	21
2.4.1	Linkages, Flexure Joints and the Main Body Design	21
2.4.2	Locomotion Mechanism Optimization	23
2.4.3	Fixed-Angle Knee Joint Design	23
2.4.4	Performance of MinIAQ-II	25
2.5	C-Quad and C-Shaped Wheel Design	28
2.5.1	Main Body Design	29
2.5.2	C-Shaped Wheeled Leg Design	30
2.5.3	Performance of C-Quad	32
3	Compliant Joints and Beam Theory	34
3.1	Advantages of Compliant Joints	34
3.2	Limitations of Compliant Joints	35
3.3	Linear Elastic Small Deflections	36
3.3.1	Beam with End Load	36
3.3.2	Beam with End Moment	38
3.3.3	Beam with Vertical End Force and Moment Loads at the Free End	38
3.4	Nonlinear Large Deflections	39

3.4.1	Historical Background of Nonlinear Large Deflections . . .	39
3.4.2	Elliptic Integrals	40
3.4.3	Beam with Moment at the Free End	42
3.4.4	Beam with Combined Force Load at the Free End	43
3.4.5	Beam with Combined Force and Moment Loads	46
3.4.6	Beam with Initial Curvature	51
3.5	Large vs. Small Deflections	52
4	Kinematic Model of Rigid Linkage and Compliant Joint Mechanisms Based on Large Deflection Elliptic Integrals	54
4.1	Leg Mechanism Used in Experiments	54
4.2	MinIAQ-I Leg Mechanism	59
4.3	MinIAQ-II Leg Mechanism	63
5	Fatigue Failure Prevention For Compliant Mechanisms	67
5.1	Principal Stresses	67
5.2	Fatigue Failure	70
5.3	Fatigue Life Method	71
5.3.1	Stress Life Method of Polymers	71
5.4	Fluctuating Stresses	74
5.4.1	Fatigue Failure Criteria for Fluctuating Stresses	75

<i>CONTENTS</i>	xi
5.4.2 Fatigue Failure Criteria for Fluctuating Stresses of Polymers	77
5.5 Combination of Loading Modes	78
6 Optimization	80
6.1 Optimization Algorithm	80
6.2 Optimization Problem	81
6.2.1 MinIAQ-I Mechanism Optimization	82
7 Experimental Results and Discussion	85
7.1 Parametric Joint Experiments	85
7.1.1 Thickness	86
7.1.2 Length	88
7.1.3 Width	90
7.1.4 Vertical Point Load	91
7.2 Torque Limit Experiment	92
7.3 Trajectory Paths of Compliant, Small-Length Flexure and Revolute Joint Mechanisms	94
8 Conclusion and Future Work	95
Bibliography	105
A Optimized Parameters of MinIAQ Mechanism	106

A.1 MinIAQ-I Optimization	106
A.2 MinIAQ-II Optimization	107

List of Figures

2.1	Foldable miniature quadruped robot, MinIAQ.	8
2.2	Various colors of PET sheets used in MinIAQ as structural material.	9
2.3	Gait trajectory of the cam-driven four-bar mechanism with a detail view of the fundamental linkage and joint design in foldable robots. Inset shows hollow triangular beams with flexure joints.	10
2.4	(a) Unfolded crease pattern of two parallel T-shaped folds (green) with embedded U-shaped fasteners (red). The black dashed lines represent the folding lines. (b) Folded structure of T-folds with their U-shaped extension tabs fastened into a common slot in between. (c) Side view of the folded structure showing how the fasteners pass underneath the T-folds and lock into the slot from below.	12
2.5	A sectional view of MinIAQ’s main frame with tight fit motor housing using a pair of parallel T-folds and an IR sensor housing on the outer T-fold next to motors. •Green: T-shaped folds. •Red: Double-sided coupled locking tabs to fasten T-fold faces. •Yellow: T-fold end extension fasteners to restrict torsional twist and sliding dislocations (Holes are used to temporarily insert pins during assembly). •Pink: T-fold top extension fasteners to restrict torsional twist and sliding dislocations. •Blue: U-shaped lockable fasteners to form I-beam like structures from T-folds.	13

2.6 (a) Unfolded structure of two T-folds with motor and sensor housings. The black dashed lines represent the folding lines. (b) Folded structure of T-folds with motor and sensor in place. 14

2.7 CadSoft Eagle drawing of the PCBs used in MinIAQ: (a) Inner flexible PCB for sensor connections and power regulation and distribution. (b) Main controller PCB for controls and driving the actuators. Red color lines show traces on top layer and blue color lines show traces on bottom layer. The labeled numbers indicate the soldering position of components and connectors described in text. 15

2.8 (a) Single black band cam shaft encoder. (b) 3D cam shaft encoder. (c) A 3D encoder analog output signal with 28 sample points detected per cycle for the controller input. 17

2.9 (a) PCB without any components soldered. (b) PCB without Arduino Microcontroller soldered. (c) PCBs final state after all components soldered, cut and folded ready to be inserted inside the robot. 18

2.10 The 2D unfolded technical drawing file used for laser cutting where dashed red lines represent the folding edges and continuous blue lines show full cuts. The labeled parts are explained in detail in the text. 20

2.11 MinIAQ-II: A foldable miniature quadruped robot with independent leg actuation and improved mechanism design. 22

2.12 (a) Original locomotion mechanism trajectory of MinIAQ. (b) Optimized mechanism trajectory of MinIAQ-II. 24

2.13	A schematic representation of the unfolded to folded structure of the new leg design. The knee shaped triangular beam link consists of two triangular beams and a fixed angle joint that is locked in place with the help of the inclined fastener.	25
2.14	Comparison between forward leg trajectory for ideal trot gait simulation of MinIAQ-II (top) and MinIAQ (bottom).	26
2.15	Estimation of pitch and roll angles variations from simulation at 3 Hz for both versions of MinIAQ. The snapshots on the right show the maximum recorded pitch and roll from actual tests.	27
2.16	Snapshots of MinIAQ-II's improved maneuverability during a zero-radius in-position turning test at 3 Hz drive frequency.	28
2.17	The foldable, miniature, C-shaped-legged quadruped, C-Quad. . .	29
2.18	2D unfolded technical drawing of the body where blue lines represent the full cuts and red lines represent the folding lines.	30
2.19	(a) The folded C-shaped leg. (b) Design iterations of C-shaped legs.	31
2.20	2D unfolded technical drawing of a C-shaped leg design.	31
2.21	Controlled steering of the C-Quad.	32
2.22	C-Quad locomotion over obstacle of 2.5 cm.	33
3.1	Force acting to the free end of cantilever beam with small deflections.	36
3.2	Moment acting to the free end of cantilever beam with small deflections.	38
3.3	Force and Moment acting to the free end of cantilever beam with small deflections.	38

3.4	Moment acting to the free end of cantilever beam with large deflections.	42
3.5	Combined force loads acting to the free end of cantilever beam with large deflections.	43
3.6	Combined force and moment loads acting to the free end of cantilever beam with large deflections.	46
3.7	Initially curved beam with combined force and moment loads acting at the free end of cantilever beam.	51
3.8	End slope of joint, θ , versus vertical end load, P , for small and large deflection models. Joint parameters: $L = 2$ mm, $b = 6$ mm, $t = 25$ μ m, $M_0 = 0$ N m and $P = 0.001$ N to 0.02 N.	53
4.1	A single leg compliant mechanism used in experiments to verify kinematic analysis.	55
4.2	(a) Free body diagram of rigid link CD. (b) Free body diagram of compliant joint. (c) Actuator link connected to motor, link AE.	55
4.3	A single leg compliant mechanism with dashed lines to clarify trigonometric relation for prismatic joint.	56
4.4	A single leg compliant mechanism used in experiments to verify kinematic analysis.	57
4.5	Deflection angle of joint (θ) versus vertical end load (P) experimental average error (black), and kinematic analysis of large deflection elliptic solution (red).	58
4.6	Deflection curves of beam for linear elastic (blue) and nonlinear large (black) deflection models. Tip position is shown in red circles which is obtained from experiments.	58

4.7	Compliant mechanism used in MinIAQ-I.	59
4.8	(a) Free body diagram of first compliant joint. (b) Free body diagram of second compliant joint. (c) Free body diagram of link BC. (d) Free body diagram of link DF.	60
4.9	Free body diagram of the actuator link connected to motor, link GI. 61	
4.10	Input crank angle (ψ) versus joint deflections (θ_1 and θ_2) comparison for large deflection kinematic solution and FEA results. . . .	62
4.11	Input crank angle (ψ) versus joint end forces ($P1$, $nP1$, $P2$ and $nP2$) for large deflection kinematic solution.	62
4.12	Input crank angle (ψ) versus moments (M_{01} , M_{02}) and input crank torque (T_{in}) for large deflection kinematic solution.	63
4.13	Compliant mechanism used in MinIAQ-II.	64
4.14	(a) Free body diagram of first compliant joint. (b) Free body diagram of second compliant joint. (c) Free body diagram of link BC. (d) Free body diagram of link DF.	65
5.1	2D planar stress element to 2D principal stress element transformation.	69
5.2	Variation of bending stress subjected on PET sheet joint material used in early stages of MinIAQ-I design is a good example of cyclic softening.	73
5.3	Estimated S-N diagram for Kapton [®] polyimide film with parameters $\sigma_u = 231MPa$, $\sigma_e = 50MPa$, $C_n = 0.051$ and $m_n = 0.28$. . .	74

5.4 Time-stress reversal examples. (a) Completely reversed sinusoidal stress. (b and c) Sinusoidal fluctuating stresses with different mean stress (σ_m). 75

5.5 Modified Goodman diagram used to predict fatigue failure in fluctuating stresses. 76

5.6 Fatigue diagram for various criteria methods to relate mean stresses (σ_m) to stress amplitude (σ_a) where σ_y is yield strength, σ_e is endurance limit, σ_{ult} is ultimate strength. **Turquoise:** Infinite life area, **Pink:** Yielding area and **Grey:** Finite life area 77

5.7 Estimated mean stress effect on the S-N diagram for Kapton[®] polyimide film for different mean stress (σ_m) and stress ratios (R) with Parameters $\sigma_u = 231MPa$, $\sigma_e = 50MPa$, $C_n = 0.051$ and $m_n = 0.28$ 78

6.1 (a) Input small-length flexural joint mechanism. (b) Output optimized compliant joint mechanism. 84

6.2 Optimization convergence examples for MinIAQ-I mechanism for different thickness and stress amplitudes. (a) 75 μm (b) 100 μm Kapton[®] PI film. 84

7.1 Experiment setup used to obtain vertical force readings with the deflection of leg. 86

7.2 Vertical force (P) versus end slope (θ_0) for thicknesses of 25, 50, 75 and 125 μm Kapton[®] PI film. 87

7.3 Input crank torque (T_{in}) versus end slope (θ_0) for thicknesses of 25, 50, 75 and 125 μm Kapton[®] PI film. 88

7.4	Vertical force (P) versus end slope (θ_0) for 2, 3, 4, 6 and 12 mm long Kapton [®] PI film.	89
7.5	Input crank torque (T_{in}) versus end slope (θ_0) for 2, 3, 4, 6 and 12 mm long Kapton [®] PI film.	89
7.6	Vertical force (P) versus end slope (θ_0) for 2, 4, 6, 8 and 10 mm wide Kapton [®] PI film.	90
7.7	Input crank torque (T_{in}) versus end slope (θ_0) for 2, 4, 6, 8 and 10 mm wide Kapton [®] PI film.	90
7.8	Vertical force (P) versus end slope (θ_0) for vertical loads of 0.76, 3.08, 6.73 and 10.52 grams acting on the tip of the leg.	91
7.9	Input crank torque (T_{in}) versus end slope (θ_0) for vertical loads of 0.76, 3.08, 6.73 and 10.52 grams acting on the tip of the leg.	92
7.10	Limiting input crank torque experiment setup. (a) No load attached on the tip of the leg. (b) Vertical load attached on the tip of the leg.	92
7.11	MinIAQ-I trajectory paths for compliant joint, small-length flexural joint and revolute joint kinematic analysis methods.	94
A.1	Input mechanism of MinIAQ-1.	106
A.2	Optimized compliant mechanism of MinIAQ-1.	107
A.3	Input mechanism of MinIAQ-2.	108
A.4	Optimized compliant mechanism of MinIAQ-2.	109

List of Tables

7.1	Torque limit experimental versus large deflection kinematic prediction results when no loads acting to tip of the leg (see Figures 4.1 and 7.10(a)).	93
7.2	Torque limit experimental versus large deflection kinematic prediction results when vertical force is applied on the tip of the leg ($Dy = 1.7g$ see Figures 4.1 and 7.10(b)).	93

Chapter 1

Introduction

1.1 Objectives and Contributions of the Thesis

The first contribution of the work on this thesis is the design, development, and basic operation of MinIAQ-I, MinIAQ-II and C-Quad, which are origami-inspired, printable, miniature quadruped robots. Instead of employing multi-layer composite structures similar to most micro-robotic fabrication techniques, these robots are fabricated from a single A4 PET sheet. MinIAQ-I and MinIAQ-II leg mechanisms are designed as compliant mechanisms based on simple four bar mechanism and C-Quad is designed based on C-shaped wheeled legs that are separately manufactured by folding C-shaped wheels. Each four legs of these robots are driven and controlled separately by DC motors and encoders enabling gait modification and higher degree of freedom on controlling the motion. The origami inspired fabrication technique is a fast and inexpensive method to make complex 3D robotic structures through successive folding of laser-machined sheets. However, there is still a need for improvement in modulating and extending the design standards of origami robots. In an effort to addressing this need, the primitive foldable design patterns of MinIAQ for higher structural integrity and rigidity are presented in detail.

The foremost contribution of this thesis is the optimization of the compliant joints used in but not limited to the miniature robots discussed above. The flexure joints used in compliant mechanisms are modeled as cantilever beams fixed from one end and subjected to combined end loads and moments based on nonlinear large deflections. There exists several methods to predict the deflection of the cantilever beams, such as FEA methods, but they are time consuming and hard to solve based on optimization problem. In this work, elliptic integrals are used to solve the large deflections of Bernoulli–Euler cantilever beams, which are easier to converge to a solution and have high accuracy for thin beams. The biggest challenge in using a compliant joint in these mechanisms is the fatigue failure of these flexure members. The fatigue failure methods are investigated for combined loading conditions, then the compliant mechanisms used in MinIAQ are optimized for desired output trajectory and fatigue cycle life. Using the work in this thesis one can obtain the maximum load capacity, input motor torque required to actuate the loaded mechanism and number of cycles before failure of a compliant mechanism.

1.2 Organization of the Thesis

Chapter 2 focuses on the design of MinIAQ, the miniature quadruped, which was inspired by origami, the traditional Japanese art of subsequent folding of a 2D sheet into a 3D functional structure. Folding is an efficient and simple approach to planar fabrication of flexible 3D structures and can be employed as an alternative fabrication method to traditional machining or complex composite manufacturing processes. Yet, it is not extensively utilized in engineering fields due to its limiting factors such as planar design constraints, material selection limitations, and relatively complex folding and assembly tasks involved.

Chapter 3 introduces the beam theories used to model compliant joints. Firstly, advantages and challenges in using compliant joints are explained. Then, linear elastic beam deflection models are derived, which give accurate results for small

deflections. Since compliant joints used in miniature robotics undergo large deflections, linear elastic beam theories yield high error. For this reason, nonlinear large deflection methods are used to model joints in compliant mechanisms. A brief historical background survey about nonlinear large deflection beam theories is provided based on different methods. Among the readily available methods, elliptic integral solution for nonlinear large deflections is chosen for different loading conditions.

In **Chapter 4** kinematic model of compliant mechanisms will be presented, which has a different approach than traditional revolute joint kinematic analysis and harder to solve. In order to model the kinematics of a compliant mechanism, the nonlinear large deflection elliptic integral solutions introduced in Chapter 3 are combined with static equilibrium equations of rigid linkages and loop closure equations based on free body diagrams of a compliant mechanism. The first mechanism introduced in this chapter is relatively simple four bar mechanism, which has a single compliant joint, used to verify the validity of results obtained in large deflection elliptic integral solution. The vertical force obtained from large deflection elliptic integral kinematic solution of this simple mechanism is verified with Comsol FEA and experimental results. Finally, large deflection elliptic integral kinematic analysis is done based on compliant mechanisms used in MinIAQ-I and MinIAQ-II and output trajectories are obtained. The large deflection elliptic integral kinematic analysis and FEA results for end slopes and forces acting on compliant joints are presented.

Chapter 5 investigates the methods to prevent the fatigue failure of compliant mechanisms. First the planar stresses subjected to a compliant joint are discussed for different loading conditions, then principal stress is explained which are key elements in dealing with fatigue failure for combined loads. A fatigue-life method will be presented that provides an insight on stress-life cycle for polymers based on mathematical formulations.

Chapter 6 provides an optimization method for joints used in compliant mechanisms. First, an appropriate optimization algorithm is chosen from MatLab

optimization toolbox. `fminimax` multi-objective nonlinear constraint optimization function is used. Then, optimization problem is defined for MinIAQ-I leg mechanism and optimization is conducted for this mechanism.

In **Chapter 7**, experimental results are presented for the effect of changing geometric parameters of a compliant joint. Results are plotted for varying a single geometric parameter while other parameters are kept constant. Discussions are made for effect of each parameter on force acting on the leg and input torque required to drive the mechanism.

Chapter 8 is a summary of this thesis and provides the conclusion and outlook of the current work, including any improvements possible and future works for the content of this thesis.

Chapter 2

Design and Manufacturing of MinIAQ

In this chapter, design, development, electronics and basic operation of MinIAQ, which is inspired by origami art, the traditional Japanese art of subsequent folding of a 2D sheet into a 3D functional structure is presented. Then, MinIAQ-II, which has an improved locomotion design is presented and its improvements are explained. Finally, C-Quad, which has C-shaped wheels, wheeled legs, instead of legs is introduced and its benefits are explained.

2.1 Historical Background of Miniature Foldable Robots

Miniature and small scale robotic applications offer solutions to accomplish low cost and high modularity that macro robotic applications generally remain incapable, which additionally limits the widespread utilization of macro scale robots. Moreover, unlike macro scale, miniature robotic systems have important advantages such as, nimbler locomotion, high maneuverability abilities that allow them to access confined and hazardous spaces [1]. On the other hand, miniature scale

applications generally have locomotion, slip, design and failure limitations. Flexure joints used in compliant mechanisms have a maximum allowable deflection, while revolute joints can rotate unlimited number of times, so these mechanisms have limited rotation range and reachability. Since rotation of these joints comes from bending of flexure segments, bending stresses may cause failure under long period of cyclic loads. Also a proper design is needed to assemble such mechanism to achieve rigidity and integrity to carry desired loads.

In literature there exists several methods for miniature robotic design and fabrication such as MEMS [2, 3], cutting laminate of carbon fiber composite and thin polyimide films (SCM), 3D printing [4] and folding [5–7], such as used in RoACH [8] and HAMR [9].

Kirigami, a subset of origami involving out-of-plane cuts [10], inspired developing a new planar fabrication process for micro-robotic systems which is often referred to as printable, foldable, or print-and-fold robotics [11]. In this context, the term printing corresponds to engraving cut and fold patterns on sheets by utilizing a laser cutter or even by patterning 2D printable layers using 3D printers [12]. One of the advantages of printable or foldable robotics is that all transmission, flexure joints, and customizations can be embedded into a single 2D design, which not only is cheap and time-saving, but also eases the fabrication, assembly, and future design enhancements. Following the early works reported in [13], this technology was first developed by researchers in Harvard University and MIT [11] and was later adapted by many researchers in designing their miniature grasping [14, 15], flying [16], and worm type robots [17, 18] as well as some enhanced legged versions [19–21]. The method was further developed in [22] by implementing embedded circuitry through shape-memory composite planar designs to enable self-folding of the robots.

Despite the recent advancements in foldable robotics, there exists space for development in standardizing the hierarchical design process and folding elements to obtain high structural integrity and rigidity in a robotic platform. There aren't many examples of complex foldable structures and most of the works rely on rather simple designs. This chapter aims to design MinIAQ in a way to show

the capability of this fabrication method for making complex robots and set a paradigm for designing more complicated foldable structures with higher structural integrity and rigidity.

MinIAQ is a quadruped foldable legged robot made from a single sheet of thin A4-sized PET film. The stiffening structures used in the robot and the overall unfolded structure design are not presented before, and thus this is one of the contributions done to the literature. As another contribution of this work, each leg is designed to be actuated individually by a small DC motor. This is different from previous miniature robots where one or two actuators are shared between legs to provide easier synchronous leg motion. Despite higher power consumption and greater challenge in phase synchronization control at such small scale, the idea of using one actuator per leg is to independently control the legs, achieve better maneuverability and in-place sharp turning, and have higher degree of freedom on controlling the overall robot's motion.

The main reason in designing a robot with individually actuated legs is not to claim that it is better or easier to control than miniature robots with coupled actuation but to enable gait modification during locomotion in a small scale for future studies. As an additional contribution, custom absolute encoders are designed for having small-yet-sensorless actuators to generate a single predefined signal that could be used to estimate both the speed and position of each leg and synchronize the legs accordingly. Even though the current version is a quadruped, the robot can be modified to have 'n' legs, if 'n' of these individually actuated legs are put together on a single body.

2.2 Design of MinIAQ

MinIAQ is fabricated from a single sheet of thin A4-sized PET film. Its legs are designed based on a simple four-bar locomotion mechanism that is embedded within its planar design. Each leg is actuated and controlled individually by separate DC motors enabling gait modification and higher degree of freedom on

controlling the motion (see Figure 2.1).

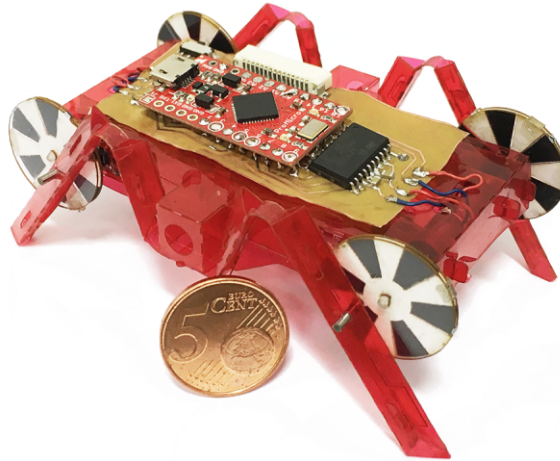


Figure 2.1: Foldable miniature quadruped robot, MinIAQ.

The origami-inspired fabrication technique is a fast and inexpensive method to make complex 3D robotic structures through successive-folding of laser-machined sheets. However, there is still a need for improvement in modulating and extending the design standards of origami robots. In an effort to addressing this need, the primitive foldable design patterns of MinIAQ for higher structural integrity and rigidity are presented in detail.

The initial version of the robot takes less than two hours to be cut and assembled and weighs about 23 grams where 3.5 grams is the weight of its body, 7.5 grams is its motors and encoders, 5 grams is its battery, and about 7 grams is its current on-board electronics and sensors. The robot is capable of running about 30 minutes on a single fully charged 150mAh single cell LiPo battery. Using the feedback signals from the custom encoders, MinIAQ can perform a trot gait with a speed of approximately 0.65 Bodylengths/sec, or equivalently 7.5 cm/s.

2.2.1 Material Selection

In designing MinIAQ, the aim was to make an embedded single-piece crease pattern for ease of manufacturing. In order to select a proper material in terms

of flexibility, rigidity, and joint durability, 100, 250 and 500 micrometer thick PET sheets were selected as possible candidates, see Figure 2.2. During the manufacturing process, it was observed that the thinner sheets were easier to cut, fold and assemble. Despite the fact that rigidity increases with film thickness, it becomes harder to make folds and shape corners, especially by scaling down to smaller scale folds. In addition, the thicker sheets had lower joint performance since the joints made of thicker sheets would plastically deform and break much sooner than the thin sheets, which makes sense according to beam theories that will be explained in Chapter 3. Alternative structural materials can also be used to achieve enhanced mechanical properties such as increased stiffness or higher joint cycle life. Chapter 6 deeply focuses on these issues to achieve higher joint life cycle.



Figure 2.2: Various colors of PET sheets used in MinIAQ as structural material.

2.2.2 Actuation Mechanism and Leg Design

In MinIAQ, rigid triangular beams and compliant flexure joints are used as the primitive components of the locomotion mechanism (Figure 2.3). Rigid triangular beams are achieved by folding the sheets and locking into triangular prism shape. In this configuration, the beam's rigidity is dependent on its length, width, thickness and Young's modulus of material used [23]. Flexure joints are kinematic components that allow rotation in 1 DOF between two rigid links with the help

of sheet flexibility. Even though flexure joints are very useful components for miniature scale compliant mechanisms, they suffer from fatigue failure [24]. By optimizing the joint width, length and maximum deflection angle, life cycle of the flexure joints can be increased further by distributing the load more uniformly and reducing the stress at the joints. At the time that the initial version of the MinIAQ was designed, the joints were not optimized yet, but this issue will be dealt later on Chapter 6.

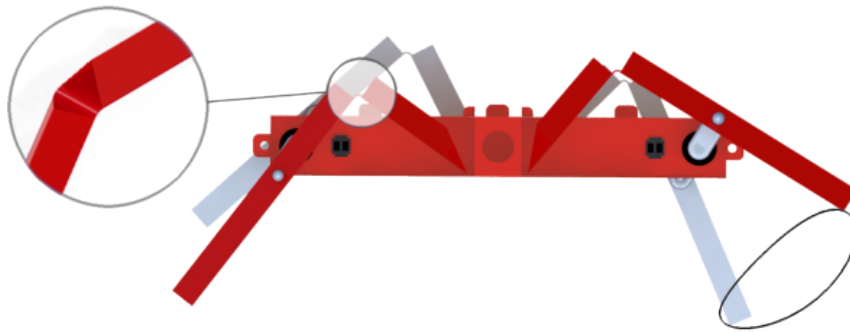


Figure 2.3: Gait trajectory of the cam-driven four-bar mechanism with a detail view of the fundamental linkage and joint design in foldable robots. Inset shows hollow triangular beams with flexure joints.

The first step towards a legged robot design and perhaps the foremost important stage is the design of its actuation mechanism. In foldable robotics context, it is quite challenging to integrate a mechanism into the design which has good locomotion trajectory while having simple unfolded form. The flexure joints in foldable designs have limited degree of rotation, meaning that the links should not be bent very large with respect to each other so as to prevent shear at the joints [25]. This issue further aggregates the challenge in mechanism selection.

For MinIAQ's legs, a simple four-bar cam-driven mechanism was designed and synthesized by altering the dimension of the leg, position of the joints and radius of the cam (input crank link) in order to obtain an acceptable gait path as shown by the trajectory in Figure 2.3. The selected four-bar is not optimal performance-wise; it has relatively poor gait path and stride length. However, its simplicity was favored over complexity for the initial MinIAQ version due to ease of planar design and assembly. In improved version of MinIAQ, a more optimal transmission is used, which will be introduced in Section 2.4 of this chapter.

2.2.3 Design Elements for Higher Frame Stiffness and Rigidity

A very important parameter influencing the payload capacity of a foldable robot is its structural integrity. Due to having a thin flexible sheet as the base material, certain primitive folded structures were required to make the frame and linkages hold their shapes. These primitive folded components set the basic design rules and act as subsets of any complex structure. As discussed, the legs were designed according to the hollow triangular linkage and perforated joint structures studied in the literature by [19, 23, 26, 27].

As an addition to the foldable robot design library in the literature, newly introduced T-shaped folds are used as fundamental elements in MinIAQ contributing to its high structural integrity (shown in green in Figure 2.4, 2.5, and 2.6). They act as out of plane extensions which not only stiffen the main robotic frame, but also can restrict transverse bending, buckling and bellling of the robot. To lock the T-shaped folds in place, gluing or stitching can be a solution, but they are practically hard to implement for small parts and tiny extensions. The better approach is to utilize tab-and-slot fasteners to tightly lock the parts into each other.

On every T-fold, certain tabs are placed on one of the faces that locks into a slot. To firmly fix the position of a pair of T-folds and hold them in place with respect to each other, the tabs on each T-fold should be fastened into a single slot (see Figure 2.4(a)). Once the tabs are inserted through the slot, sides of the tabs are bent into U-shape to achieve proper locking in place as seen in Figure 2.4(a). The visual representation of locking mechanism for T-folds can be seen in Figure 2.5 with red color. Note that a total of six (three on each side), equally spaced, double-sided T-fold fasteners are used on the main frame of MinIAQ. By using such fasteners, T-fold assemblies can be completed in minutes without needing any extra effort or hand skill.

In order to limit robot frame's twisting under torsion and prevent unwanted

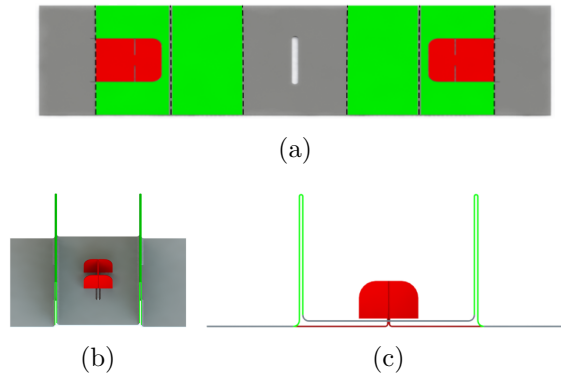


Figure 2.4: (a) Unfolded crease pattern of two parallel T-shaped folds (green) with embedded U-shaped fasteners (red). The black dashed lines represent the folding lines. (b) Folded structure of T-folds with their U-shaped extension tabs fastened into a common slot in between. (c) Side view of the folded structure showing how the fasteners pass underneath the T-folds and lock into the slot from below.

dislocations, extension tabs (shown in yellow in Figure 2.5) were made at the ends of the T-folds, which are tightly fitted through a slot. The friction between the extension tab and slot has enough locking force to prevent sliding of tabs due to torsion and any movement along the transverse direction. These tabs can be converted to U-shaped lockable tabs introduced in the next paragraph to achieve better locking but with slightly harder assembly.

To further improve the bending stiffness of the main frame, the T-folds located within the body are attached to the top cover of the main frame using two types of fasteners. The first type is the tight fit extension tabs and slots described in preceding paragraph that prevent buckling of T-folds by tight fitting the tabs on the upper side of the T-folds into a slot on the top cover (Figure 2.5 - pink). The second type of fastener used to stiffen the main frame is U-shaped lockable tabs, which are practically tabs with foldable extensions on both sides that form a U-shape after inserting through a slot and folding the extensions inwards by 90° (Figure 2.5 - blue). By fastening the U-shaped tabs on the T-folds through the slots placed on the top cover, fixing the T-folds rigidly in place is achieved that they act as I-beam like structures. Therefore, by using ‘n’ number of T-folds within the structure and using tabs and U-shaped fasteners, the main frame

technically becomes a rigid body supported by ‘n’ number of I-beams.

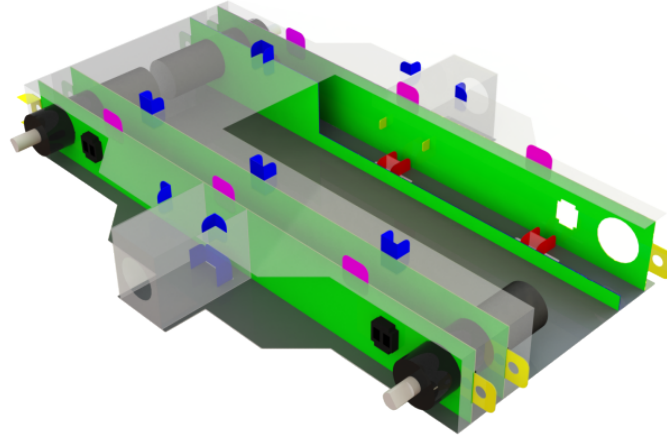


Figure 2.5: A sectional view of MinIAQ’s main frame with tight fit motor housing using a pair of parallel T-folds and an IR sensor housing on the outer T-fold next to motors. ●**Green:** T-shaped folds. ●**Red:** Double-sided coupled locking tabs to fasten T-fold faces. ●**Yellow:** T-fold end extension fasteners to restrict torsional twist and sliding dislocations (Holes are used to temporarily insert pins during assembly). ●**Pink:** T-fold top extension fasteners to restrict torsional twist and sliding dislocations. ●**Blue:** U-shaped lockable fasteners to form I-beam like structures from T-folds.

Another challenging stage in the design was to find a folded structure to tightly hold the DC motors in place within the frame. Note that while using an external housing could be a solution, in foldable robotics the aim is to avoid using separate parts or materials as much as possible and restrict the work to a single uniform crease pattern. This was solved by using two sets of parallel T-folds on each side of the main frame and placing tight circular housings for the DC motors through each pair. T-folds increased the rigidity of the frame and also held the motors strongly in place. Thus, due to their out-of-plane structure, T-folds are very suitable for making housings such that any type of motor can be properly mounted onto the frame by a pair of parallel T-folds. Since MinIAQ is designed to have individual leg actuation, four T-folds were embedded into the design to enable four motor housings, one at each corner of the frame (Figure 2.5 and 2.6).

The rotational motion of the motors was transmitted to the legs with a cam shaft made of a thicker sheet film. Note that since the cam shaft, i.e. the crank link of the four-bar, has to rotate 360° in plane, it is very hard and complex, if not

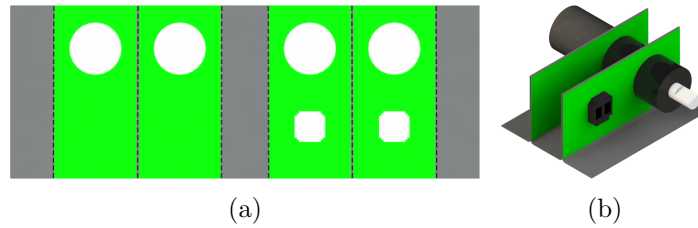


Figure 2.6: (a) Unfolded structure of two T-folds with motor and sensor housings. The black dashed lines represent the folding lines. (b) Folded structure of T-folds with motor and sensor in place.

impossible, to achieve this with an origami flexure joint structure. Thus, the cam shafts were made and assembled from separate sheets and pins. These elements on the MinIAQ are the only mechanical structures on the robot that have to be manufactured separately. The cam shafts also serve as elements used in control and synchronization of the robot legs via IR sensors which are explained in detail in Section 2.2.5 of this chapter. Placing the sensors on the body is achieved by making a small housing next to the motors and inserting them within the outer T-folds. A small rectangular opening for the emitter and receiver on the outer side of the T-fold helps holding the sensor in place by preventing it from sliding inside the T-fold that can be seen in Figure 2.6.

2.2.4 Design of Electronics and PCB

With the intention of independent actuation of each leg, MinIAQ is designed with four very small and lightweight (approx. 1.25 grams each) motors (Pololu, Sub-Micro Plastic Planetary Gearmotor). The major drawback of using these motors is the lack of any type of built-in encoders. For this reason, it is necessary to design a feedback controller for each motor to properly adjust the speed and position of each leg. Therefore, small IR sensors are selected to house next to the motors and custom cam encoders with black and white stripes are made and attached to the motors.

The IR sensors need three connections (power, ground and signal) to operate in order to provide feedback signal to the controller. To avoid complex wiring

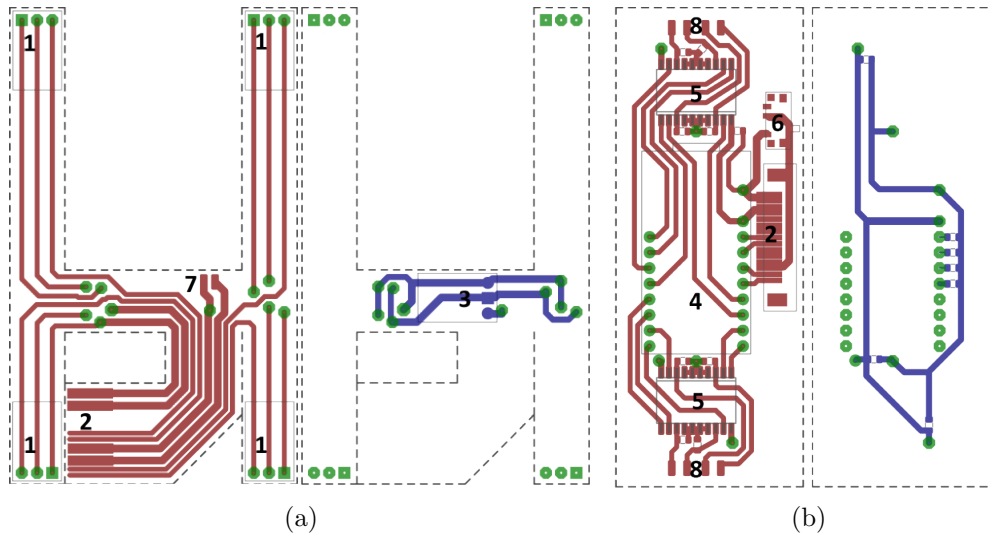


Figure 2.7: CadSoft Eagle drawing of the PCBs used in MinIAQ: (a) Inner flexible PCB for sensor connections and power regulation and distribution. (b) Main controller PCB for controls and driving the actuators. Red color lines show traces on top layer and blue color lines show traces on bottom layer. The labeled numbers indicate the soldering position of components and connectors described in text.

and soldering of each sensor, a flexible PCB that will be located inside the body frame is designed, which can be cut into shape and extended to the sensors. This inner flexible board powers every sensor and transfers the signals to the controller (see Figure 2.7(a)). A copper clad polyimide flexible sheet is chosen as the PCB material (Dupont, Pyralux). The inner flexible PCB interconnects the two sensor couples by two 90 degree folds (Figure 2.7-1). Signal and power traces of the inner PCB are combined and bundled in a foldable extension that comes out of the top frame, to be connected to the main controller PCB, which is located on top of the robot, through a socket (Figure 2.7-2).

To run the robot, a single cell 3.7 V, 150 mAh LiPo battery is used and it is soldered from the pads seen in Figure 2.7-7. Then its voltage is boosted to 5 V with a step-up regulator located on the inner flexible PCB (Figure 2.7-3)) to power the sensors, the motor drivers, and the microcontroller.

The Arduino Pro Micro microcontroller (Figure 2.7-4) is placed on the main controller PCB located on top of the main frame, along with two L293DD motor

driver ICs (Figure 2.7-5), 16 SMT capacitors, on-off slider switch (Figure 2.7-6) and an FFC/FPC socket (Figure 2.7-2) to connect the inner flexible PCB to the main controller PCB. The main controller PCB can be seen in Figure 2.7. The inner flexible PCB distributes the regulated 5 V power to the sensors and the main controller PCB and also transfers the signals generated by the sensors. Finally each motor is soldered via the pads placed on top and bottom of the main PCB (Figure 2.7-8).

2.2.5 Custom Encoder Design and Control Input Signal

Considering the choice of having four actuators on board, one of the smallest and lightest available DC motors was selected as the actuator. However, these motors lack extension shafts for encoder attachments. For determination and control of both speed and position of each leg, small analog IR sensors were selected as MinIAQ's only sensing device and were embedded into the design next to the motors as explained in Section 2.2.3 of this chapter.

An absolute encoder with a single black band was designed and integrated with the actuation mechanism cam-shaft (crank linkage) as shown in Figure 2.8(a). The output signal of this cam resembles a single peak per cycle signal where for a walking motion with nominal frequency of about 2.5 to 3 Hz, it does not provide more than a few discrete inputs in each cycle to the controller. Thus, during walking trials, it was observed that the speed of the control loop was insufficient to compensate for the highly varying loads on the motors.

In an effort to increase the number of sampled data inputs and rate of control, a 3D encoder cam shown in Figure 2.8(b) was designed. Due to the sensitivity of IR sensors to distance, the amplitude of the peak for the gray band becomes noticeably smaller than those of the black bands. By this means, the position of the legs over the entire cycle can be estimated based on the smaller peak reference. Figure 2.8(c) represents the analog output signal of the 3D cams with 28 detected discrete input data points that are used for motors' speed control and phase synchronization. Note that to obtain a 180° phase difference between the

diagonal leg pairs, only the position of the crank pin holes on each encoder pair are placed with 180° offset. Thus, by synchronizing the signals of all four cams to have zero phase, 180° phase difference was ensured on the legs resembling the ideal trot gait locomotion.

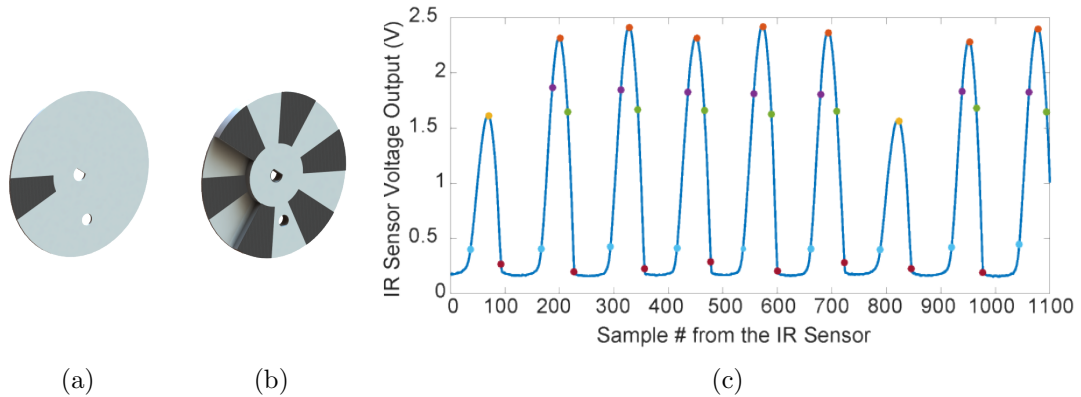


Figure 2.8: (a) Single black band cam shaft encoder. (b) 3D cam shaft encoder. (c) A 3D encoder analog output signal with 28 sample points detected per cycle for the controller input.

2.3 Fabrication and Assembly

2.3.1 Fabrication of Electronics and PCB

Before starting the assembly process of the robot, boards introduced in Section 2.2.4 must be fabricated and components must be soldered. The PCBs are manufactured by coating a mask material on the flexible sheets, ablating the coating with a laser engraver (Universal Laser Systems, VLS 6.60) in raster-scan mode to generate the appropriate mask, and etching the copper at the unmasked locations. Since the board material used is a thin flexible sheet, it must be flattened perfectly and bonded to a flat surface to prevent any wrinkles during ablation process.

Prior to coating the mask material, the surface is cleaned from dust and oils. After initial cleaning, the surface is coated by using a dark, varnish-based paint.

Afterwards, the mask material is ablated with a laser engraver to form a positive mask. Unmasked copper regions are then etched using HCl_3 solvent and the PCB traces remain with mask material on them. The remaining mask material is cleaned with acetone and finally components are soldered to the boards using solder paste and a heat gun. The whole process takes about 4 to 5 hours due to the slow speed of laser raster, relative complexity of the circuits, and the number of components that needs to be soldered, see Figure 2.9.

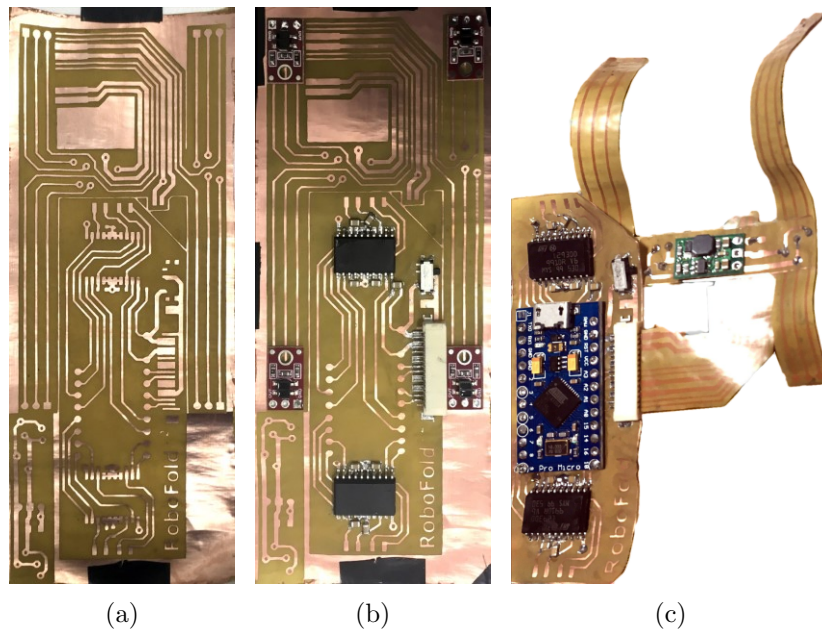


Figure 2.9: (a) PCB without any components soldered. (b) PCB without Arduino Microcontroller soldered. (c) PCBs final state after all components soldered, cut and folded ready to be inserted inside the robot.

The PCB used on MinIAQ has an Arduino Pro Micro controller that drives the four DC motors through two L293DD H-bridge motor drivers. A 3.7 Volts 150 mAh battery is placed inside the robot's body. Using a step-up regulator its output is boosted to 5 Volts to power the main board, motor drivers and sensors. The completed MinIAQ is approximately 6 cm in width, maximum of 4.3 cm in height, and about 12 cm in length. In the absence of any components, the folded structure weighs only 3.5 grams. The DC motors add a total of 5 grams and the PCB, electronic components, battery, and encoders add an extra 14.5 g to the platform making the weight of the current MinIAQ approximately 23 grams.

Once the electronics are ready, the robot's body is fabricated and assembled. The PET sheets are cut in the same laser engraver used in manufacturing of the PCBs. The assembly stage consists of consecutively folding and fastening the T-folds, placing electronics and motors inside, closing and fastening the sides and the top cover, and folding the legs, which is explained in detail in the next section.

2.3.2 Fabrication and Assembly of the Robot

This section explains the fabrication process of MinIAQ from scratch which takes less than two hours to cut and assemble. The process begins with laser cutting (using Universal Laser Systems VLS 6.60) of the unfolded design from thin PET sheets which takes about 20 minutes. The design of MinIAQ was done in AutoCAD and its technical drawing cut file is shown in Figure 2.10.

The first step in assembling MinIAQ is folding the T-shaped folds. T-folds are labeled as 1 in Figure 2.10. Once every four T-folds are folded, the IR sensors are placed inside their housing within the outer T-folds and wired to the PCB. Next, the T-folds are fastened by using double-sided tab and slot fasteners (Figure 2.10-2) explained in Section 2.2.3 of this chapter. After that, motors and sensors are placed into the housings that are located on the corners of the T-folds. Then, the extension tabs labeled as 3 in Figure 2.10 are attached to the front and back of the main frame and are temporarily locked in place with small pins.

The top cover of the main frame is folded on top of the T-folds after passing the sensors and motor wires through the holes placed on the top cover. Once done, the tabs and U-locking fasteners existing on top of the T-folds (Figure 2.10-4) are fastened to the top cover one by one.

Once the main body frame is enclosed, the supports carrying the load on the legs, shown in Figure 2.10 labeled as 5 are assembled for increased rigidity. These supports consist of the same tab-and-slot and locking mechanisms explained in Section 2.2.3 of this chapter.

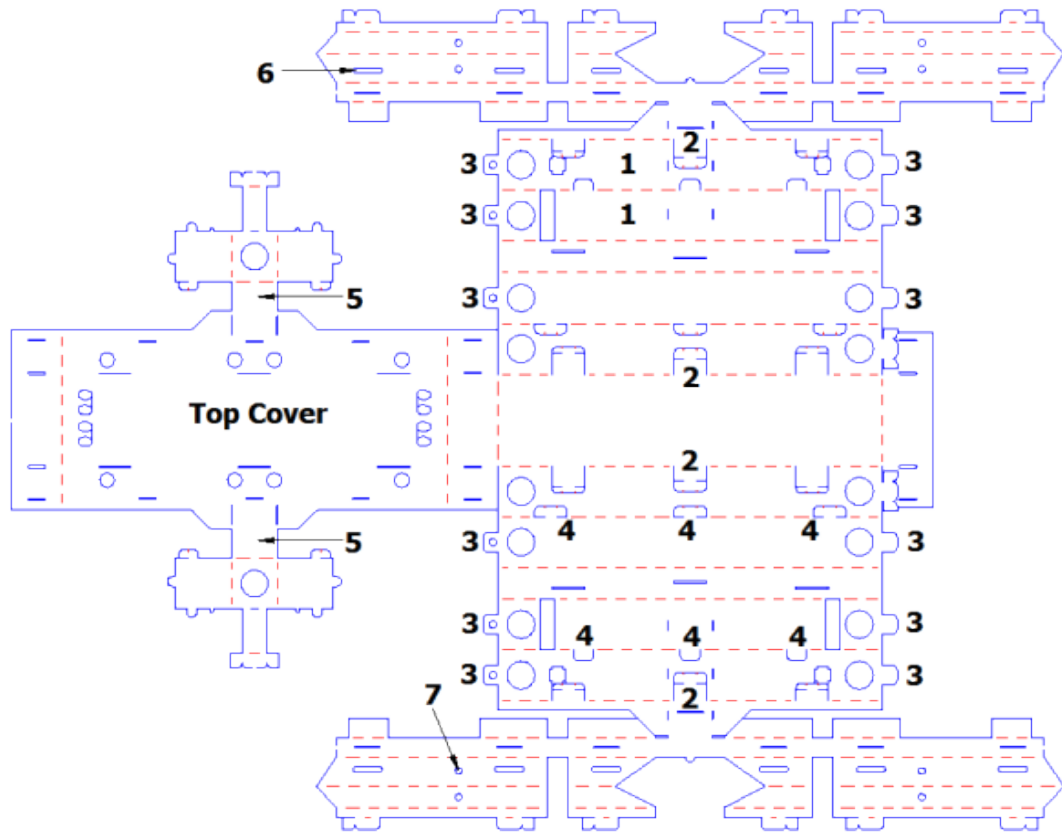


Figure 2.10: The 2D unfolded technical drawing file used for laser cutting where dashed red lines represent the folding edges and continuous blue lines show full cuts. The labeled parts are explained in detail in the text.

Prior to assembling the legs, wiring and placing electronic components should be done to avoid harming the flexure joints. Next, the legs are folded and their fasteners are locked to form rigid triangular beams.

During the assembly process, positioning some of the interior extensions and locking U-shaped fasteners can be challenging. Introducing some slots such as the one labeled as 6 in Figure 2.10 can help overcome this problem. With the help of these slots, one can access the fasteners easily with tweezers or a similar hand tool. Then, the cams are attached onto the DC motors' shafts and connecting the legs and cams by inserting a pin through the pin holes (Figure 2.10-7).

2.4 Improved Latest Version, MinIAQ-II

The originally designed first version of MinIAQ with individually actuated legs is relatively slow [5] and it cannot maneuver properly due to the easy-to-make leg mechanism which has a poor trajectory. Through designing the first version of the robot, the experience gained on mechanism design for foldable robots have been used to create an improved foldable mechanism for higher traction and better stability. The improved mechanism requires links that are not flat, essentially joints that are fixed to a specific angle. In this section, these design enhancements are demonstrated, as well as the new version of the robot, MinIAQ-II is presented [6].

The major contributions done on this section are the enhanced easy-to-fold four-bar leg mechanism design of the new version of MinIAQ as well as a systematic approach to create non-straight rigid foldable links, i.e. link designs with fixed-angle joints in the middle. It is believed that the novelties in the design of foldable structures in the original and new version robots can be applied to similar foldable or conventional microrobots and mechanisms.

Like its predecessor, the new version of the robot, named MinIAQ-II (see Figure 2.11), weighs 23 grams, is 12 cm in length, 6 cm in width, 4.5 cm in height, and can walk forward with a speed of more than 0.8 bodylengths/sec at 3 Hz stride frequency. Having optimized the actuation mechanism trajectory and observed comparable performance improvements of MinIAQ-II, this robot can be used to perform gait studies in miniature scale robots.

2.4.1 Linkages, Flexure Joints and the Main Body Design

In MinIAQ-II, 100-micrometer-thick PET sheets, same as the material used in the original MinIAQ [5], are used as the main structural material. To create kinematic chains, the well-known compliant flexure joints and triangular rigid beams are utilized. Most of the kinematic chain uses the conventional foldable

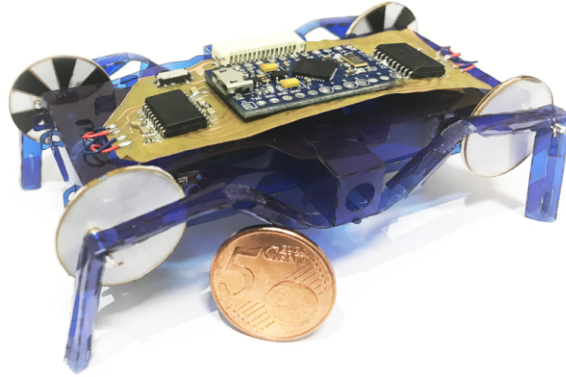


Figure 2.11: MinIAQ-II: A foldable miniature quadruped robot with independent leg actuation and improved mechanism design.

robot links and joints. However, this easy-to-make, straight rigid link shape has to be altered into a non-straight link for one of the links in the kinematic chain to improve the trajectory of the mechanism. Details on the kinematic analysis and the non-straight link fabrication are given in sections Section 2.4.2 and 2.4.3 of this chapter.

Due to the nature of foldable robot fabrication that employs a single thin sheet of material as the main structural element, integrity of the main frame and rigid linkages are very important. To achieve a reasonable degree of structural integrity, several types of tab-and-fastener locking mechanisms were embedded into the original design.

In the original MinIAQ design, T-folds were introduced to increase bending stiffness of the main frame of the body, U-shaped fastener tabs to keep the folded structures locked, and tight fit tab-and-slot fasteners to block sliding dislocations on structure planes. The T-folds are created as a crease pattern of three parallel lines on the main frame part of the sheet. When the three parallel lines are folded inwards 90 degrees, outwards 180 degrees, and outwards 90 degrees, respectively, they form a T-shaped structure in the body [5]. If T-folds, U-fasteners and tight fit tab-and-slots are used together in right spots, the T-folds become I-beam like structures and the main body frame enclosure becomes very stiff; it does not bend, twist, or buckle during operation (see Section 2.2.3). In the new version of MinIAQ, all of these structural elements are used very similar to the first version.

2.4.2 Locomotion Mechanism Optimization

The original easy-to-fold four-bar leg design in MinIAQ has a relatively poor trajectory, therefore, the robot is quite bouncy and slow [5]. Essentially, a flatter and more elliptical trajectory is needed in order to maximize the lateral motion during ground contact and reduce the bounciness. Altering the straight coupler link into a knee-shaped link, as can be observed in many animals, can shift the trajectory of the tip of the leg more in parallel with the ground. But this alteration is not straight-forward due to restrictions of the manufacturing process and 2D unfolded design complexities. Thus, the simplest solution to tackle a non-straight rigid link design is to make a fixed-angle locking joint and incorporate that to the coupler link design.

Position-based optimization methodology is employed to determine a set of design parameters for the best achievable trajectory for this specific four-bar leg design. In optimizing the mechanism, certain criteria and design constraints are imposed. The algorithm is to carefully define regions in which each individual node can be relocated incrementally such that the resulting leg trajectory is as close as possible to the ideal trajectory. The optimization algorithm seeks for the best set of design variables that minimizes the cost function, being the least square error between the resulting tip trajectory and the ideal desired trajectory. Figure 2.12 illustrates the trajectories of the final configuration of the optimized mechanism as well as the trajectory of the original MinIAQ's mechanism. With the resulting mechanism, MinIAQ-II benefits from a longer stride length, improved lateral ground contact, smaller leg lift (bounciness), and less flexure joint bending.

2.4.3 Fixed-Angle Knee Joint Design

The implementation of the enhanced mechanism requires an unfolded crease pattern to precisely obtain a required fixed angle lock between two triangular rigid beams. There are examples of non-straight members such as in gripping structure of [19] in literature. However, no detail is given on how to systemically design

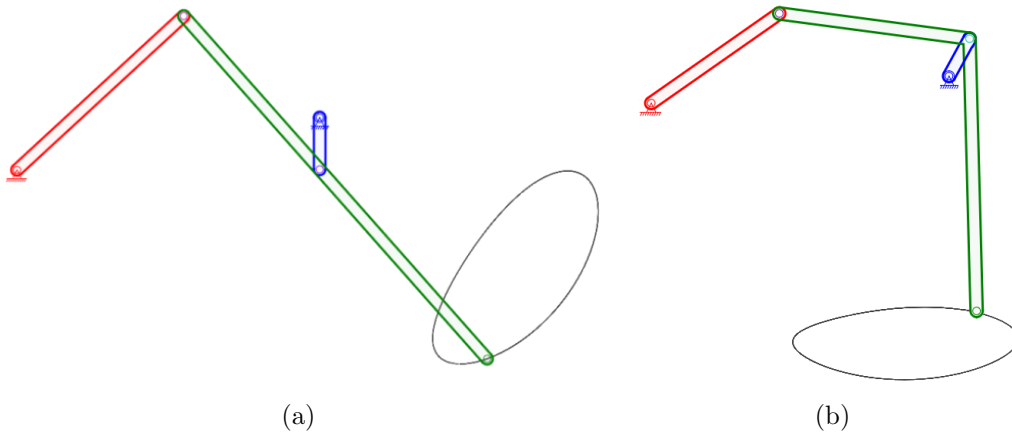


Figure 2.12: (a) Original locomotion mechanism trajectory of MinIAQ. (b) Optimized mechanism trajectory of MinIAQ-II.

and control the locking angle of such rigid bent links, therefore implementing similar designs for other researchers are very hard. For this reason, many design iterations are done to get a rigid-enough locking mechanism at any desired design angle specified.

The majority of the changes in MinIAQ-II design, compared to the original MinIAQ, comes from its optimized leg mechanism shown in Figure 2.12. How to fold a single leg in two main steps to form the final shape is illustrated in Figure 2.13. The proposed design for the knee-shaped link consists of two regular triangular beams connected with a short flexure joint and an inclined fixed-angle tab-and-fastener locking mechanism next to it. Note that the angle between the inclined fastener and the leg orientation on the unfolded structure is equal to the resulting desired fixed-angle lock between the folded beams.

With the proposed design, any two triangular beams can potentially be locked together at any desired acute or obtuse angles. If one requires to lock the right portion of the leg with a downwards orientation, similar to MinIAQ-II, the triangular beams can be folded in the reverse direction and the locking mechanism can be placed accordingly to be folded and locked in reverse. In the original MinIAQ, the triangular beams have been folded upwards, but they are folded downwards in MinIAQ-II to enable the 81° fixed-angle lock.

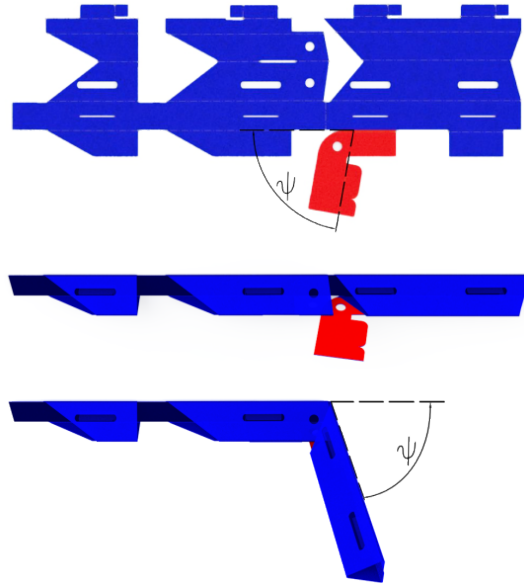


Figure 2.13: A schematic representation of the unfolded to folded structure of the new leg design. The knee shaped triangular beam link consists of two triangular beams and a fixed angle joint that is locked in place with the help of the inclined fastener.

2.4.4 Performance of MinIAQ-II

MinIAQ-II's performance on straight walking and turning are tested in several experiments and the new version's performance is compared to its predecessor. MinIAQ-II can run about 30 minutes on a single fully charged 150mAh battery and the flexure joints last a few hours of constant operation before fatigue failure. The kinematic simulation of an ideal trot gait driven at 3 Hz (Figure 2.14) is done in SolidWorks for both versions of the robot with correct physical and material properties. While the robot has shown successful performance at different stride frequencies, it is generally run at 3 Hz for tests and simulations because MinIAQ-II achieves a more natural and stable quadrupedalism behavior at 3 Hz stride frequency.

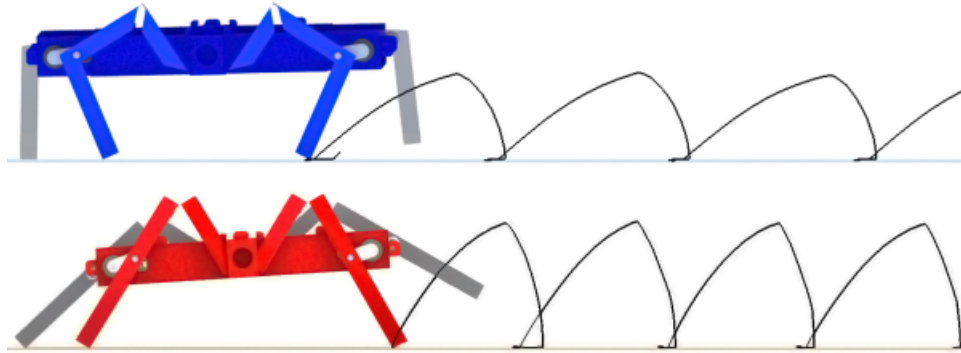


Figure 2.14: Comparison between forward leg trajectory for ideal trot gait simulation of MinIAQ-II (top) and MinIAQ (bottom).

Simulation results show the new version's superiority over the original MinIAQ. The results not only imply larger stride length, but also suggest a more stable walk due to smaller leg lift. Several experiments are conducted to verify the performance increase suggested by the simulations. The experiments demonstrate an increase in average forward locomotion speed from 0.65 bodylengths/s (7.5 cm/s) in original MinIAQ to more than 0.8 bodylengths/s (9.7 cm/s) in MinIAQ-II.

Figure 2.15 shows the simulation results of pitch and roll angle variations at 3 Hz-drive, together with snapshots of experimental results for maximum pitch and roll. The experiments are in good agreement with the simulation results. Due to the improved mechanism, MinIAQ-II has a more stable walk and much better maneuverability due to an approximate decrease in body's roll from $\pm 21^\circ$ to $\pm 9^\circ$ and a lower pitch angle of 0° - 7° compared to the original MinIAQ's 0° - 11° pitch.

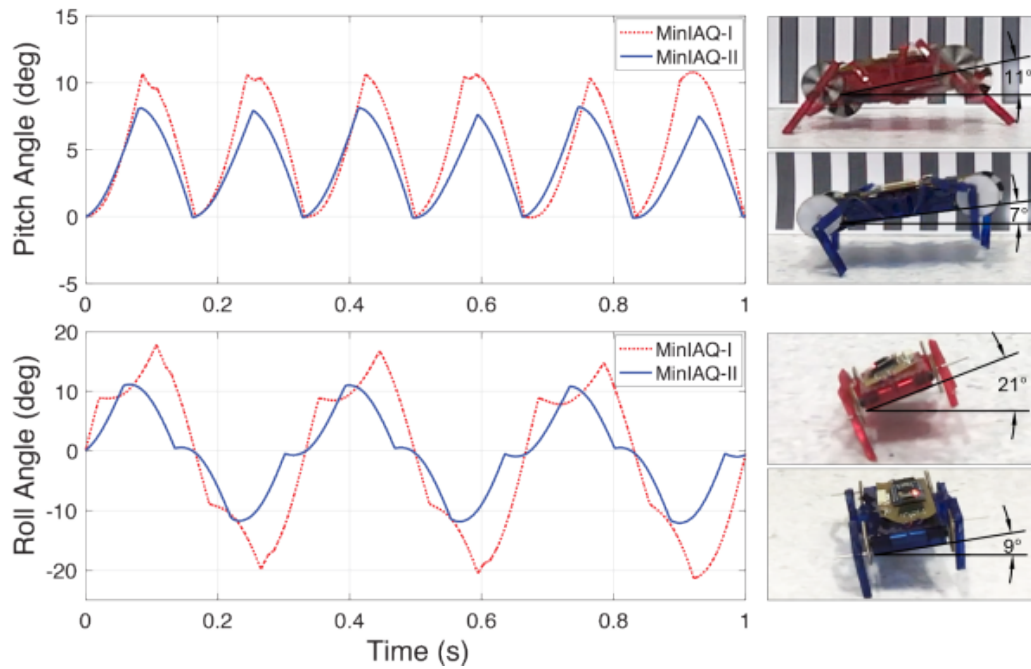


Figure 2.15: Estimation of pitch and roll angles variations from simulation at 3 Hz for both versions of MinIAQ. The snapshots on the right show the maximum recorded pitch and roll from actual tests.

The relatively better stabilization and balance in locomotion of MinIAQ-II helps the robot to have a more uniform load distribution on its feet. This uniform load distribution results in improved maneuverability of MinIAQ-II, where its predecessor lacks the most. The feet of the previous version of the MinIAQ cannot keep traction properly due to the varied load distribution and results with an in-place turning with an inconsistent angular speed and low success rate. On the other hand, MinIAQ-II can successfully turn in-place in every trial with an almost constant angular speed. Figure 2.16 shows the capability of the robot to turn in-place with a speed of $60^\circ/\text{s}$ at 3 Hz motor frequency.

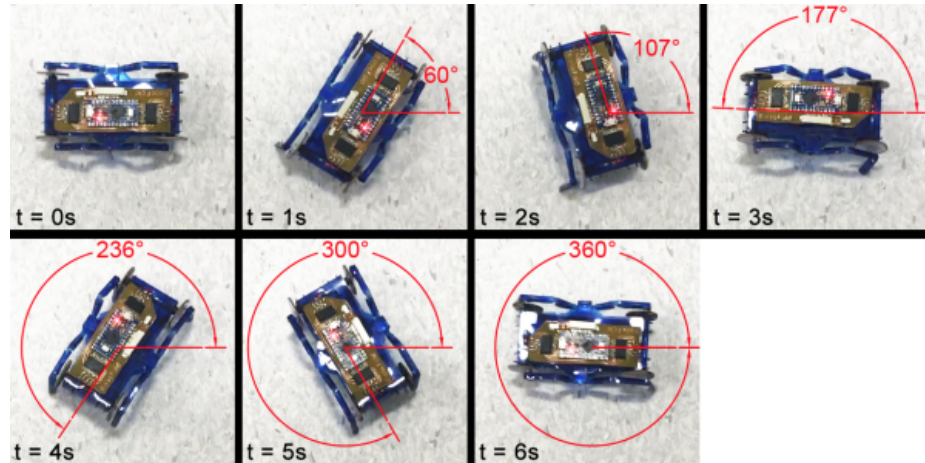


Figure 2.16: Snapshots of MinIAQ-II’s improved maneuverability during a zero-radius in-position turning test at 3 Hz drive frequency.

2.5 C-Quad and C-Shaped Wheel Design

In the design of the C-Quad, the aim was to use a leg design that would provide the robot a high mobility. Originally, RHex showed impressive rough terrain locomotion capabilities using C-shaped compliant legs [28]. More recently a similar leg design is implemented by Maryland Microrobotics Laboratory on a robot much smaller (sub-2 grams) using 3D printed rigid materials, which proved that even without the compliance, C-shaped leg structure can help a miniature robot walk on rough terrain [4].

Most foldable robots utilize simple fourbar transmissions that can be manufactured on a single sheet of material in order to exploit the ease of manufacturing in this technique. C-Quad is proposed as a design that offers robust structure, fast running, in-place turning, steering and obstacle scaling, with the downside of manufacturing the complete robot in parts on different sheets and a more complicated crease pattern for the leg design. By using a base material of thin PET sheet and optimized folds and locks, the main body frame and each leg structure form part of the highly resilient assembly.

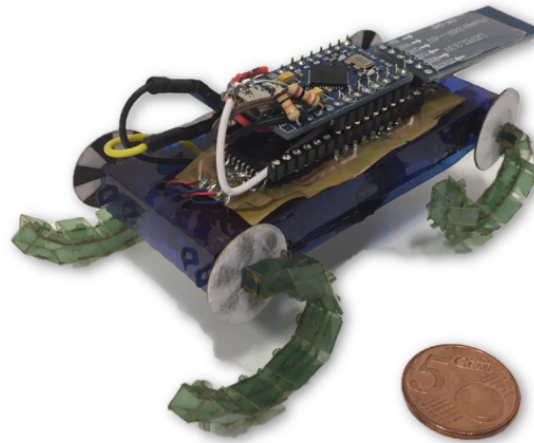


Figure 2.17: The foldable, miniature, C-shaped-legged quadruped, C-Quad.

The major contribution of C-Quad is the foldable design of the C-shaped legs and their integration into a miniature robot [7]. The modified C-shape enables fast locomotion by increasing the contact time between the leg and the ground. Main control strategy is based on controlling individual speed of the legs with the aid of IR sensors and custom encoder disks introduced in previous sections. Moreover, C-Quad has remote control with the aid of a bluetooth serial module along with the micro-controller devices located on a custom flexible printed circuit board (PCB). The resulting untethered robot weighs 38 grams and can run with a speed of 2.7 Bodylengths/sec which correspond to 27.7 cm/second.

2.5.1 Main Body Design

C-Quad uses the same structural elements, such as T-Folds, tabs and extensions, and U-Shaped lockers used in the initial and final versions of MinIAQ that increase structural rigidity and robustness. The 2D unfolded technical drawing cut file of the main frame can be seen in Figure 2.18. The only difference in design is that C-Quad does not have compliant leg mechanisms, instead it is equipped with four independent C-shaped legs in whose detailed design elements are explained in the next section.

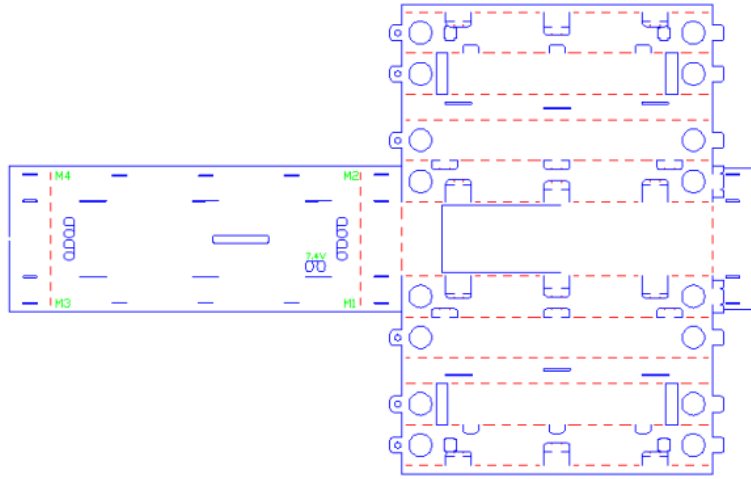


Figure 2.18: 2D unfolded technical drawing of the body where blue lines represent the full cuts and red lines represent the folding lines.

2.5.2 C-Shaped Wheeled Leg Design

In order to obtain fast and durable locomotion, a variety of leg structures are studied. All four legs are designed in C-shaped structures instead of wheels, which can be machined onto and folded from one complete sheet in order to meet the idea of ease of manufacturing and assembly. The fact that the C-shaped legs are being produced by folding from a single thin sheet material makes them very light weight compared to regular wheels.

By definition, leg structure are required to have robustness in order to be able to provide the desired locomotion and carry the weight of the robot complete with the battery and electronic boards. Moreover, C-shaped leg designs prevent stall cases during locomotion over obstacles, a problem that can be experienced in a small-wheeled robot [28]. In the beginning of the design process, a regular C-shaped leg (similar to those in [4] and [28]) is tried.

The standard version of the C-shaped leg led to extremely imbalanced body during the locomotion. The main reason for this imbalance is the fact that the shape does not stay at a constant height with respect to the body while the leg is in contact with the surface.

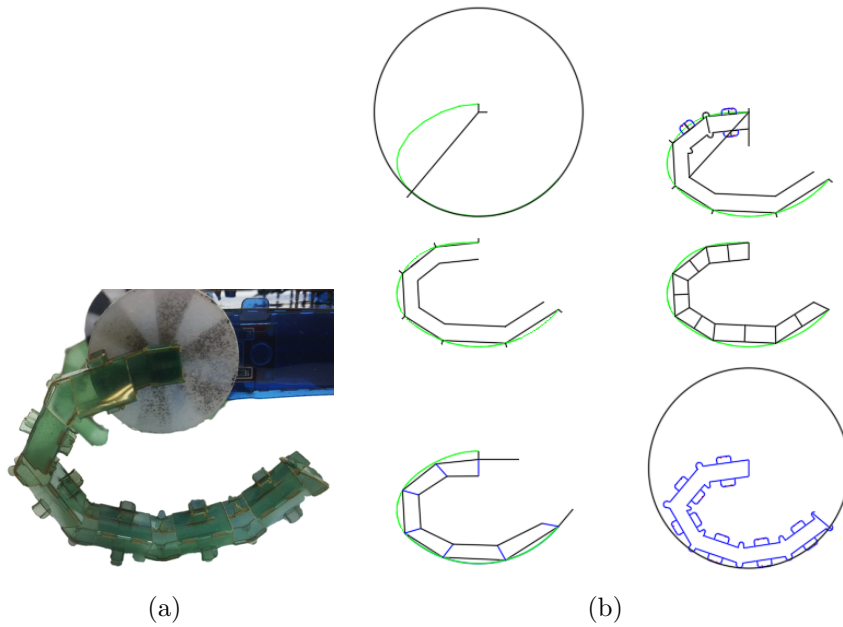


Figure 2.19: (a) The folded C-shaped leg. (b) Design iterations of C-shaped legs.

Consequently, a modified C-shaped leg is designed such that the leg surface that contacts the ground would trace a circle whose center is located at the motor hub (Figure 2.19(a)). Placing the center of the C-shaped leg to the motor hub and sweeping the leg surface to the constant radii increases the contact time of the leg (Figure 2.19(b)). By increasing the total contact time between the leg and the ground and avoiding changing height of the body during contact, the undesirable motion of the body structure is prevented. These new design of the C-shaped legs offers a fairly fast and robust locomotion for the C-Quad. The 2D unfolded technical cut file of C-shaped wheels can be seen in Figure 2.20.

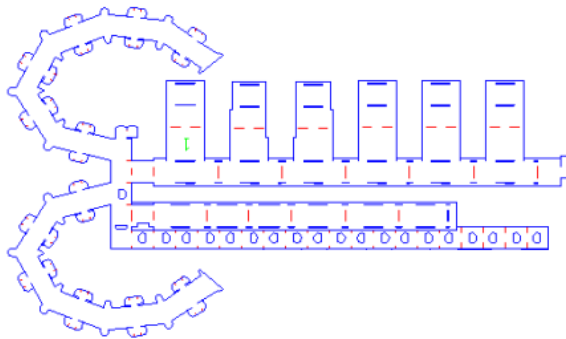


Figure 2.20: 2D unfolded technical drawing of a C-shaped leg design.

2.5.3 Performance of C-Quad

C-Quad has an ability to reach a speed of 2.7 Bodylengths/sec at its maximum speed with duty cycle of 30%. Due to the newly proposed design of the C-Shaped legs, locomotion of the robot becomes smoother compared to the classic ‘C’-shaped legs. With the aid of the new design, total contact time of the legs with the ground or obstacle is increased. Besides, the vertical movement of the center of gravity of the C-Quad’s body frame is reduced by the new C-Shaped legs.

C-Quad, as a miniature robot, is expected to work inside confined spaces where there is usually limited space for steering operations. By considering this, the C-Quad is equipped with four actuators that allow it to perform tight turns. By rotating the motors on different sides of the robot in opposing directions, C-Quad can perform a zero-radius-turn. By switching the directions of the rotation on both sides, the robot can be tightly turned right or left. Additionally, C-Quad can turn at different turning radii by adjusting the relative speeds of left and right motors. A series of screen shots demonstrating the robot’s steering capability is shown in Fig. 2.21.



Figure 2.21: Controlled steering of the C-Quad.

C-Quad should be able to operate on rough terrain where it is likely to encounter small obstacles. So far, other robots with C-shaped legs proved that this leg shape is very beneficial for rough terrain locomotion [4, 28]. Experiments are done to observe the maximum height of an obstacle can C-Quad scale. Experiments showed that the maximum height that the C-Quad can climb is 25 mm, which is more than 64% of its height. The speed controller also helps the locomotion over obstacles. C-Quad’s performance on locomotion over obstacles are demonstrated

in a series of screen shots showing C-Quad climbing to a 2.5-cm-obstacle is shown in Figure 2.22.

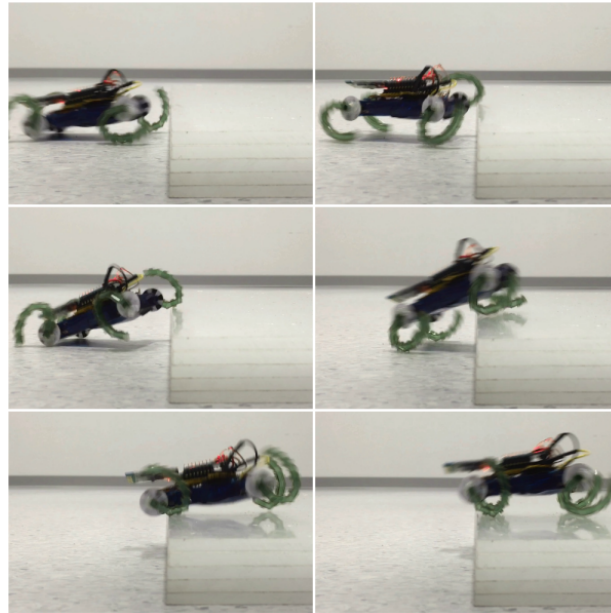


Figure 2.22: C-Quad locomotion over obstacle of 2.5 cm.

Chapter 3

Compliant Joints and Beam Theory

In this chapter, first linear elastic small angle deflection models, then large angle nonlinear deflection models are presented for cantilever beams.

3.1 Advantages of Compliant Joints

Compliant joints offer less movable parts, less assembly processes, time and effort compared to traditional joints that has turning, sliding parts that needs to be assembled. This results in less friction losses, reduced weight, wears, need for lubrication and maintenance.

Since compliant joint is a flexible component that elastically deforms, it can store energy in the form of strain energy [24]. This energy can be stored just like a spring to achieve certain tasks in any mechanism. The motion a compliant joint generates might have high repeatability as long as elastic deformations remain at specific limits.

Because of its benefits compliant joints find a common use in micro-structures,

actuators and sensors such as, Micro Electro Mechanical Systems (MEMS), Scanning Probe Microscopy (SPM) [29], Atomic Force Microscopy Scanning (AFM) [30], nano-positioning [31] and robotic applications [5, 22, 27, 28, 32].

3.2 Limitations of Compliant Joints

The biggest problem of a compliant joint is fatigue failure from cyclic loading. Because their motion comes from bending of flexible parts, compliant mechanisms experience stress at those locations. When that motion is repeated during its life, fatigue loads are present and the fatigue life must exceed the expected life of the mechanism [33].

While it has many advantages over revolute joints, there is a limit to a deflection that a compliant joint can take, so they cannot be used for continuous rotation.

Another issue arises when a kinematic model is desired for a compliant mechanism. Because of the fact that compliant joints generally undergo large deformations, the large angle nonlinear models should be considered to obtain precise position and force on mechanism members.

3.3 Linear Elastic Small Deflections

In this section, linear elastic deflections for small deflections are analyzed. Small deflections are defined as deflections to be significantly less than %10 of the beam length [33]. This deflection model linearizes the Bernoulli–Euler equation by some simplifications such as, the displacement is considered to be very small compared to the dimensions of the cantilever beam, the material is elastic and strain is proportional to the stress. In these deflection model stresses are generally below the yield point.

According to Bernoulli–Euler linear elastic beam theory,

$$\frac{d\theta}{ds} = \frac{M}{EI} = \frac{d^2y/dx^2}{\left[1 + (dy/dx)^2\right]^{3/2}} \quad (3.1)$$

where M is moment, $\frac{d\theta}{ds}$ is rate of change in angular deflection, E is Youngs Modulus of the material and I is moment of inertia.

If the deflection is small, which means $(dy/dx)^2 \ll 1$, then $(dy/dx)^2$ can be neglected. This gives the well known moment-curvature equation. From this point any force moment configuration can be applied to a cantilever beam which is derived in the following subsections.

3.3.1 Beam with End Load

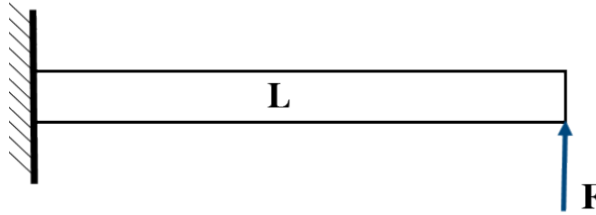


Figure 3.1: Force acting to the free end of cantilever beam with small deflections.

Moment is

$$M = F(L - x), \quad (3.2)$$

slope at any point is

$$\theta = \frac{dy}{dx} \quad (3.3)$$

and moment-curvature equation is

$$M = F(L - x) = EI \frac{d\theta}{ds}. \quad (3.4)$$

Rearranging this equation, then by integrating

$$\int d\theta = \frac{F}{EI} \int (L - x) dx \quad (3.5)$$

$$\theta = \frac{F}{EI} \left(Lx - \frac{x^2}{2} \right) + C_1 \quad (3.6)$$

is obtained. C_1 constant can be obtained from inputting boundary conditions to Equation (3.6). For $\theta = 0$ $x = 0$, then $C_1 = 0$. The deflection is

$$\theta = \frac{dy}{dx} = \frac{F}{2EI} (2L - x). \quad (3.7)$$

If Equation (3.7) is rearranged and integrated, deflection can be obtained as

$$y = \int \frac{Fx}{2EI} (2L - x) dx = \frac{F}{2EI} \left(Lx^2 - \frac{x^3}{3} + C_2 \right), \quad (3.8)$$

then inserting the boundary conditions to Equation (3.8). For $x = 0$ $y = 0$ yields $C_2 = 0$. Therefore, deflection becomes

$$y = \frac{Fx^2}{6EI} (3L - x). \quad (3.9)$$

From Equation (3.9) values at the free end of the cantilever beam, for $x = L$, are

$$y_{max} = \frac{FL^3}{3EI}, \quad \theta_{max} = \frac{FL^2}{2EI} \quad (3.10)$$

and values at the fixed end are, for $x = 0$,

$$M_{max} = FL. \quad (3.11)$$

3.3.2 Beam with End Moment

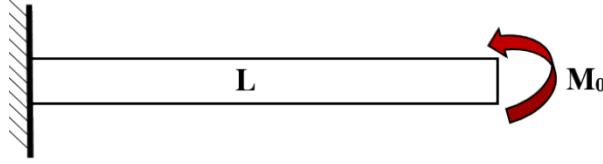


Figure 3.2: Moment acting to the free end of cantilever beam with small deflections.

By using the moment-curvature equation and deriving the equations by using the same approach used in Section 3.3.1 with respect to the boundary conditions for end moment, following equations are obtained.

$$y = \frac{M_0 x^2}{2EI}, \quad \theta = \frac{M_0 x}{EI} \quad (3.12)$$

For $x = L$,

$$y_{max} = \frac{M_0 L^2}{2EI}, \quad \theta_{max} = \frac{M_0 L}{EI}, \quad M_{max} = M_0 \quad (3.13)$$

3.3.3 Beam with Vertical End Force and Moment Loads at the Free End

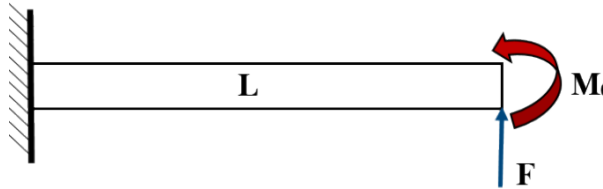


Figure 3.3: Force and Moment acting to the free end of cantilever beam with small deflections.

Repeating same procedure with moment-curvature equation with combined end load boundary conditions to derive equations yields following equations.

$$y = \frac{F x^2}{6EI} (3L - x) + \frac{M_0 x^2}{2EI}, \quad \theta = \frac{F}{2EI} (2L - x) + \frac{M_0 x}{EI} \quad (3.14)$$

For $x = L$,

$$y_{max} = \frac{FL^3}{6EI} + \frac{M_0L^2}{2EI}, \quad \theta_{max} = \frac{FL^2}{2EI} + \frac{M_0L}{EI}, \quad M_{max} = M_0 + FL \quad (3.15)$$

3.4 Nonlinear Large Deflections

Nonlinear large angle deflection analysis assumes small strains but large deformations. Nonlinearities from large strains must be taken into account if the strain is large enough to cause significant changes in geometry, such as area or thickness [24], but these cases are not considered under this work because such geometrical changes do not occur in compliant mechanisms and miniature robotics.

3.4.1 Historical Background of Nonlinear Large Deflections

Compliant mechanisms are advantageous and commonly used in micro-structures, actuators, sensors and robotic applications because of their properties such as number of parts, assembly process, time and effort, friction, weight, cost etc. . . against traditional revolute joints. Because of the fact that their motion comes from bending of flexible parts, compliant mechanisms experience large deformations at throughout the length of joints. Therefore, linear elastic beam theory fails to predict their motion. Since the joint itself has a length, it undergoes large displacements that causes geometric nonlinearities and these nonlinearities must be taken into account to achieve accurate results.

There have been several different methods are available in literature to solve nonlinear large angle deflections, some of them are elliptic integral solutions [24, 34–43], pseudo-rigid-body model (PRBM) methods [24, 44–52], the finite element method, chained beam constraint model [24, 53–55], Adomian decomposition method [40, 56] and circle-arc method [57]. Elliptic integral solutions are considered to be the most accurate in predicting large deflections as long as the

end slope and load parameters are known. In the absence of these parameters numerical calculations are needed to be done, which are very sensitive to initial guess depending on the loading case. Besides, elliptic integral solutions converge very fast with iterative methods compared to finite element methods. In kinematic analysis or optimization problems, fast solution convergence can prove to be beneficial.

Elliptic integral solution in literature is first derived by Bisshopp and Drucker for vertical force acting on the free end of a cantilever beam [39]. Improvements to this solution for combined loading and other cases are done by Frish-Ray et al. [24, 34, 35, 43, 58]. The loading cases in which an inflection point occurs is modeled by Shoup et al. with elliptic integrals [24, 36–38, 42]. Beam with combined end forces and moment acting is the hardest to derive elliptic equations. For the case of the combined end forces and moment are acting on opposite directions an inflection point may occur. A comprehensive solution to that case is derived by Zhang and Chen [41].

3.4.2 Elliptic Integrals

For complex loading cases in large deflections, algorithms are generally very hard to derive a closed form solution. To simplify calculations elliptic integrals are widely used in nonlinear large deflection analysis [35–42].

Elliptic integral transformations are introduced in this section for complete and incomplete elliptic integrals of the first, second and third kind. In nonlinear large deflection analysis first and second kind of elliptic integrals are commonly used, but if the loading cases change third kind might be useful. The calculation of an elliptic integral can be done numerically by a series expansion [59] or precalculated tables [60].

Legendre elliptic integral is a function that needs two inputs (amplitude ϕ and modulus k) to obtain the elliptic integral value. The definition of an elliptic

integral of the first kind [60], $F(\phi, k)$ is

$$F(\phi, k) = \int_0^\phi \frac{d\theta}{\sqrt{1 - k^2 \sin^2 \theta}} \quad (3.16)$$

where ϕ is the amplitude and k is the modulus of the elliptic integral. The definition of an elliptic integral of the second kind [60], $E(\phi, k)$ is

$$E(\phi, k) = \int_0^\phi \sqrt{1 - k^2 \sin^2 \theta} d\theta \quad (3.17)$$

and the definition of an elliptic integral of the third kind [60], $\Pi(\phi, \alpha^2, k)$ is

$$\Pi(\phi, \alpha^2, k) = \int_0^\phi \frac{1}{(1 - n \sin^2 \theta) \sqrt{1 - k^2 \sin^2 \theta}} d\theta. \quad (3.18)$$

Elliptic integrals in Equations (3.16) to (3.18) are *incomplete elliptic integrals of the first, second and third kind*. *Complete elliptic integral* is a special case of elliptic integral when $\phi = \frac{\pi}{2}$ and can be denoted as $F(\frac{\pi}{2}, k) = F(k)$, $E(\frac{\pi}{2}, k) = E(k)$ and $\Pi(\frac{\pi}{2}, \alpha^2, k) = \Pi(\alpha^2, k)$.

The simplified method of solving equations that involve elliptic integrals are as follows [24]:

1. Derive the equations that describe the system. These equations will include integral terms that cannot be solved by usual methods.
2. Manipulate these integral terms until they are in a form that is integrable using elliptic integrals.
3. Choose a solution form available in the literature [60]. Once this step is completed the solution will contain elliptic integrals.

3.4.3 Beam with Moment at the Free End

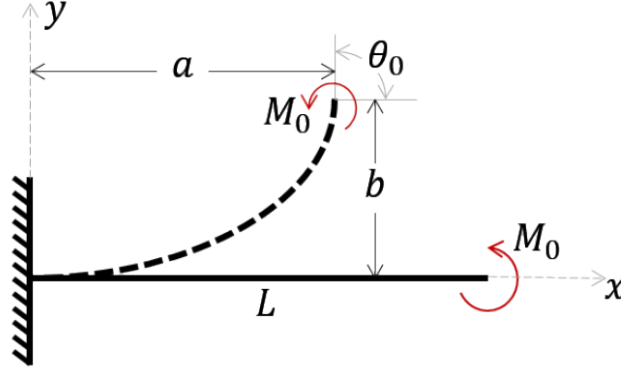


Figure 3.4: Moment acting to the free end of cantilever beam with large deflections.

Bernoulli–Euler equation is

$$k = \frac{d\theta}{ds} = \frac{M_0}{EI} \quad (3.19)$$

by rearranging, then integrating gives

$$\int_0^{\theta_0} d\theta = \int_0^L \frac{M_0}{EI}, \quad (3.20)$$

$$\theta_0 = \frac{M_0 L}{EI}. \quad (3.21)$$

Since this integration is done along the beam length s , instead of vertical distance x , the result gives the large angle solution. In order to find vertical deflection, b , Bernoulli–Euler equation should be written as follows

$$\frac{d\theta}{ds} = \frac{M_0}{EI} = \frac{d\theta}{dy} \frac{dy}{ds} = \frac{d\theta}{dy} \sin \theta, \quad (3.22)$$

rearranging and integrating gives

$$\int_0^b dy = \frac{EI}{M_0} \int_0^{\theta_0} \sin \theta d\theta, \quad (3.23)$$

$$b = \frac{EI}{M_0} (-\cos \theta_0 + 1). \quad (3.24)$$

Similarly, for horizontal deflection, a , Bernoulli–Euler equation is written as

$$\frac{d\theta}{ds} = \frac{M_0}{EI} = \frac{d\theta}{dx} \frac{dx}{ds} = \frac{d\theta}{dx} \cos \theta, \quad (3.25)$$

rearranging and integrating gives

$$\int_0^a dx = \frac{EI}{M_0} \int_0^{\theta_0} \cos \theta d\theta, \quad (3.26)$$

$$a = \frac{EI}{M_0} (\sin \theta_0). \quad (3.27)$$

3.4.4 Beam with Combined Force Load at the Free End

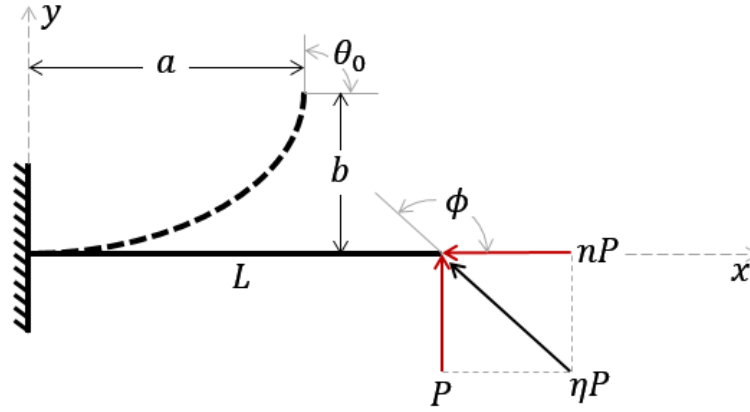


Figure 3.5: Combined force loads acting to the free end of cantilever beam with large deflections.

Moment acting on any point on the cantilever beam is given as

$$M = P(a - x) + nP(b - y) \quad (3.28)$$

and Bernoulli–Euler beam equation is

$$\frac{d\theta}{ds} = \frac{M}{EI} = k \quad (3.29)$$

where, k is curvature. Combining the moment obtained in Equation (3.28) into Equation (3.29) gives

$$k = \frac{d\theta}{ds} = \frac{P}{EI} [(a - x) + n(b - y)]. \quad (3.30)$$

If the equation above is integrated with respect to s

$$\frac{dk}{ds} = \frac{d^2\theta}{ds^2} = \frac{P}{EI} \left(-\frac{dx}{ds} - n\frac{dy}{ds} \right) \quad (3.31)$$

can be obtained. Since $dx/ds = \cos \theta$ and $dy/ds = \sin \theta$, inserting them into Equation (3.31) gives

$$\frac{dk}{ds} = \frac{d^2\theta}{ds^2} = \frac{P}{EI}(-\cos \theta - n \sin \theta). \quad (3.32)$$

Integrating the equation above with respect to ds

$$\frac{1}{2} \left(\frac{d\theta}{ds} \right)^2 = \frac{P}{EI}(-\sin \theta + n \cos \theta) + C_1 \quad (3.33)$$

is obtained. The boundary conditions for $x = 0$ $\theta = \theta_0$ and $k = d\theta/ds = 0$ and inserting them into above equation gives

$$C_1 = \frac{P}{EI}(\sin \theta_0 - n \cos \theta_0). \quad (3.34)$$

Then by inserting C_1 into Equation (3.33) and solving for $k = d\theta/ds$ gives

$$k = \frac{d\theta}{ds} = \pm \sqrt{\frac{2P}{EI}(\sin \theta_0 - n \cos \theta_0 - \sin \theta + n \cos \theta)}. \quad (3.35)$$

This equation being positive means the cantilever is bend upwards (monotonically increasing slope [42]) and has a concave curvature otherwise cantilever is bend downwards and has a convex curvature (monotonically decreasing slope [42]). To simplify this equation λ (dimensionless load coefficient) and α (dimensionless force index) coefficients are introduced [42]. Then Equation (3.35) becomes

$$k = \frac{d\theta}{ds} = \pm \sqrt{2} \frac{\alpha}{L} \sqrt{\lambda - \sin \theta + n \cos \theta} \quad (3.36)$$

and in this equation

$$\alpha^2 = \frac{PL^2}{EI} \text{ and } \lambda = \sin \theta_0 - n \cos \theta_0. \quad (3.37)$$

The P , nP forces acting to the free end of the cantilever beam has a relation as follows

$$\varphi_1 = \tan^{-1} \frac{1}{-n} \text{ or } \varphi_1 = \frac{\pi}{2} + \tan^{-1} n. \quad (3.38)$$

Here φ_1 is the angle between the x-axis and resulting force of P and nP as seen in Figure 3.5. The resulting force ηP is

$$\eta P = \sqrt{P^2 + (nP)^2} \quad (3.39)$$

and simplifying this term gives

$$\eta = \sqrt{1 + n^2}. \quad (3.40)$$

By rearranging Equation (3.36) and integrating gives

$$\frac{\alpha\sqrt{2}}{L} \int_0^L ds = \pm \int_0^{\theta_0} \frac{d\theta}{\sqrt{\lambda - \sin \theta + n \cos \theta}} \quad (3.41)$$

and by rearranging again

$$\alpha = \pm \frac{1}{\sqrt{2}} \int_0^{\theta_0} \frac{d\theta}{\sqrt{\lambda - \sin \theta + n \cos \theta}} \quad (3.42)$$

is obtained. The equation above can be converted into elliptic integral with the information given in Section 3.4.2 and becomes

$$\alpha = \pm \frac{1}{\sqrt{\eta}} \left[F\left(\frac{\pi}{2}, t\right) - F(\gamma, t) \right] \quad (3.43)$$

where

$$\gamma = \sin^{-1} \sqrt{\frac{\eta - n}{\eta + \lambda}} \text{ and } t = \sqrt{\frac{\eta + \lambda}{2\eta}}. \quad (3.44)$$

After that, in order to obtain the vertical deflection, b , the curvature relation in Bernoulli–Euler equation should be written as follows

$$k = \frac{d\theta}{ds} = \frac{d\theta}{dy} \frac{dy}{ds} = \frac{d\theta}{dy} \sin \theta, \quad (3.45)$$

inserting Equation (3.45) into Equation (3.36) gives

$$\frac{d\theta}{dy} \sin \theta = \sqrt{2} \frac{\alpha}{L} \sqrt{\lambda - \sin \theta + n \cos \theta} \quad (3.46)$$

and by separating variables and integrating vertical deflection, b , can be obtained from

$$\int_0^b dy = b = \pm \frac{L}{\sqrt{2}\alpha} \int_0^{\theta_0} \frac{\sin \theta d\theta}{\sqrt{\lambda - \sin \theta + n \cos \theta}}. \quad (3.47)$$

By applying elliptic integral transformation to this equation gives the vertical deflection

$$b = \frac{L}{\alpha\eta^{5/2}} \left\{ \eta \left[F\left(\frac{\pi}{2}, t\right) - F(\gamma, t) + 2 \left(E(\gamma, t) - E\left(\frac{\pi}{2}, t\right) \right) \right] + n \sqrt{2\eta(\eta + \lambda)} \cos \gamma \right\} \quad (3.48)$$

and likewise, to obtain the horizontal deflection, a , the curvature relation in Bernoulli–Euler equation should be written as follows

$$k = \frac{d\theta}{ds} = \frac{d\theta}{dx} \frac{dx}{ds} = \frac{d\theta}{dx} \cos \theta, \quad (3.49)$$

inserting Equation (3.49) into Equation (3.36) gives

$$\frac{d\theta}{dx} \cos \theta = \sqrt{2} \frac{\alpha}{L} \sqrt{\lambda - \sin \theta + n \cos \theta} \quad (3.50)$$

and by separating variables and integrating

$$\int_0^a dx = a = \pm \frac{L}{\sqrt{2}\alpha} \int_0^{\theta_0} \frac{\cos \theta d\theta}{\sqrt{\lambda - \sin \theta + n \cos \theta}} \quad (3.51)$$

is obtained. After elliptic integral transformation, horizontal deflection, a , can be found as

$$a = \frac{L}{\alpha \eta^{5/2}} \left\{ -n\eta \left[F\left(\frac{\pi}{2}, t\right) - F(\gamma, t) + 2 \left(E(\gamma, t) - E\left(\frac{\pi}{2}, t\right) \right) \right] + \sqrt{2\eta(\eta + \lambda)} \cos \gamma \right\}. \quad (3.52)$$

3.4.5 Beam with Combined Force and Moment Loads

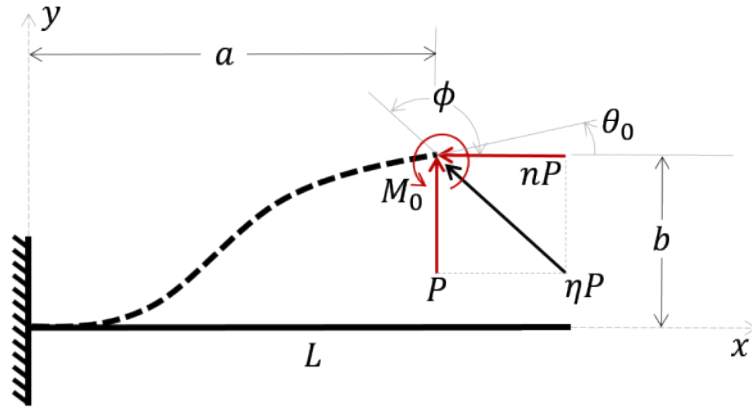


Figure 3.6: Combined force and moment loads acting to the free end of cantilever beam with large deflections.

Moment at any point on cantilever beam according to Figure 3.6

$$M = P(a - x) + nP(b - y) + M_0. \quad (3.53)$$

Bernoulli–Euler equation and the curvature of the normal axis

$$\frac{d\theta}{ds} = \frac{M}{EI} = k, \quad (3.54)$$

inserting the moment found in Equation (3.53) into Equation (3.54) gives

$$k = \frac{d\theta}{ds} = \frac{P}{EI} \left[(a - x) + n(b - y) + \frac{M_0}{P} \right] \quad (3.55)$$

and taking its derivative with respect to s

$$\frac{dk}{ds} = \frac{d^2\theta}{ds^2} = \frac{P}{EI} \left(-\frac{dx}{ds} - n\frac{dy}{ds} \right) \quad (3.56)$$

is obtained. Since $dx/ds = \cos \theta$ and $dy/ds = \sin \theta$, equation above becomes

$$\frac{dk}{ds} = \frac{d^2\theta}{ds^2} = \frac{P}{EI} (-\cos \theta - n \sin \theta) \quad (3.57)$$

and integrating with respect to θ gives

$$\frac{1}{2} \left(\frac{d\theta}{ds} \right)^2 = \frac{P}{EI} (-\sin \theta + n \cos \theta) + C_1. \quad (3.58)$$

By applying boundary condition on the free end of cantilever beam $\theta = \theta_0$ and $k = d\theta/ds = M_0/EI$

$$C_1 = \frac{P}{EI} (\sin \theta_0 - n \cos \theta_0) + \frac{1}{2} \left(\frac{M_0}{EI} \right)^2 \quad (3.59)$$

is obtained. Inserting C_1 into Equation (3.58) and solving for $d\theta/ds$ gives

$$\frac{d\theta}{ds} = \pm \sqrt{\frac{2P}{EI} \left(\sin \theta_0 - n \cos \theta_0 - \sin \theta + n \cos \theta + \frac{M_0^2}{2PEI} \right)}. \quad (3.60)$$

To simplify this equation, λ (dimensionless load coefficient), α (dimensionless force index) and κ (load ratio) is used to get

$$\frac{d\theta}{ds} = \pm \sqrt{2} \frac{\alpha}{L} \sqrt{\lambda - \sin \theta + n \cos \theta} \quad (3.61)$$

where

$$\alpha^2 = \frac{PL^2}{EI}, \quad \kappa = \frac{M_0^2}{2PEI} \quad \text{and} \quad \lambda = \sin \theta_0 - n \cos \theta_0 + \kappa. \quad (3.62)$$

and the relation between P and nP is as follows

$$\varphi_1 = \tan^{-1} \frac{1}{-n} \quad \text{or} \quad \varphi_1 = \frac{\pi}{2} + \tan^{-1} n. \quad (3.63)$$

The resulting force ηP acting to the free end is

$$\eta P = \sqrt{P^2 + (nP)^2}, \quad (3.64)$$

simplifying this term gives

$$\eta = \sqrt{1 + n^2}. \quad (3.65)$$

By rearranging and integrating Equation (3.60)

$$\frac{\alpha\sqrt{2}}{L} \int_0^L = \pm \int_0^{\theta_0} \frac{d\theta}{\sqrt{\lambda - \sin\theta + n \cos\theta}} \quad (3.66)$$

is obtained. Rearranging that equation gives

$$\alpha = \pm \frac{1}{\sqrt{2}} \int_0^{\theta_0} \frac{d\theta}{\sqrt{\lambda - \sin\theta + n \cos\theta}}. \quad (3.67)$$

Then, in order to obtain the vertical deflection, b , Bernoulli–Euler equation should be written as follows

$$k = \frac{d\theta}{ds} = \frac{d\theta}{dy} \frac{dy}{ds} = \frac{d\theta}{dy} \sin\theta \quad (3.68)$$

and by combining Equation (3.68) and Equation (3.61)

$$\frac{d\theta}{dy} \sin\theta = \sqrt{2} \frac{\alpha}{L} \sqrt{\lambda - \sin\theta + n \cos\theta} \quad (3.69)$$

is obtained. By separating variables and integrating equation above gives the vertical deflection, b , as

$$\int_0^b dy = b = \pm \frac{L}{\sqrt{2}\alpha} \int_0^{\theta_0} \frac{\sin\theta d\theta}{\sqrt{\lambda - \sin\theta + n \cos\theta}}. \quad (3.70)$$

By using the same approach, horizontal deflection, a , can be found as

$$\int_0^a dx = a = \pm \frac{L}{\sqrt{2}\alpha} \int_0^{\theta_0} \frac{\cos\theta d\theta}{\sqrt{\lambda - \sin\theta + n \cos\theta}}. \quad (3.71)$$

An inflection point is a point on a cantilever beam at which the sign of the curvature (k), moment and stress changes. Cantilever beam with combined loads and moment may or may not have an inflection point if the end moment is acting in the opposite direction as the end force [37]. According to elastica theory any number of inflection can occur on a beam for the values of ϕ is equal to

$(2n + 1)\pi/2$ [36]. On an inflection point $k = d\theta/ds = 0$, by knowing that also $M = 0$. Therefore Equations (3.60) and (3.61) will become

$$\lambda = \sin \theta - n \cos \theta. \quad (3.72)$$

This equation mathematically has infinite number solutions. Solving for θ

$$\hat{\theta}_j = 2k\pi + \phi_1 \pm \cos^{-1}(\lambda/\eta), \text{ where } k = 0, \pm 1, \pm 2, \dots \quad (3.73)$$

where $\hat{\theta}$ represents deflection angle at an inflection point and j specifies the j th inflection point starting from the fixed end. From this point, P is considered to be positive and large angle formulations are done accordingly. Sign of the end moment load S_m parameter is defined to be dependent on the sign of M_0 [41].

$$S_m = \begin{cases} 1, & \text{if } M_0 \geq 0 \\ -1, & \text{if } M_0 \leq 0 \end{cases} \quad (3.74)$$

The moment acting on cantilever beam is related with the number of inflection points m . According to beam theory, the curvature ($k = d\theta/ds$) is zero at an inflection point and changes sign between every inflection points. According to this, sign change can be related as [41]

$$S_r = (-1)^m S_m. \quad (3.75)$$

Therefore, for any m value Equations (3.67), (3.70) and (3.71) can be updated as

$$\begin{aligned} \alpha &= \frac{S_r}{\sqrt{2}} \sum_{j=0}^m (-1)^j \int_{\hat{\theta}_j}^{\hat{\theta}_{j+1}} \frac{d\theta}{\sqrt{\lambda - \sin \theta + n \cos \theta}} \\ a &= \frac{S_r L}{\sqrt{2}\alpha} \sum_{j=0}^m (-1)^j \int_{\hat{\theta}_j}^{\hat{\theta}_{j+1}} \frac{\cos \theta d\theta}{\sqrt{\lambda - \sin \theta + n \cos \theta}} \\ b &= \frac{S_r L}{\sqrt{2}\alpha} \sum_{j=0}^m (-1)^j \int_{\hat{\theta}_j}^{\hat{\theta}_{j+1}} \frac{\sin \theta d\theta}{\sqrt{\lambda - \sin \theta + n \cos \theta}}. \end{aligned} \quad (3.76)$$

These three equations can be solved with the help of elliptic equations of the first and second kind. Due to the limitation of these elliptic integrals, elliptic solutions to these equations are divided in two parts [41].

Case 1: $|\lambda| > \eta$ This case applies when there is no inflection point and the slope is monotonically increasing or decreasing.

$$\begin{aligned}\alpha &= \frac{S_m \sqrt{2}}{\sqrt{\lambda + \eta}} f \\ a &= \frac{S_m L \sqrt{2}}{\eta^2 \alpha \sqrt{\lambda + \eta}} [-n\lambda f + n(\lambda + \eta)e + \sqrt{\lambda + \eta}c] \\ b &= \frac{S_m L \sqrt{2}}{\eta^2 \alpha \sqrt{\lambda + \eta}} [-nf - n(\lambda + \eta)e + n\sqrt{\lambda + \eta}c]\end{aligned}\quad (3.77)$$

where

$$\begin{aligned}f &= F(\gamma_2, t) - F(\gamma_1, t) \\ e &= E(\gamma_2, t) - E(\gamma_1, t) \\ c &= \sqrt{(\lambda + n) - \sqrt{\lambda - \sin \theta_0 + n \cos \theta_0}} \\ t &= \sqrt{\frac{2\eta}{\lambda + \eta}} \\ \gamma_1 &= \sin^{-1} \sqrt{\frac{\eta - n}{2\eta}} \\ \gamma_2 &= -[-0.5k]\pi + (-1)^k \sin^{-1} \sqrt{\frac{\eta + \sin \theta_0 - n \cos \theta_0}{2\eta}}\end{aligned}$$

for $(k - 1)\pi + \phi < \theta_0 \leq k\pi + \phi$ ($k = 0, \pm 1, \pm 2, \dots$) and $[-0.5k]$ gives the largest integer that is less than or equal to $-0.5k$.

Case 2: $|\lambda| \leq \eta$ In this case cantilever beam can have any number of inflection points ($m \geq 0$) and slope can be upward or downward.

$$\begin{aligned}\alpha &= \frac{S_r}{\sqrt{\eta}} f \\ a &= \frac{S_r L}{\eta^{5/2} \alpha} [-n\eta f + 2n\eta e + \sqrt{2\eta}c] \\ b &= \frac{S_r L}{\eta^{5/2} \alpha} [nf - 2\eta e + n\sqrt{2\eta}c]\end{aligned}$$

where

$$f = \begin{cases} (-1)^m F(\gamma_2, t) - F(\gamma_1, t) - 2 \sum_{j=1}^m (-1)^j F(\gamma_{\hat{\theta}_j}, t) & \text{for } m \geq 1 \\ F(\gamma_2, t) - F(\gamma_1, t) & \text{for } m = 0 \end{cases}$$

$$e = \begin{cases} (-1)^m E(\gamma_2, t) - E(\gamma_1, t) - 2 \sum_{j=1}^m (-1)^j E(\gamma_{\hat{\theta}_j}, t) & \text{for } m \geq 1 \\ E(\gamma_2, t) - E(\gamma_1, t) & \text{for } m = 0 \end{cases}$$

$$c = \sqrt{(\lambda + n) - (-1)^m \sqrt{\lambda - \sin \theta_0 + n \cos \theta_0}}$$

$$t = \sqrt{\frac{\lambda + \eta}{2\eta}}$$

$$S_r = (-1)^m S_m$$

$$\gamma_1 = \sin^{-1} \sqrt{\frac{\eta - n}{\lambda + \eta}}$$

$$\gamma_2 = -[-0.5k]\pi + (-1)^k \sin^{-1} \sqrt{\frac{\eta + \sin \theta_0 - n \cos \theta_0}{\lambda + \eta}}$$

for $(k - 1)\pi + \phi < \theta_0 \leq k\pi + \phi$ ($k = 0, \pm 1, \pm 2, \dots$) and $[-0.5k]$ gives the largest integer that is less than or equal to $-0.5k$.

$$\gamma_{\hat{\theta}_j} = -[-0.5k]\pi + (-1)^k \frac{\pi}{2}$$

for $(k - 1)\pi + \phi < \hat{\theta}_j \leq k\pi + \phi$ ($k = 0, \pm 1, \pm 2, \dots$)

3.4.6 Beam with Initial Curvature

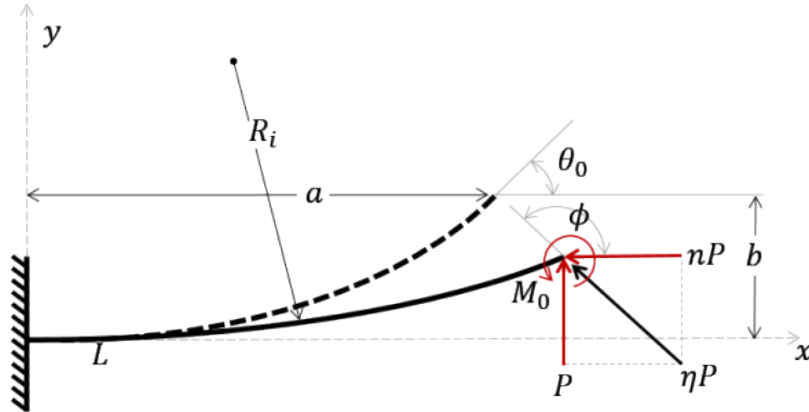


Figure 3.7: Initially curved beam with combined force and moment loads acting at the free end of cantilever beam.

In previous sections, nonlinear large deflection solutions for various loading cases were obtained. For a cantilever beam that is initially curved with moment and combined forces applied to its free end, the boundary conditions are $\theta = \theta_0$ and $k = d\theta/ds = M_0/EI + 1/R_i$. The curvature, k , in Equation (3.61) was obtained as

$$\frac{d\theta}{ds} = \pm\sqrt{2}\frac{\alpha}{L}\sqrt{\lambda - \sin\theta + n\cos\theta}. \quad (3.78)$$

The parameters used to simplify this equation λ (dimensionless load coefficient), α (dimensionless force index) and κ (load ratio) for initial curvature is redefined as

$$\alpha^2 = \frac{PL^2}{EI}, \kappa = \frac{1}{2}\left(\frac{M_0}{EI} + \frac{\mathbf{1}}{R_i}\right)^2 \text{ and } \lambda = \sin\theta_0 - n\cos\theta_0 + \kappa \quad (3.79)$$

where, R_i is the initial curvature. If cantilever beam has no initial curvature ($R_i = inf$), same κ value in Equation (3.62) can be obtained as

$$\kappa = \frac{M_0^2}{2PEI}. \quad (3.80)$$

3.5 Large vs. Small Deflections

Geometric nonlinearities due to large deflections are commonly encountered in compliant mechanisms [24]. When a compliant joint experiences large deflections, small deflection formulations given in Section 3.3 yield inaccurate results because of these geometric nonlinearities. Therefore, large angle deflection models should be used in compliant mechanisms because majority of these mechanisms undergo large deflections. In Figure 3.8, comparison of end slope, θ_0 , for small and large deflection beam models are plotted for a flexure beam. It is clear that beyond 30° of end slope the results become inaccurate.

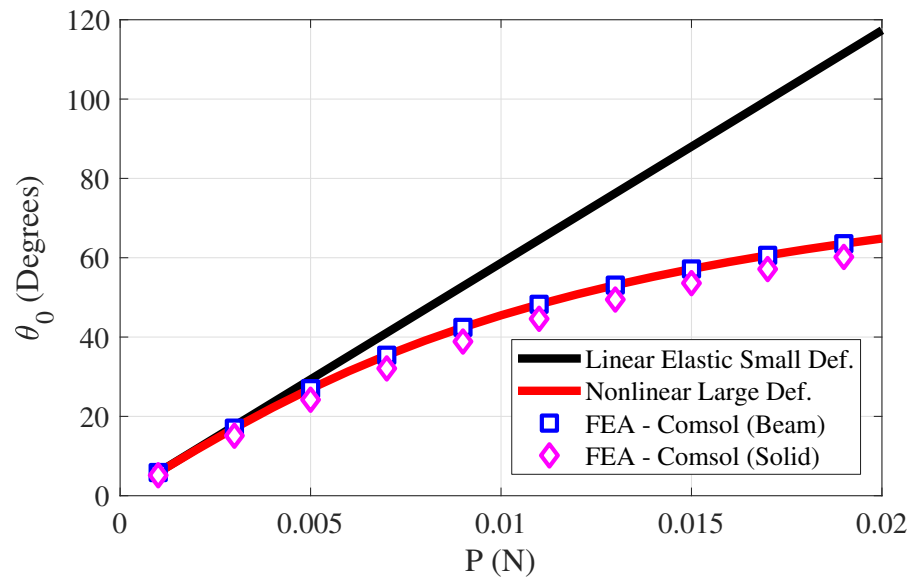


Figure 3.8: End slope of joint, θ , versus vertical end load, P , for small and large deflection models. Joint parameters: $L = 2$ mm, $b = 6$ mm, $t = 25$ μ m, $M_0 = 0$ N m and $P = 0.001$ N to 0.02 N.

Chapter 4

Kinematic Model of Rigid Linkage and Compliant Joint Mechanisms Based on Large Deflection Elliptic Integrals

In this chapter, a single leg and single joint compliant mechanism is used to verify the large deflection elliptic integral solution. Theoretical and experimental results are verified by comparing the vertical force acting on the compliant joint. Then, compliant mechanisms used in MinIAQ-I and MinIAQ-II are modeled by combining the large deflection elliptic integral into kinematic analysis.

4.1 Leg Mechanism Used in Experiments

In this section, a single joint compliant mechanism shown in Figure 4.1 is used to verify the nonlinear large deflection elliptic solution explained in Chapter 3. The vertical force acting on the compliant joint is measured by a force sensor connected to leg mechanism as the motor rotated the rigid linkage.

In the mechanism, Link AC is a compliant joint while links AE, BC, BD and BE are rigid linkages and their lengths are defined as L_{AE} , L_{CD} and L_{BD} and L_{BE} . Link AE is the motor input link and has revolute joints at both ends.

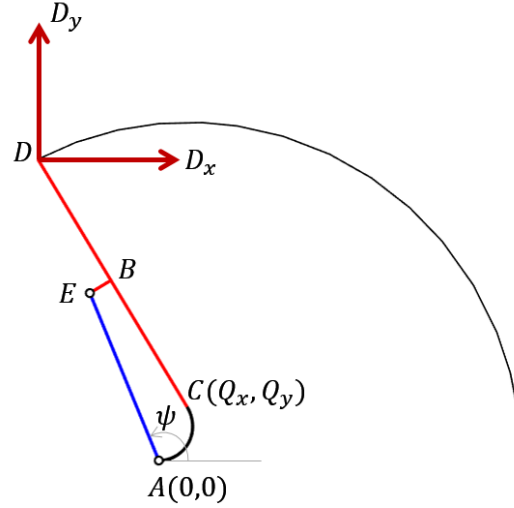


Figure 4.1: A single leg compliant mechanism used in experiments to verify kinematic analysis.

Loop closure equations according to Figure 4.1 are

$$Q_x + L_{BC} \cos \theta + L_{BE} \cos \left(\theta + \frac{\pi}{2} \right) = L_{AE} \cos \psi, \quad (4.1)$$

$$Q_y + L_{BC} \sin \theta + L_{BE} \sin \left(\theta + \frac{\pi}{2} \right) = L_{AE} \sin \psi. \quad (4.2)$$

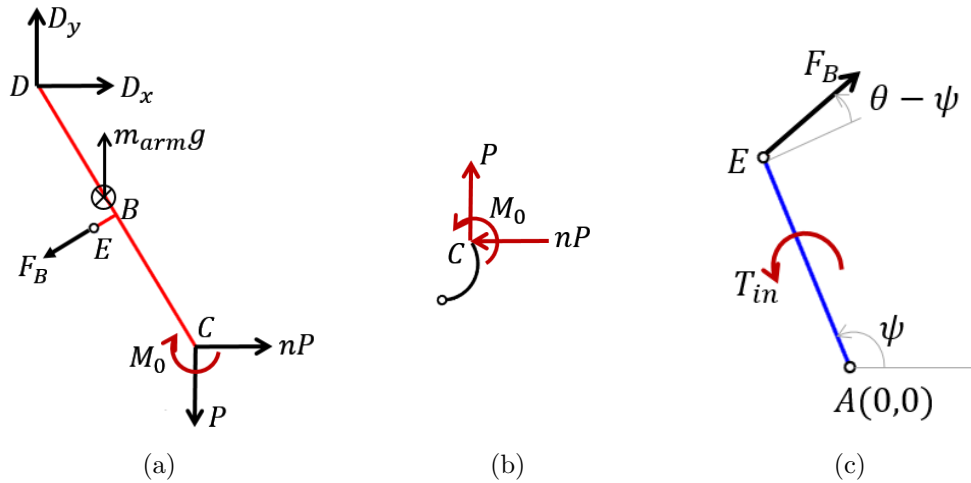


Figure 4.2: (a) Free body diagram of rigid link CD. (b) Free body diagram of compliant joint. (c) Actuator link connected to motor, link AE.

Static equilibrium equations according to Figure 4.2(a) are

$$\sum F_x = 0 \Rightarrow D_x + F_B \cos \left(\theta + \frac{\pi}{2} \right) + nP = 0, \quad (4.3)$$

$$\sum F_y = 0 \Rightarrow D_y + F_B \sin \left(\theta + \frac{\pi}{2} \right) - P + m_{arm}g = 0, \quad (4.4)$$

$$\begin{aligned} \sum M_C = 0 \Rightarrow F_B L_{BC} + L_{CD} [D_y \cos \theta - D_x \sin \theta] \\ + m_{arm}g L_{com} \cos \theta - M_0 = 0, \end{aligned} \quad (4.5)$$

$$\begin{aligned} \sum M_B = 0 \Rightarrow L_{BC} [P \cos \theta + nP \sin \theta] + L_{BD} [D_y \cos \theta - D_x \sin \theta] \\ - m_{arm}g [L_{BC} - L_{com}] \cos \theta - M_0 = 0, \end{aligned} \quad (4.6)$$

$$\begin{aligned} \sum M_D = 0 \Rightarrow L_{CD} [P \cos \theta + nP \sin \theta] - F_B L_{BD} \\ - m_{arm}g [L_{CD} - L_{com}] - M_0 = 0, \end{aligned} \quad (4.7)$$

$$\begin{aligned} \sum M_E = 0 \Rightarrow P \left[L_{BC} \cos \theta + L_{BE} \cos \left(\theta + \frac{\pi}{2} \right) \right] \\ + nP \left[L_{BC} \sin \theta + L_{BE} \sin \left(\theta + \frac{\pi}{2} \right) \right] \\ + D_y \left[L_{BD} \cos \theta - L_{BE} \cos \left(\theta + \frac{\pi}{2} \right) \right] \\ - D_x \left[L_{BD} \sin \theta - L_{BE} \sin \left(\theta + \frac{\pi}{2} \right) \right] \\ + mg \left[(L_{BC} - L_{com}) \cos \theta + L_{BE} \cos \left(\theta + \frac{\pi}{2} \right) \right] - M_0 = 0. \end{aligned} \quad (4.8)$$

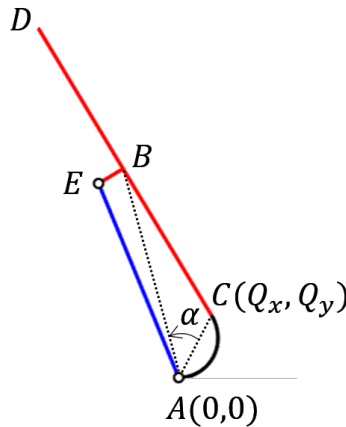


Figure 4.3: A single leg compliant mechanism with dashed lines to clarify trigonometric relation for prismatic joint.

In rigid link of the leg mechanism a slot is used to achieve vertical reaction force F_B at all times, therefore Joint B is a sliding prismatic joint. This prismatic

joint changes position by sliding inside the slot with the motor angle (ψ), the relation to obtain L_{BC} using trigonometric relations by referring to Figure 4.3 can be defined as

$$L_{AB}^2 = L_{AC}^2 + L_{BC}^2, \quad (4.9)$$

$$\alpha = (\psi - \text{atan2}(L_{BE}, L_{AE}) - \text{atan2}(Q_y, Q_x)) \text{ and} \quad (4.10)$$

$$L_{BC}^2 = L_{AB}^2 + Q_x^2 + Q_y^2 - 2L_{AB}\sqrt{Q_x^2 + Q_y^2} \cos \alpha \quad (4.11)$$

$$L_{BD} = L_{CD} - L_{BC}. \quad (4.12)$$

Input torque from motor can be obtained according to Figure 4.2 by applying static equilibrium for link AE

$$\sum M_A = 0 \Rightarrow T_{in} - L_{AE}F_B(\cos \theta \cos \psi + \sin \theta \sin \psi) = 0. \quad (4.13)$$

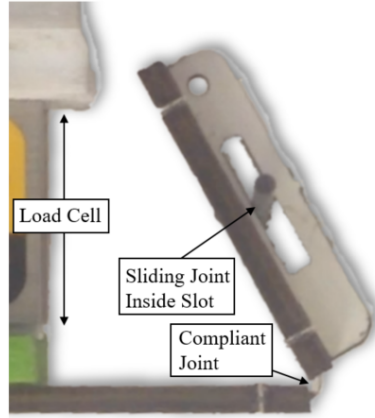


Figure 4.4: A single leg compliant mechanism used in experiments to verify kinematic analysis.

The experiment setup for verification is shown in Figure 4.4. The kinematic parameters used for this setup are $L_{AE} = 15$ mm, $L_{CD} = 23.5$ mm and $L_{BE} = 2$ mm (opposite direction meaning that $L_{BE} = -2$ mm), it should be noted that since B is a sliding joint L_{BC} and L_{BD} are variables that needs to be obtained in solution. Compliant joint parameters are as follows: length ($L = L_{AC} = 4$ mm), width ($w = 6$ mm) and thickness is ($t = 125$ μ m). Leg deflection angle versus experimental average error plot and theoretical kinematic analysis large deflection elliptic kinematic solution results are shown in Figure 4.5.

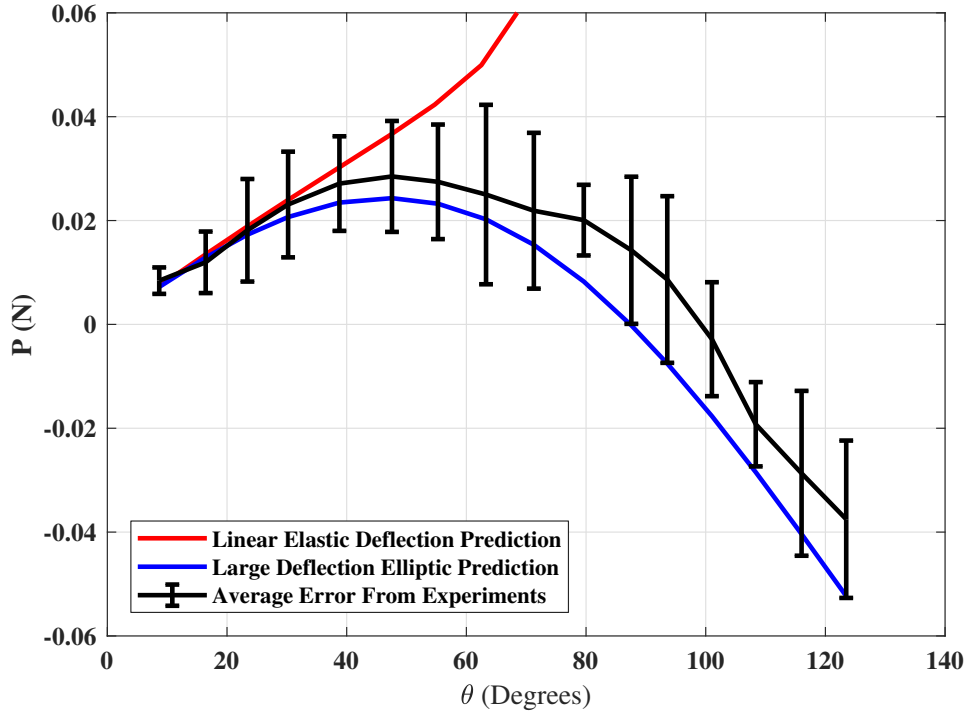


Figure 4.5: Deflection angle of joint (θ) versus vertical end load (P) experimental average error (black), and kinematic analysis of large deflection elliptic solution (red).

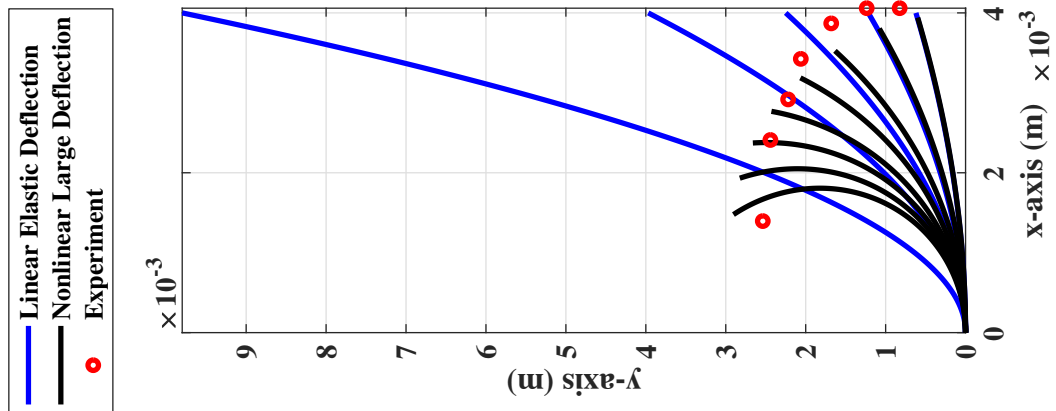


Figure 4.6: Deflection curves of beam for linear elastic (blue) and nonlinear large (black) deflection models. Tip position is shown in red circles which is obtained from experiments.

4.2 MinIAQ-I Leg Mechanism

The kinematic analysis of compliant mechanism used in MinIAQ-I [5] is modeled in this section. In the mechanism, Links AB and CD are compliant joints while points G and I are revolute joints. Links BC, DE, EF, EI and GI are rigid linkages where link GI is the motor input link and motor is positioned at coordinates (H, G) . Point F is the tip of the leg where any external loads may occur during walking due to friction or body loads. Lengths of the links are defined as L_{BC} , L_{DE} , L_{EF} , L_{EI} , L_{EG} , L_{GI} , L_{AH} and L_{GH} .

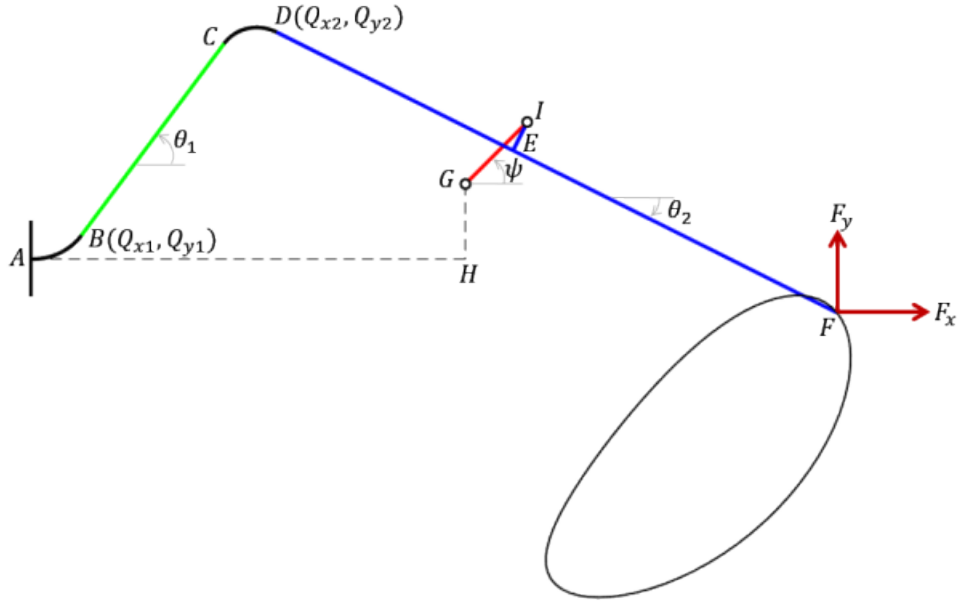


Figure 4.7: Compliant mechanism used in MinIAQ-I.

Loop closure equations according to Figure 4.7.

$$Q_{x1} + L_{BC} \cos \theta_1 + Q_{x2} + L_{DE} \cos \theta_2 + L_{EI} \cos \left(\theta_2 + \frac{\pi}{2} \right) = L_{AH} + L_{GI} \cos \psi, \quad (4.14)$$

$$Q_{y1} + L_{BC} \sin \theta_1 + Q_{y2} + L_{DE} \sin \theta_2 + L_{EI} \sin \left(\theta_2 + \frac{\pi}{2} \right) = L_{GH} + L_{GI} \sin \psi. \quad (4.15)$$

Static equilibrium equations according to Figure 4.8(c)

$$\sum F_x = 0 \Rightarrow -nP_2 \cos \theta_1 - P_2 \sin \theta_1 + nP_1 = 0, \quad (4.16)$$

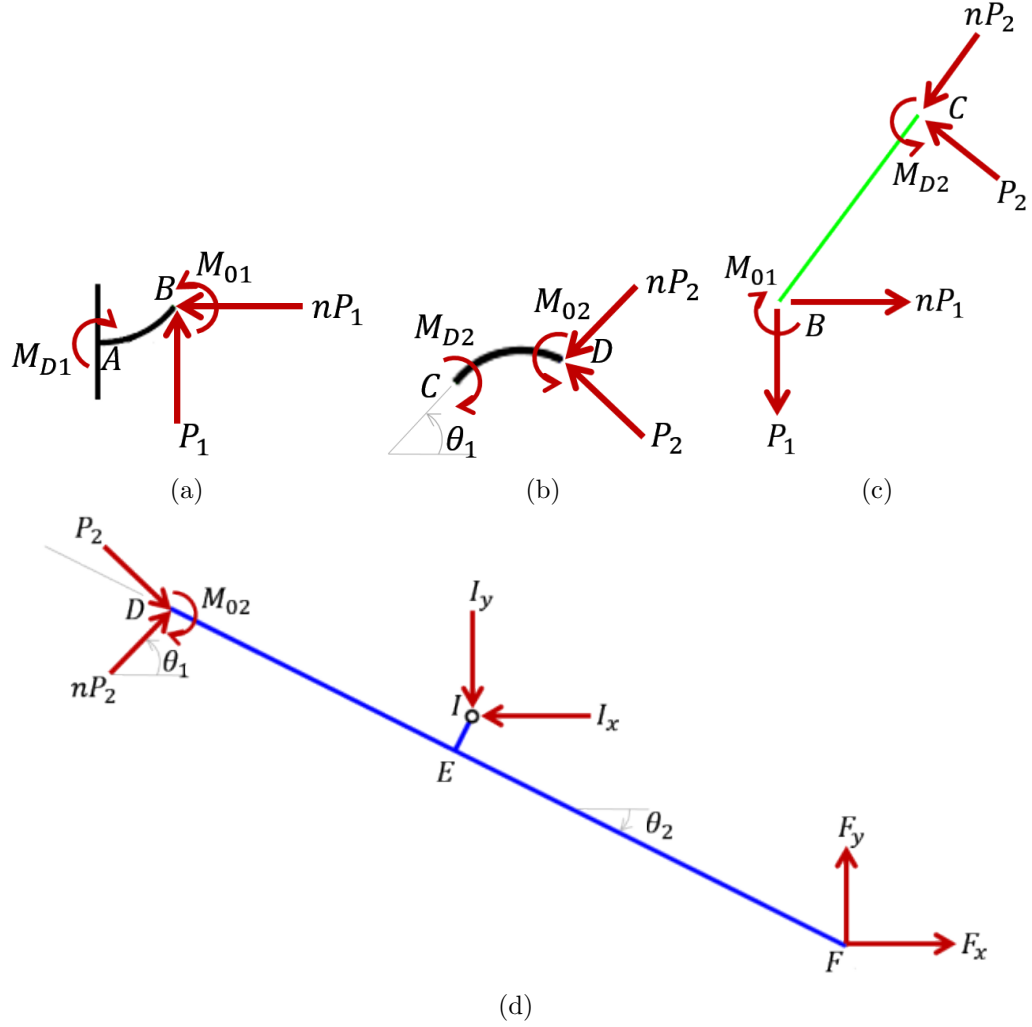


Figure 4.8: (a) Free body diagram of first compliant joint. (b) Free body diagram of second compliant joint. (c) Free body diagram of link BC. (d) Free body diagram of link DF.

$$\sum F_y = 0 \Rightarrow P_2 \cos \theta_1 - nP_2 \sin \theta_1 - P_1 = 0, \quad (4.17)$$

$$\sum M_B = 0 \Rightarrow -M_{01} + M_{D2} + L_{BC}P_2 = 0 \text{ and} \quad (4.18)$$

$$\sum M_C = 0 \Rightarrow -M_{01} + M_{D2} + L_{BC}[P_1 \cos \theta_1 + nP_1 \sin \theta_1] = 0. \quad (4.19)$$

Static equilibrium equations according to Figure 4.8(d)

$$\sum F_x = 0 \Rightarrow F_x - I_x + nP_2 \sin \left(\frac{\pi}{2} - \theta_1 \right) + P_2 \cos \left(\frac{\pi}{2} - \theta_1 \right) = 0, \quad (4.20)$$

$$\sum F_y = 0 \Rightarrow F_y - I_y + nP_2 \cos \left(\frac{\pi}{2} - \theta_1 \right) - P_2 \sin \left(\frac{\pi}{2} - \theta_1 \right) = 0, \quad (4.21)$$

$$\sum M_D = 0 \Rightarrow -M_{02} + L_{DF}[F_y \cos -\theta_2 + F_x \sin -\theta_2]$$

$$\begin{aligned}
& -L_{DE}[I_y \cos -\theta_2 + I_x \sin -\theta_2] \\
& + L_{EI}[I_x \cos -\theta_2 - I_y \sin -\theta_2] = 0, \tag{4.22}
\end{aligned}$$

$$\begin{aligned}
\sum M_E = 0 \Rightarrow & -M_{02} + L_{DE}[-nP_2 \sin \theta_1 + P_2 \cos \theta_1] \\
& + L_{EI}[I_x \cos -\theta_2 - I_y \sin -\theta_2] \\
& + L_{EF}[F_y \cos -\theta_2 + F_x \sin -\theta_2] = 0, \tag{4.23}
\end{aligned}$$

$$\begin{aligned}
\sum M_F = 0 \Rightarrow & -M_{02} + L_{DF}[-nP_2 \sin \theta_1 + P_2 \cos \theta_1] \\
& + L_{EI}[I_x \cos -\theta_2 - I_y \sin -\theta_2] \\
& + L_{EF}[I_y \cos -\theta_2 + I_x \sin -\theta_2] = 0 \text{ and} \tag{4.24}
\end{aligned}$$

$$\begin{aligned}
\sum M_I = 0 \Rightarrow & -M_{02} + L_{EF}[F_x \sin -\theta_2 + F_y \cos -\theta_2] \\
& + L_{EI}[F_x \cos -\theta_2 - F_y \sin -\theta_2] \\
& + L_{EI}[nP_2 \cos \theta_1 + P_2 \sin \theta_1] \\
& - L_{DE}[nP_2 \sin \theta_1 - P_2 \cos \theta_1] = 0. \tag{4.25}
\end{aligned}$$

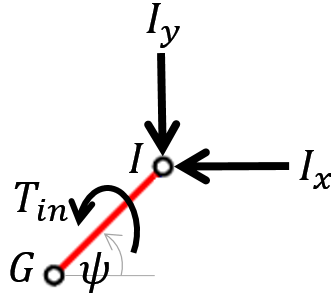


Figure 4.9: Free body diagram of the actuator link connected to motor, link GI.

Input torque from motor can be obtained according to Figure 4.9 from equation

$$\sum M_G = 0 \Rightarrow T_{in} - L_{GI}[I_x \sin \psi - I_y \cos \psi] = 0. \tag{4.26}$$

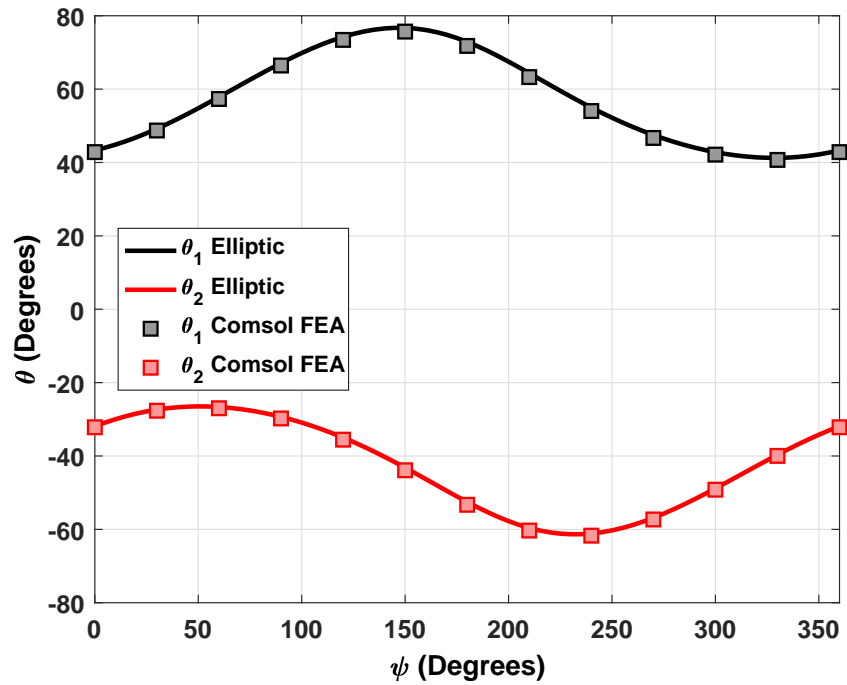


Figure 4.10: Input crank angle (ψ) versus joint deflections (θ_1 and θ_2) comparison for large deflection kinematic solution and FEA results.

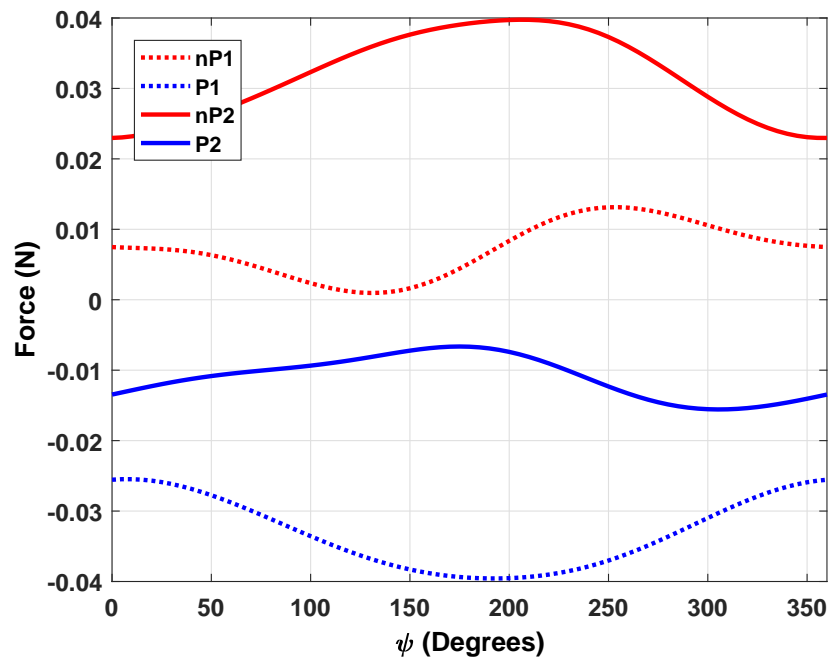


Figure 4.11: Input crank angle (ψ) versus joint end forces (P_1 , nP_1 , P_2 and nP_2) for large deflection kinematic solution.

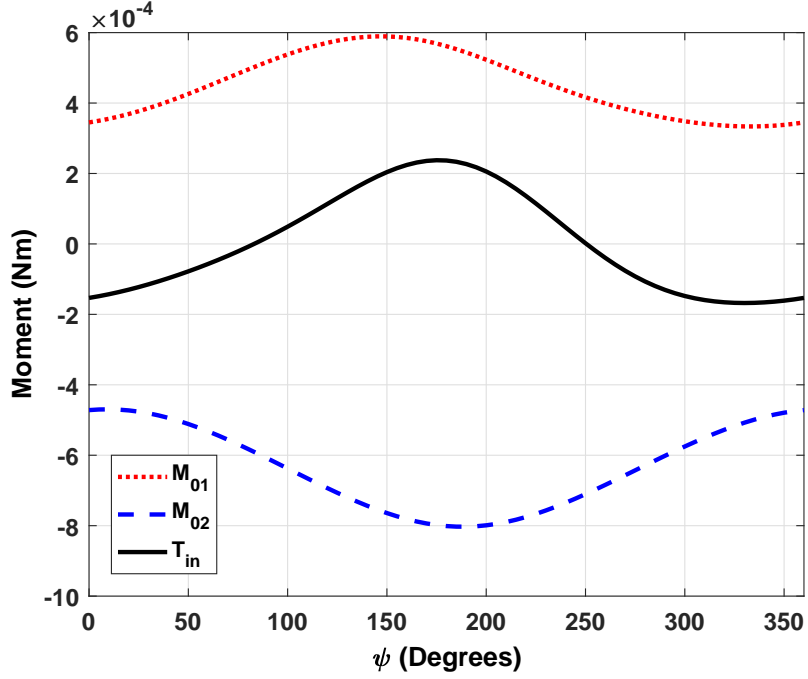


Figure 4.12: Input crank angle (ψ) versus moments (M_{01} , M_{02}) and input crank torque (T_{in}) for large deflection kinematic solution.

4.3 MinIAQ-II Leg Mechanism

The kinematic analysis of compliant mechanism used in MinIAQ-II [6] is modeled in this section. In the mechanism, Links AB and CD are compliant joints while points G and I are revolute joints. Links BC, DE, EF, EI and GI are rigid linkages where link GI is the motor input link and motor is positioned at coordinates (H, G) . The knee joint has a fixed angle defined as ϕ . Point F is the tip of the leg where any external loads may occur during walking due to friction or body loads. ϕ is the fixed angle for knee joint. Lengths of the links are defined as L_{BC} , L_{DE} , L_{EF} , L_{EI} , L_{EG} , L_{GI} , L_{AH} and L_{GH} .

Loop closure equations according to Figure 4.13

$$Q_{x1} + L_{BC} \cos \theta_1 + Q_{x2} + L_{DE} \cos \theta_2 + L_{EI} \cos \left(\theta_2 + \frac{\pi}{2} \right) = L_{AH} + L_{GI} \cos \psi, \quad (4.27)$$

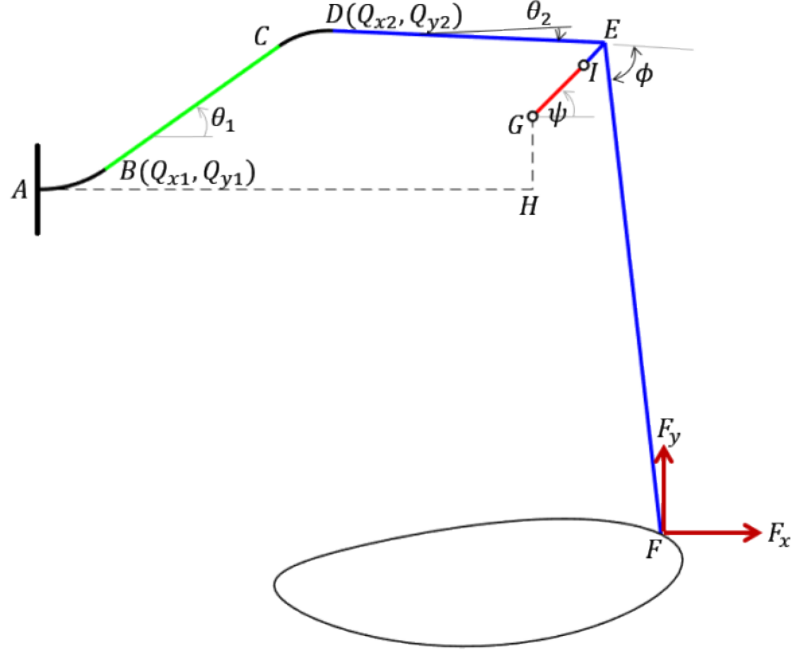


Figure 4.13: Compliant mechanism used in MinIAQ-II.

$$Q_{y1} + L_{BC} \sin \theta_1 + Q_{y2} + L_{DE} \sin \theta_2 + L_{EI} \sin \left(\theta_2 + \frac{\pi}{2} \right) = L_{GH} + L_{GI} \sin \psi. \quad (4.28)$$

Static equilibrium equations in Figure 4.14(c)

$$\sum F_x = 0 \Rightarrow -nP_2 \cos \theta_1 - P_2 \sin \theta_1 + nP_1 = 0, \quad (4.29)$$

$$\sum F_y = 0 \Rightarrow P_2 \cos \theta_1 - nP_2 \sin \theta_1 - P_1 = 0, \quad (4.30)$$

$$\sum M_B = 0 \Rightarrow -M_{01} + M_{D2} + L_{BC}P_2 = 0 \text{ and} \quad (4.31)$$

$$\sum M_C = 0 \Rightarrow -M_{01} + M_{D2} + L_{BC} [P_1 \cos \theta_1 + nP_1 \sin \theta_1] = 0. \quad (4.32)$$

Static equilibrium equations in Figure 4.14(d)

$$\sum F_x = 0 \Rightarrow F_x - I_x + nP_2 \sin \left(\frac{\pi}{2} - \theta_1 \right) + P_2 \cos \left(\frac{\pi}{2} - \theta_1 \right) = 0, \quad (4.33)$$

$$\sum F_y = 0 \Rightarrow F_y - I_y + nP_2 \cos \left(\frac{\pi}{2} - \theta_1 \right) - P_2 \sin \left(\frac{\pi}{2} - \theta_1 \right) = 0, \quad (4.34)$$

$$\begin{aligned} \sum M_D = 0 \Rightarrow & -M_{02} + L_{EI} \sin \left(\frac{\pi - \phi}{2} \right) [I_x \cos -\theta_2 - I_y \sin -\theta_2] \\ & - \left[L_{DE} - L_{EI} \cos \left(\frac{\pi - \phi}{2} \right) \right] [I_y \cos -\theta_2 + I_x \sin -\theta_2] \\ & + L_{EF} \sin \phi [F_x \cos -\theta_2 - F_y \sin -\theta_2] \end{aligned}$$

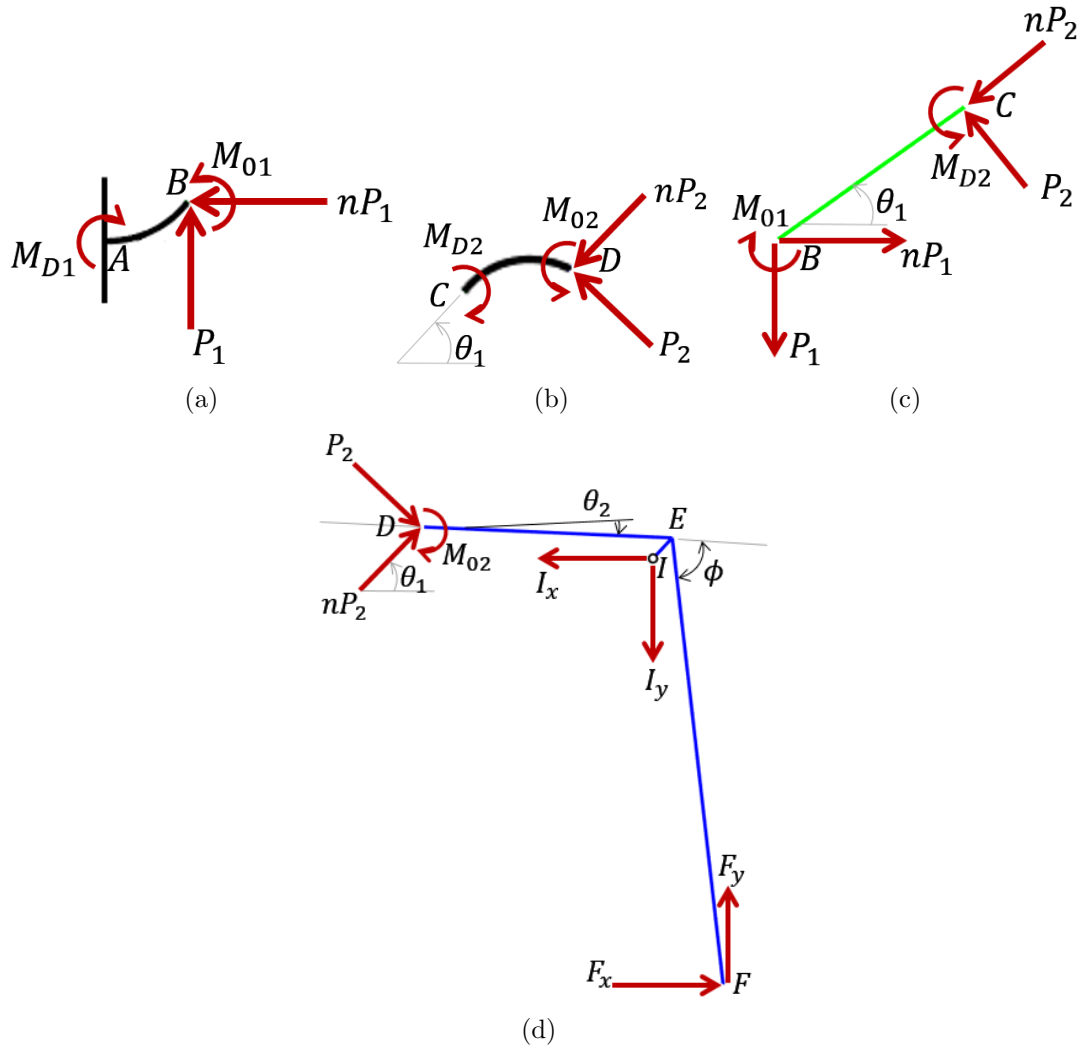


Figure 4.14: (a) Free body diagram of first compliant joint. (b) Free body diagram of second compliant joint. (c) Free body diagram of link BC. (d) Free body diagram of link DF.

$$+ [L_{DE} + L_{EF} \cos \phi] [F_x \sin -\theta_2 + F_y \cos -\theta_2] = 0, \quad (4.35)$$

$$\begin{aligned} \sum M_E = 0 \Rightarrow & -M_{02} + L_{DE} [nP_2 \sin -\theta_1 - P_2 \cos -\theta_1] \\ & - L_{EI} \sin \left(\frac{\pi - \phi}{2} \right) [I_x \cos -\theta_2 - I_y \sin -\theta_2] \\ & + L_{EF} \sin \phi [F_x \cos -\theta_2 - F_y \sin -\theta_2] \\ & + L_{EF} \cos \phi [F_x \sin -\theta_2 + F_y \cos -\theta_2] = 0, \end{aligned} \quad (4.36)$$

$$\begin{aligned} \sum M_F = 0 \Rightarrow & -M_{02} - [L_{DE} + L_{EF} \cos \phi] [nP_2 \sin \theta_1 - P_2 \cos \theta_1] \\ & - L_{EF} \sin \phi [nP_2 \cos \theta_1 + P_2 \sin \theta_1] \end{aligned}$$

$$\begin{aligned}
& + \left[L_{EF} \sin \phi - L_{EI} \sin \left(\frac{\pi - \phi}{2} \right) \right] [I_x \cos -\theta_2 - I_y \sin -\theta_2] \\
& + \left[L_{EF} \cos \phi + L_{EI} \cos \left(\frac{\pi - \phi}{2} \right) \right] [F I_y \cos -\theta_2 + I_x \sin -\theta_2] = 0 \text{ and} \\
& \hspace{20em} (4.37)
\end{aligned}$$

$$\begin{aligned}
\sum M_I = 0 \Rightarrow & -M_{02} + L_{EI} \sin \left(\frac{\pi - \phi}{2} \right) [nP_2 \cos \theta_1 + P_2 \sin \theta_1] \\
& - \left[L_{DE} - L_{EI} \cos \left(\frac{\pi - \phi}{2} \right) \right] [nP_2 \sin \theta_1 - P_2 \cos \theta_1] \\
& + \left[L_{EF} \sin \phi - L_{EI} \sin \left(\frac{\pi - \phi}{2} \right) \right] [F_x \cos -\theta_2 - F_y \sin -\theta_2] \\
& + \left[L_{EF} \cos \phi + L_{EI} \cos \left(\frac{\pi - \phi}{2} \right) \right] [F_x \sin -\theta_2 + F_y \cos -\theta_2] = 0. \\
& \hspace{20em} (4.38)
\end{aligned}$$

Input torque from motor can be obtained according to Figure 4.9 from equation

$$\sum M_G = 0 \Rightarrow T_{in} - L_{GI} [I_x \sin \psi - I_y \cos \psi] = 0. \quad (4.39)$$

Chapter 5

Fatigue Failure Prevention For Compliant Mechanisms

In this chapter, dynamic loads that vary in time are examined and how to deal with such stresses to prevent failures or achieve a specific life cycle. Since compliant mechanism members must undergo some deflections to satisfy the motion criteria, they often experience variable loading cases that must be repeated for a large number of cycles. Fatigue failure theories used in design and analysis of fatigue failure that are explained in this chapter. In literature, these stresses can be called as *variable, repeated, alternating or fluctuating* stresses [61].

5.1 Principal Stresses

Before describing the concept of principal stresses, stresses that occur at any plane should be classified (σ_x, σ_y : normal stresses and τ_{xy} : shear stresses). On a compliant joint, the bending moment may be caused from end loads (P, nP) and end moment (M_0) or a combination of both. When end loads are present, an axial and a shear stress will act on the compliant joint and the bending moment will generate a bending stress. The axial and bending stresses can be compressive

or tensile depending on the sign of the load and they are defined as

$$\sigma = \begin{cases} \frac{F_{axial}}{A}, & \text{axial stress} \\ \frac{M_{bending}y}{I}, & \text{bending stress} \end{cases} \quad (5.1)$$

where F_{axial} is the axial force, A is the area of the cross section of the beam, $M_{bending}$ is the bending moment, y is the distance of neutral axis to the point at which the stress is calculated for and I is the bending moment of inertia for the cross section. The maximum bending stress occurs at the farthest point from the neutral axis on a beam and it can be expressed as

$$\sigma_{max} = \frac{M_{bending}c}{I} \quad (5.2)$$

where c is the distance from the neutral axis to the outer surface of the beam. Shear stress is defined as

$$\tau = \frac{QF_{shear}}{Ib} \quad (5.3)$$

where Q is first moment of area, F_{shear} is shear force at the point of interest, I is moment of inertia for the cross section, b is the material thickness perpendicular to shear. The maximum shear stress occurs at the center point on a cantilever beam and can be expressed as

$$\tau = 1.5 \frac{F_{shear}}{A} \quad (5.4)$$

where A is the cross section area of the beam.

Let θ be the slope at any point on a cantilever beam subjected to combined end loads (P and nP) on its free end. The shear force (F_{shear}) and axial force (F_{axial}) at any point can be obtained by

$$\begin{aligned} F_{shear} &= P \cos \theta + nP \sin \theta \\ F_{axial} &= P \sin \theta - n \cos \theta. \end{aligned} \quad (5.5)$$

Principal stresses are the components of the stress tensor when the stress element is rotated with respect to a rotation angle in such a way that the shear stress components become zero and normal stress components are maximum. The

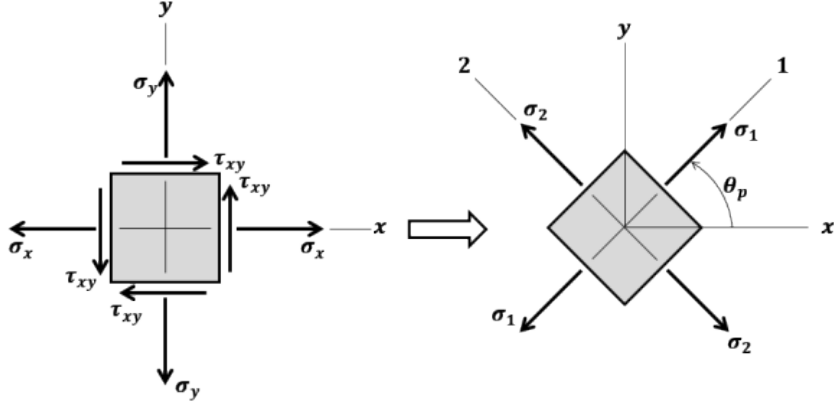


Figure 5.1: 2D planar stress element to 2D principal stress element transformation.

transformation to the principal axis can be seen in Figure 5.1. Principal stresses are

$$\sigma_{A,B} = \frac{\sigma_x + \sigma_y}{2} \pm \sqrt{\left(\frac{\sigma_x - \sigma_y}{2}\right)^2 + \tau_{xy}^2} \quad (5.6)$$

and the principal normal stresses can be found by order of magnitude

$$\begin{aligned} \sigma_1 &= \max(\sigma_A, \sigma_B, 0) \\ \sigma_3 &= \min(\sigma_A, \sigma_B, 0) \end{aligned} \quad (5.7)$$

and σ_2 is whichever of σ_A , σ_B and 0 is between σ_1 and σ_3 . The principal shear stress is

$$\tau_{max} = \left| \sqrt{\left(\frac{\sigma_x - \sigma_y}{2}\right)^2 + \tau_{xy}^2} \right| = \frac{\sigma_1 - \sigma_3}{2}. \quad (5.8)$$

The equivalent stress (σ_{eqv}) is defined by Tresca theory as

$$\sigma_{eqv} = \max(|\sigma_1 - \sigma_2|, |\sigma_2 - \sigma_3|, |\sigma_3 - \sigma_1|) \quad (5.9)$$

where σ_1 , σ_2 and σ_3 are principal stresses. The equivalent stress according to von Mises criterion for is

$$\sigma_{eqv} = \sqrt{\frac{(\sigma_1 - \sigma_2)^2 + (\sigma_2 - \sigma_3)^2 + (\sigma_3 - \sigma_1)^2}{2}} \quad (5.10)$$

or for 2D planar stresses

$$\sigma_{eqv} = \sqrt{\sigma_x^2 + \sigma_y^2 - \sigma_x \sigma_y + 3\tau_{xy}^2}. \quad (5.11)$$

5.2 Fatigue Failure

The fracture on a fatigue failure occurs in three stages. *Stage 1* is the initiation of one or more micro-cracks due to cyclic plastic deformation. Stage 1 cracks are not normally noticeable by naked eye. *Stage 2* progresses from micro-cracks to macro-cracks forming parallel fracture surfaces separated by longitudinal ridges. These surfaces can be wavy dark and light bands. During cyclic loading, these cracked surfaces open and close, rubbing together. *Stage 3* occurs during the final stress cycle when the remaining material cannot support the loads, resulting in a catastrophic, sudden, fast fracture. A stage 3 fracture can be brittle, ductile, or a combination of both [61].

Depending on the application, some compliant mechanisms may need to fulfill a life cycle of a few cycles, while other mechanisms are expected to fulfill thousands, millions of cycles before fatigue failure. The life cycle before fatigue failure is often classified in three categories named as *low-cycle*, *high-cycle* and *infinite cycle life*. Low-cycle is used for the life cycle range of $1 - 10^3$, high-cycle is used for range of $10^3 - 10^6$ life cycles, while infinite life cycle is used for more than 10^7 cycles which is also considered to be no fatigue failure happens with applied loads.

There are three well-known fatigue life methods used in design and analysis of fatigue failure to predict the life number of cycles to failure (N). These methods are called as *stress-life method*, *strain-life method* and *linear-elastic fracture mechanics method*. The most traditional method is the stress-life method, which tries to predict the number of life cycles to failure with respect to stress amplitude, is the easiest to implement for a wide range of design applications, has plenty of experimental readily available data, and can successfully predict high-cycle and infinite-cycle. However, it is the least accurate among other three methods, especially for low-cycle applications. The stress-life method is examined in detail in Section 5.3.

5.3 Fatigue Life Method

To determine the life number of cycles and fatigue strength of a material under influence of repeated or varying fatigue loads, sample specimens are subjected to loads of specified magnitudes while the cycles or reversed stresses are counted to failure. To obtain the fatigue strength or the life number of cycles of a material, plenty of experiments are needed because of the nature of fatigue theory. For instance, to obtain enough data to determine S-N curve for a metal up to an endurance of 10^8 cycles, minimum of 8 tests are required, in which the longer one will last for about two weeks if the speed of the machine is 5000 cycles per minute. With a single fatigue device, the total time required will be 8 or 10 weeks. [62].

The data obtained on fatigue strength experiments are plotted on S-N semi-log diagram. The x-axis of S-N diagram describes the number of cycles (N), while y-axis represents the fatigue strength (σ_f) for fully reversed loading. The S-N diagram is often used to express completely reversed stress cycles where the same magnitude of stress fully alternates between compression and tension.

For ferrous and many other materials, the S-N diagram becomes horizontal after a specific number of cycles. The stress corresponding to that point is called *endurance limit* (σ_e), where the number infinite life cycle begins, approximately between 10^6 and 10^7 . Some materials do not have an endurance limit to define the infinite cycle life such as Aluminum alloys and most polymers.

5.3.1 Stress Life Method of Polymers

The common fatigue criteria described in previous sections are mostly available for metals. Polymers, which are commonly used in compliant mechanisms and miniature robotics [5, 6], are harder to obtain fatigue characteristics because of material and operating factors, for which metals do not possess. Under cyclic loading conditions, the stress acting on polymers do not stay constant, it gradually decreases with number of cycles the load is applied. This phenomenon is called

cyclic softening represented in Figure 5.2. As time number of cycles increases under influence of cyclic loads, the high strain levels may cause failure that may result in crazing, cracking, stress whitening or micro-voiding [63].

The two main factors that affect the fatigue characteristics of polymers are classified as material and operating factors [63–65]. Material factors that affect fatigue resistance are:

- Surface notches
- Fillers and reinforcement
- Viscoelasticity
- Creep
- Stress relaxation
- Nonlinear elastic material properties
- Orientation of material.

The operating conditions that may affect fatigue endurance are:

- Mean stress
- Frequency of cyclic reversals
- Load waveform
- Variation of loading types
- Temperature.

Yet, apart from these factors atomic structure, molecular weight and surface quality can also affect fatigue endurance of polymers.

Since DuPont™ Kapton® polyimide film has good mechanical and fatigue properties, it is the most preferred compliant mechanism material in miniature robotic applications. In the rest of this work, Kapton® is considered as the main component to estimate fatigue life cycle of a compliant joint. Polyimides (PIs) are fabricated from aromatic diamines and aromatic dianhydrides and has excellent electrical, thermal, mechanical and chemical properties [65].

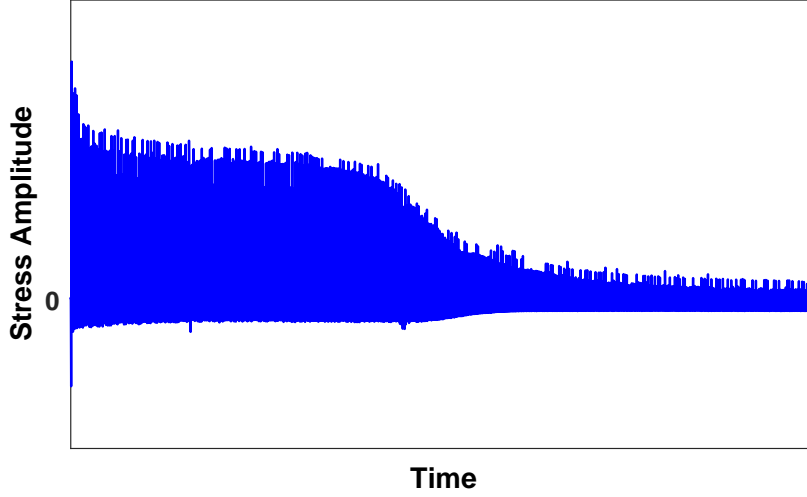


Figure 5.2: Variation of bending stress subjected on PET sheet joint material used in early stages of MinIAQ-I design is a good example of cyclic softening.

A compact constitutive equation for the stress-life (S-N) fatigue behavior of polymers is derived in Chandran's (2016) work on the basis of macroscopic crack growth mechanism [66]. Constitutive equations that gives the cyclic stress amplitude (σ_f) and number of cycles to failure (N_f) for fatigue at zero mean stress are given as

$$\sigma_f = \sigma_e + (\sigma_u - \sigma_e) \exp\left\{ -C_n(N_f)^{m_n} \right\} \quad (5.12)$$

and

$$N_f = \left[-\frac{1}{C_n} \ln\left(\frac{\sigma_a - \sigma_e}{\sigma_u - \sigma_e}\right) \right]^{1/m_n} \quad (5.13)$$

where σ_u is ultimate tensile strength of the material, σ_e is endurance limit of the material, C_n and m_n are constant parameters that are used for the prediction of S-N behavior of polymers according to experiments.

Figure 5.3 shows the estimated S-N diagram for Kapton[®] polyimide film which is used as compliant joint material in miniature robots. The stress-life diagram is approximated by using the parameters $\sigma_u = 231MPa$ [67], $\sigma_e = 50MPa$ [65], $C_n = 0.051$ and $m_n = 0.28$ for the constitutive equations given in Equations (5.12) and (5.13), the values of C_n and m_n parameters are estimated to give $\sigma_f = \sigma_u$ for $N = 0$ and $\sigma_f = \sigma_e$ for $N = 10^7$.

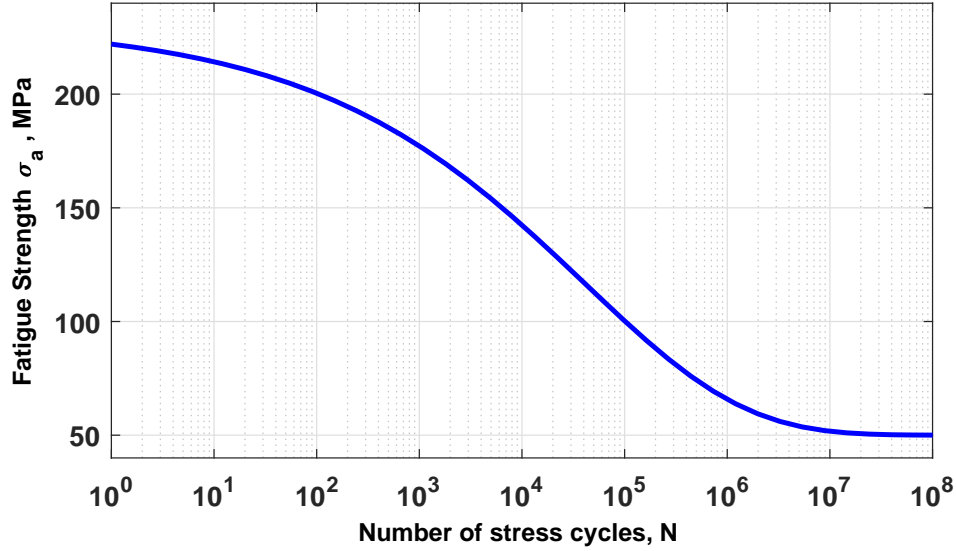


Figure 5.3: Estimated S-N diagram for Kapton[®] polyimide film with parameters $\sigma_u = 231MPa$, $\sigma_e = 50MPa$, $C_n = 0.051$ and $m_n = 0.28$.

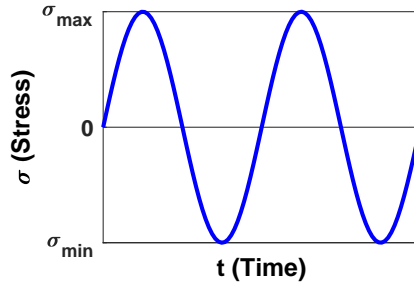
5.4 Fluctuating Stresses

Most fatigue data available are based on completely reversed loading with zero mean stress. In completely reversed loading, stress sinusoidally alternates between tensile and compressive stress whose magnitude of maximum tensile and compressive stresses are equal. This type of stress is shown in Figure 5.4(a). Fluctuating stresses that are not completely reversed may be encountered more in compliant mechanism applications. Figures 5.4(b) and 5.4(c) shows two different loading conditions for fluctuating stresses. Fluctuating stresses are defined by mid-range mean stress (σ_m) and the amplitude of sinusoidally alternating stress (σ_a) as seen in Figure 5.4. are calculated as

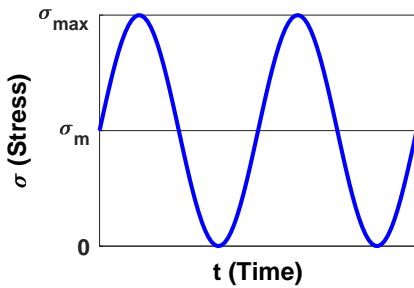
$$\sigma_m = \frac{\sigma_{min} + \sigma_{max}}{2}, \quad \sigma_a = \left| \frac{\sigma_{min} - \sigma_{min}}{2} \right| \quad (5.14)$$

and stress range (σ_r) is

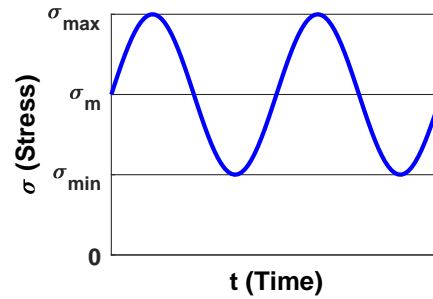
$$\sigma_r = \sigma_{max} - \sigma_{min} \quad (5.15)$$



(a)



(b)



(c)

Figure 5.4: Time-stress reversal examples. (a) Completely reversed sinusoidal stress. (b and c) Sinusoidal fluctuating stresses with different mean stress (σ_m).

where σ_{min} is the minimum stress while σ_{max} is the maximum stress in fluctuating reversal. Also the stress ratio (R) is

$$R = \frac{\sigma_{min}}{\sigma_{max}} \quad (5.16)$$

and the amplitude ratio (A) is

$$A = \frac{\sigma_a}{\sigma_m} = \frac{1 - R}{1 + R}. \quad (5.17)$$

5.4.1 Fatigue Failure Criteria for Fluctuating Stresses

In literature there are several methods available to predict fatigue failure for fluctuating stresses [61, 68, 69]. The *modified Goodman diagram* method is the most commonly used method to predict fluctuating stresses in fatigue theory illustrated in Figure 5.5. In this method, the mean stress (σ_m) is placed on the x-axis while all other stress elements are located on y-axis. The mean stress also

forms a 45° line starting from origin point. The modified Goodman diagram forms a safe zone envelope in which any alternating stress-mean stress combination that falls inside this failure envelope do not cause any failure.

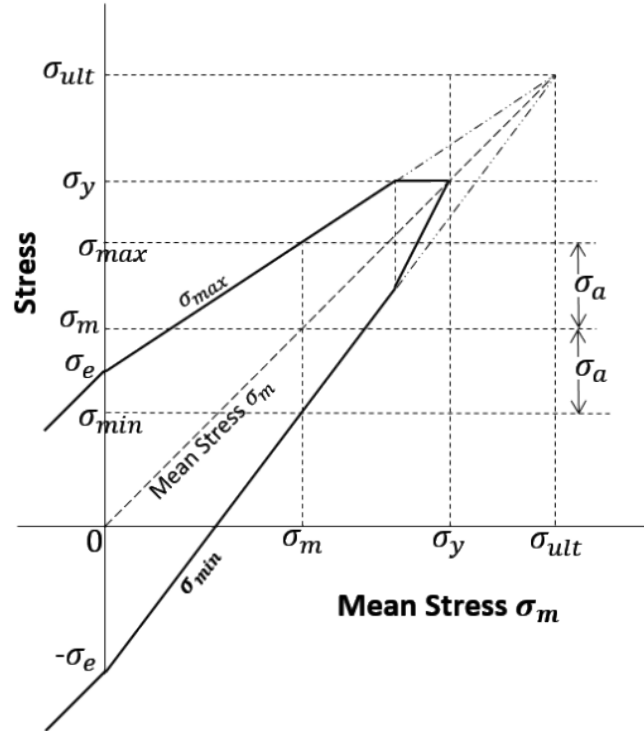


Figure 5.5: Modified Goodman diagram used to predict fatigue failure in fluctuating stresses.

In Figure 5.6 stresses are plotted for Goodman failure method along with four additional failure criteria methods where x-axis is mean stress (σ_m), while y-axis is alternating stress (σ_a). These failure criteria are commonly used in fatigue analysis and engineering design considerations.

The failure equation for the modified Goodman line is

$$1 = \frac{\sigma_a}{\sigma_e} + \frac{\sigma_m}{\sigma_{ult}}, \quad (5.18)$$

same way, the failure equation for the Soderberg line is

$$1 = \frac{\sigma_a}{\sigma_e} + \frac{\sigma_m}{\sigma_y}, \quad (5.19)$$

failure equation for Gerber line is

$$1 = \frac{\sigma_a}{\sigma_e} + \left(\frac{\sigma_m}{\sigma_{ult}} \right)^2, \quad (5.20)$$

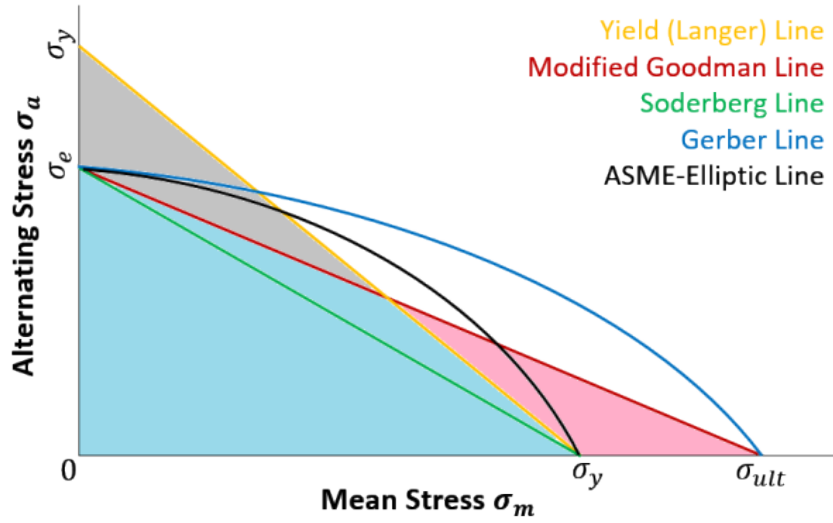


Figure 5.6: Fatigue diagram for various criteria methods to relate mean stresses (σ_m) to stress amplitude (σ_a) where σ_y is yield strength, σ_e is endurance limit, σ_{ult} is ultimate strength. **Turquoise**: Infinite life area, **Pink**: Yielding area and **Grey**: Finite life area

failure equation for ASME elliptic line is

$$1 = \left(\frac{\sigma_a}{\sigma_e}\right)^2 + \left(\frac{\sigma_m}{\sigma_y}\right)^2 \quad (5.21)$$

and finally, the failure equation for Langer first cycle yielding is

$$1 = \frac{\sigma_a}{\sigma_y} + \frac{\sigma_m}{\sigma_y}. \quad (5.22)$$

The modified Goodman criterion is more conservative than Gerber method and Soderberg method is the most conservative method among other fluctuating stress failure criteria.

5.4.2 Fatigue Failure Criteria for Fluctuating Stresses of Polymers

In Section 5.3.1 fatigue failure prediction for fully reversed loading are represented for polymers based on Chandran's (2016) work [66]. In this work the compact constitutive equation is modified in order to satisfy fluctuating loads. Number of

cycles to failure (N_{fR}) for any stress ratio R is given by the equation

$$N_{fR} = \left[-\frac{1}{C_n} \ln \left(\frac{\sigma_{maxR} - \{\sigma_{aeR-1} + \sigma_{maxR}(1+R)/2\}}{\sigma_u - \{\sigma_{aeR-1} + \sigma_{maxR}(1+R)/2\}} \right) \right]^{1/m_n} \quad (5.23)$$

where σ_{aeR-1} is the stress amplitude at endurance limit for $R = -1$, σ_{maxR} is the maximum stress of the fatigue cycle at any R , σ_u is the ultimate tensile strength of the material, C_n and m_n are constant parameters that are used for the prediction of S-N behavior of polymers according to experiments.

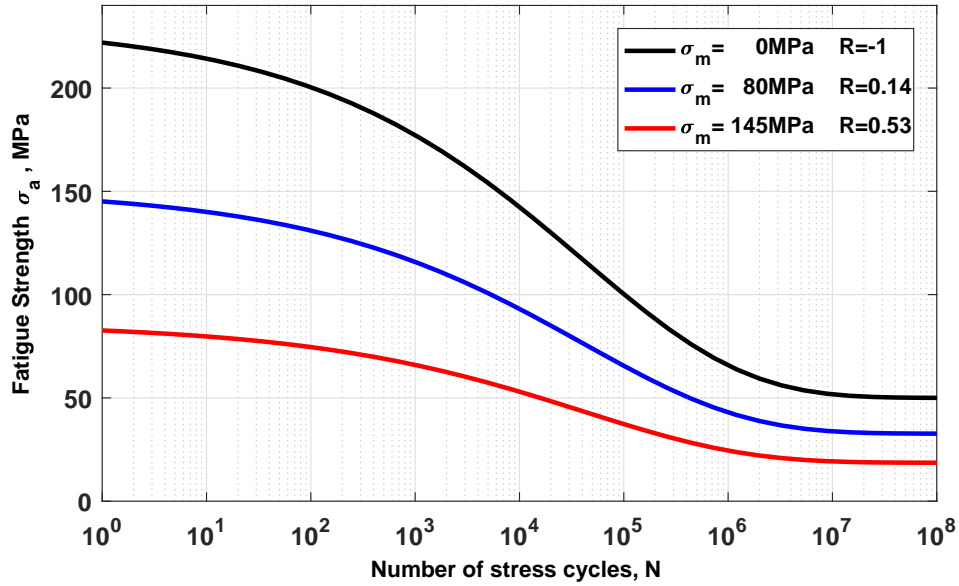


Figure 5.7: Estimated mean stress effect on the S-N diagram for Kapton[®] polyimide film for different mean stress (σ_m) and stress ratios (R) with Parameters $\sigma_u = 231MPa$, $\sigma_e = 50MPa$, $C_n = 0.051$ and $m_n = 0.28$.

5.5 Combination of Loading Modes

The easiest loading type is a completely reversed and single stress type to predict fatigue life which is presented on a S-N diagram, by plotting the number of life cycle with its corresponding alternating stress. In this loading case, mean stress (σ_m) must be zero and only a single type of loading is considered and it is generally bending stress. Then, fluctuating stresses can be predicted with respect to their

mean (σ_m) and alternating (σ_a) stresses by using modified Goodman, Gerber, ASME-elliptic, Yield or Soderberg failure criterion. Again, in these criteria only a single load is allowed. Finally, any combination of different loading types may be applied including bending, torsion, and axial stresses. The combination of these loading modes are examined in this section.

Combination of fluctuating stress loading modes acting on a component are evaluated by following these steps:

- The stress element of each type of loading is considered into its alternating (σ_a) and mean (σ_m) stresses.
- Equivalent von Mises stress can be obtained for the mean (σ'_m) and alternating (σ'_a) stress components from following equations

$$\begin{aligned}\sigma'_a &= \left\{ \left[(\sigma_a)_{bending} + \frac{(\sigma_a)_{axial}}{0.85} \right]^2 + 3 \left[(\tau_a)_{torsion} \right]^2 \right\}^{1/2} \\ \sigma'_m &= \left\{ \left[(\sigma_m)_{bending} + (\sigma_m)_{axial} \right]^2 + 3 \left[(\tau_m)_{torsion} \right]^2 \right\}^{1/2} .\end{aligned}\tag{5.24}$$

It should be noted that the alternating component of the axial load is divided by its load factor (0.85). The load factor for alternating component of bending stress equals to 1. Therefore, alternating component of torsional stress is not divided by its load factor (0.59) because it was taken into account in von Mises transformation.

- The last step is choosing any fatigue failure criterion (Langer, modified Goodman, Soderberg, Gerber or ASME-elliptic) and applying failure equation for that criteria.

Chapter 6

Optimization

The basis of multi-objective optimization problem is presented in this chapter. First, optimization problems are defined based on kinematic models discussed in Chapter 4, a single joint subjected to fully reversed bending loads and multi-joint MinIAQ-I mechanism that is under influence of combined fluctuating loading modes, then an appropriate optimization algorithm is chosen. Design variables are defined based on stress magnitudes for these optimization problems through upper and lower bounds required for design limitations.

6.1 Optimization Algorithm

In engineering design and analysis, there are several methods available for optimization of linear and nonlinear problems [70–72]. MatLab offers commonly used methods in build-in *Optimization Toolbox*. This toolbox offers optimization algorithms for linear, quadratic, integer, and nonlinear for single or multi objective problems. Among readily available functions, `fminimax` multi-objective function is selected for optimization which minimizes the worst-case value of a set of multi-variable functions, subjected to linear or nonlinear constraints.

The optimization problem solved by the `fminimax` multi-objective algorithm finds

the minimum of a problem specified by

$$\min_x \max_i F_i(x) \text{ such that } \begin{cases} c_i(x) & \leq 0, i = 1 \dots m \\ ceq_i(x) & = 0, i = m + 1 \dots mt \\ A.x & \leq b \\ Aeq.x & = beq \\ lb & \leq x \leq ub \end{cases} \quad (6.1)$$

where x is design variables, $c(x)$ is the nonlinear inequality constraint function, $ceq(x)$ is the nonlinear equality constraint function, m is the number of nonlinear inequality constraints, mt is the total number of nonlinear constraints, A is matrix, b is vector and lb and ub are lower and upper bounds on the design variables in x .

fminimax minimizes the optimization functions $F(x)$ to linear inequalities $A.x \leq b$, linear equalities $Aeq.x \leq beq$, nonlinear inequalities c and nonlinear equality ceq constraints.

6.2 Optimization Problem

By randomly defining geometric parameters to achieve a desirable mechanism, the kinematic models of rigid linkage and compliant joint mechanisms discussed in Chapter 4 are used to obtain trajectory path of a leg and stresses acting on compliant joints. In order to get an ideal stress life cycle, trajectory, load capacity for applied motor torque, joint cross-section and geometric parameters an optimization is necessary. The parameters that influence these conditions are determined and optimization is done in two stages. *First stage* is based on a kinematic optimization to achieve an ideal trajectory by manipulating the joint locations [6]. Once joint positions and linkage lengths are obtained from first stage optimization, *second stage* optimization problem is defined for compliant joints which is the main concern of this work.

In *second stage* a compliant mechanism optimization is done by using the kinematic parameters obtained in *first stage* and geometric parameters of compliant joints are altered in optimization based on objective function. As geometric parameters of compliant joints change during optimization, the output trajectory path also drifts away from the desired trajectory obtained in *first stage*. To reduce or prevent the drift in trajectory path, the input revolute joint mechanism obtained in *first stage* is considered as small-length flexure mechanism, which is a simple model used to analyze the deflection of flexible members using rigid body components wherein compliant joints are small in length compared to the rigid linkages [73]. Small-length flexure method gives satisfying trajectory results as long as the compliant joint lengths are small compared to rigid sections, if higher trajectory accuracy is desired in optimization pseudo-rigid-body models [44–52] can be easily implemented into *second stage* optimization.

6.2.1 MinIAQ-I Mechanism Optimization

The kinematic model discussed in Section 4.2 is used to obtain optimum design parameters. The model is parametrized in terms of the joint geometric variables that affect the stress acting on them.

$$\mathbf{X} = \{b1 \ L1 \ b2 \ L2\}^T \quad (6.2)$$

where $b1$ and $L1$ are width and length parameters of Joint 1, while $b2$ and $L2$ are width and length parameters of Joint 2. It should be noted that thickness is not considered as an optimization variable here, because joint material Kapton[®] PI film can be found in standard thicknesses such as 25, 50, 100 μm . Therefore, choice of material thickness is left to designer. Initial set of design variables, \mathbf{X}^0 and lower and upper bounds, \mathbf{lb} and \mathbf{ub} are defined along with desired kinematic parameters (L_{J1J2} , L_{J2E} , L_{EI} , L_{EF} , L_{J1H} , L_{GH} and L_{GI}), see Figure 6.1(a).

To reduce the drift in optimized compliant mechanisms trajectory path the following relations are defined for compliant mechanism, see Figure 6.1(b)

$$\begin{aligned}
L_{AH} &= L_{J1H} + \frac{L_1}{2} \\
L_{BC} &= L_{J1J2} - \frac{L_1}{2} - \frac{L_2}{2} \\
L_{DE} &= L_{J2E} - \frac{L_2}{2}
\end{aligned} \tag{6.3}$$

The **fminimax** optimization procedure starts here to minimize the following objective functions

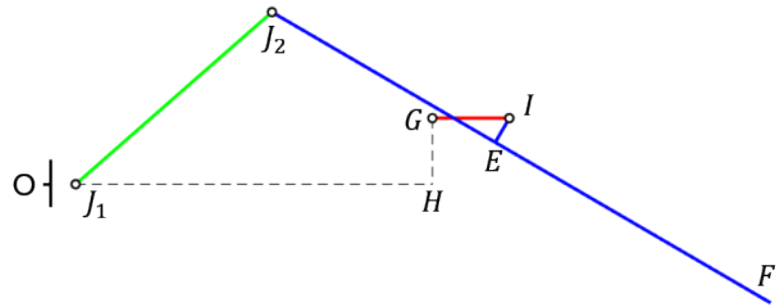
$$\begin{aligned}
f_1(\mathbf{X}) &= \sigma'_{m1} \\
f_2(\mathbf{X}) &= \sigma'_{m2}
\end{aligned} \tag{6.4}$$

where σ'_{m1} and σ'_{m2} are the mean stresses of the fluctuating loads acting on joints 1 and 2. The constraint equations of the optimization problem are

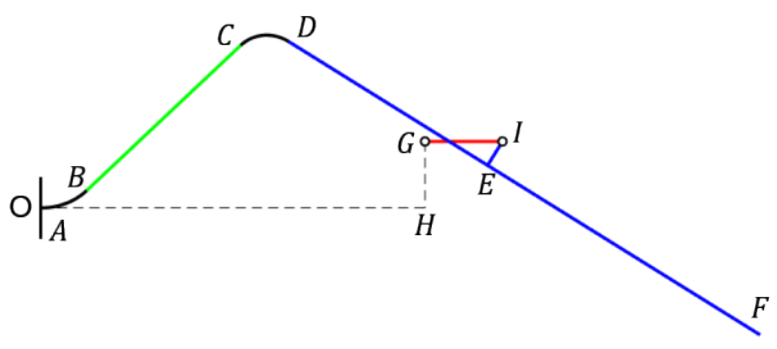
$$\begin{aligned}
c_1(\mathbf{X}) &= \sigma'_{a1} - \sigma_{aLim} \\
c_2(\mathbf{X}) &= \sigma'_{a2} - \sigma_{aLim} \\
ceq_1(\mathbf{X}) &= \sigma'_{m1} - \sigma'_{m2} \\
ceq_2(\mathbf{X}) &= b_1 - b_2
\end{aligned} \tag{6.5}$$

Here $c_1(\mathbf{X})$ and $c_2(\mathbf{X})$ inequality functions try to minimize the difference in stress amplitudes and limiting stress for joints as much as possible, while $ceq_1(\mathbf{X})$ tries to make the mean stresses acting on joints equal and $ceq_2(\mathbf{X})$ tries to equalize the width of joints (since both joints are on the same leg, this constraint is considered to reduce design dissimilarities).

The optimizations results with the compliant joint parameters: b_1 , L_1 , b_2 , L_2 and new kinematic parameters: L_{AH} , L_{BC} , L_{DE} as seen on the compliant mechanism shown in Figure 6.1(b). Two samples of optimization algorithm convergence plots can be seen in Figure 6.2.

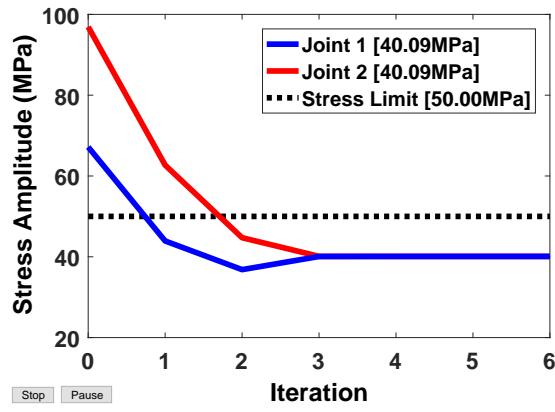


(a)

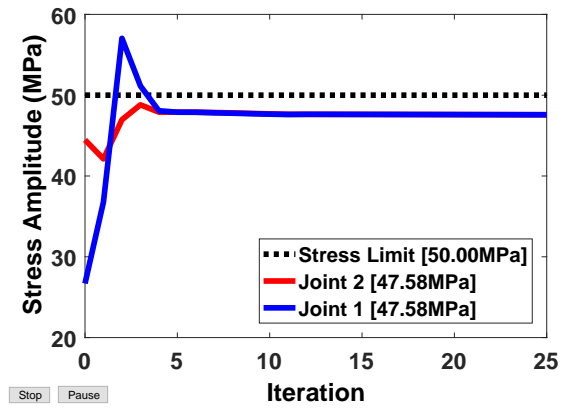


(b)

Figure 6.1: (a) Input small-length flexural joint mechanism. (b) Output optimized compliant joint mechanism.



(a)



(b)

Figure 6.2: Optimization convergence examples for MinIAQ-I mechanism for different thickness and stress amplitudes. (a) 75 μm (b) 100 μm Kapton[®] PI film.

Chapter 7

Experimental Results and Discussion

In this chapter, kinematic analysis of compliant joint solutions that were derived in Chapter 4 are verified with experimental results for controlled joint parameters of thickness, length, width and vertical point load. Then another experiment is done in order to confirm the deflection of an input torque can generate on a compliant leg mechanism. Finally, trajectory of MinIAQ-I's mechanism is compared for compliant, small-length flexure and revolute joint kinematic analysis methods.

7.1 Parametric Joint Experiments

The results in this section shows the variation of force with geometric parameters (thickness, length and width) of compliant joint and vertical point-load acting on the free end of the leg. Compliant joints of thicknesses 25, 50, 75 and 125 μm , lengths of 2, 3, 4, 6 and 12 mm, widths of 2, 4, 6, 8 and 10 mm and vertical loads of 0.76, 3.08, 6.73 and 10.52 grams are considered. For each case, vertical force (P) applied to the fixed end and the end slope (θ_0) are obtained for large deflection elliptic integral kinematic analysis and from experimental results. Test setup

used for experiments can be seen in Figure 7.1 with compliant leg mechanism attached to a load sensor. The results are presented in later subsections with the corresponding parameters.

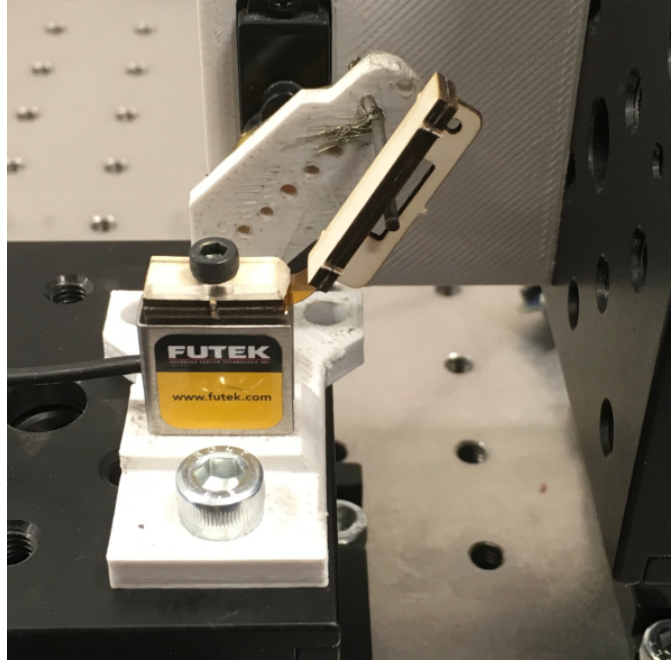


Figure 7.1: Experiment setup used to obtain vertical force readings with the deflection of leg.

7.1.1 Thickness

To observe the effect of thickness (t) of a compliant joint on the vertical force (P), 4 mm long and 6 mm wide specimens are used with varying thicknesses of 25, 50, 75 and 125 μm . It can be seen in Figure 7.2 that the magnitude of vertical force acting on the fixed end of the cantilever beam increases with the thickness. When the end slope (θ_0) reaches 90° , all of the vertical force lines intersect with each other and changes sign. By paying close attention to the ordinate of this intersection point, it is clear that the vertical force is equal to the weight of the rigid linkage arm ($m_{arm}g$), which is -3.07×10^{-3} Newtons.

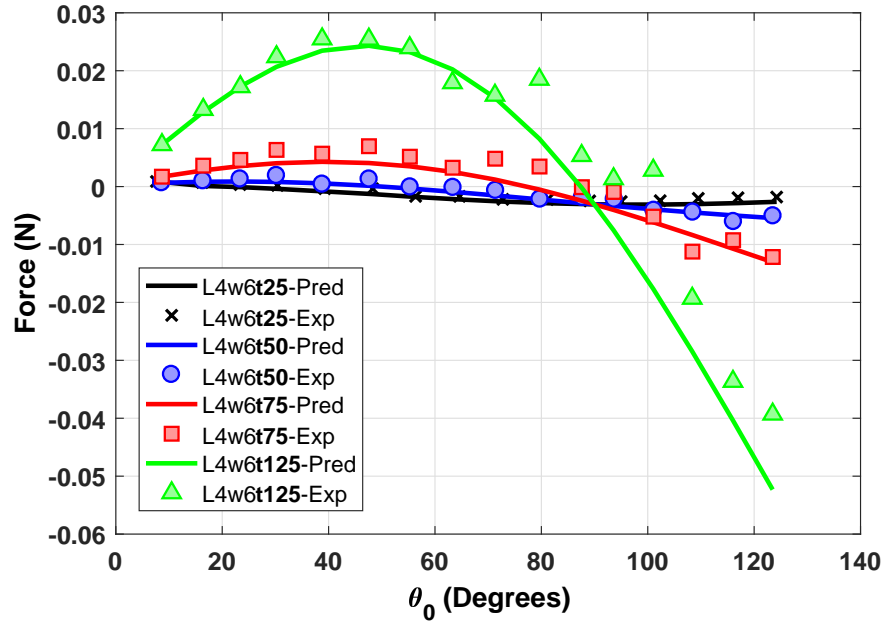


Figure 7.2: Vertical force (P) versus end slope (θ_0) for thicknesses of 25, 50, 75 and 125 μm Kapton[®] PI film.

In Chapter 3, the large deflection beam theory suggested that the end moment required to bend a cantilever beam is proportional to end slope (θ_0) and moment of inertia of the cross section of the beam (I) by the relation $M_0 = \frac{\theta_0 EI}{L}$. The input crank torque to excite this mechanism for varying thicknesses of 25, 50, 75 and 125 μm can be seen in Figure 7.3. Since the moment of inertia of a rectangular cross-section beam is defined as $I = \frac{1}{12}bt^3$, it is clear that a change in thickness will affect the required moment more than other parameters.

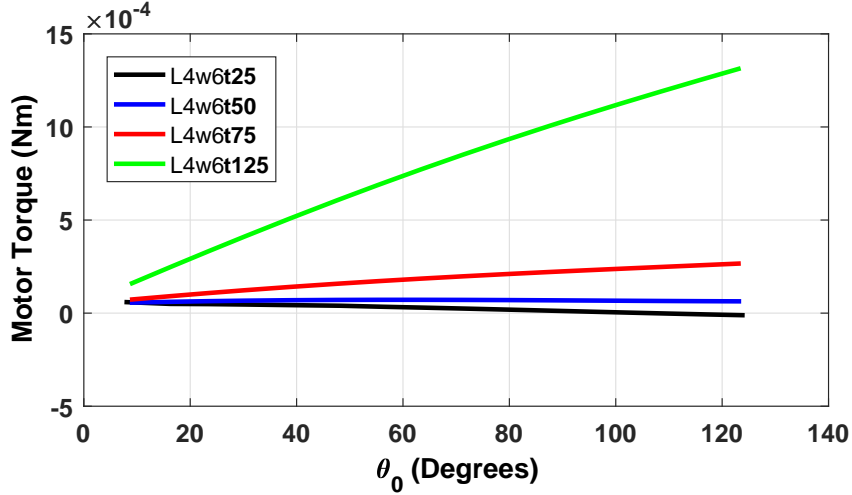


Figure 7.3: Input crank torque (T_{in}) versus end slope (θ_0) for thicknesses of 25, 50, 75 and 125 μm Kapton[®] PI film.

7.1.2 Length

To observe the effect of length (L) of a compliant joint on the vertical force (P), 2, 3, 4, 6 and 12 mm long specimens are used for the same thickness and width. In Figure 7.4, it is observed that the applied force increases with the decreasing length of the compliant joint. In Figure 7.5 input crank torque (T_{in}) versus end slope (θ_0) is plotted. Results in this figure agree with the equation for beam with end load $M_0 = \frac{\theta_0 EI}{L}$, which suggests that the moment required for given end slope is inversely proportional to length of the cantilever beam. Another point to be aware of is with changing length, the end slope (θ_0) also changes. That kind of behavior is not encountered in any parameter except length. This phenomenon can be explained by the change of vertical and horizontal deflection components of the end point as the length parameters changes, based on the eqs. (3.24), (3.27), (3.48), (3.52), (3.77) and (3.78).

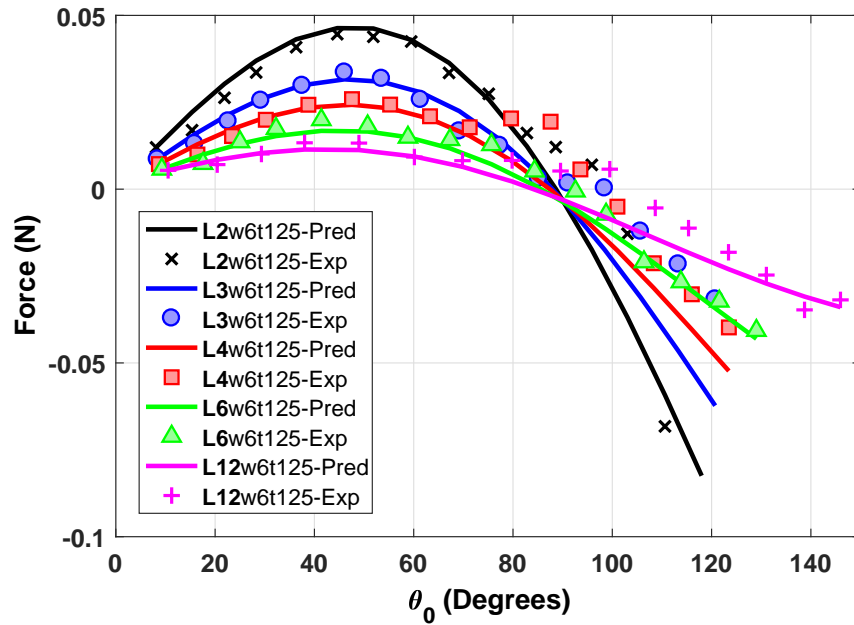


Figure 7.4: Vertical force (P) versus end slope (θ_0) for 2, 3, 4, 6 and 12 mm long Kapton[®] PI film.

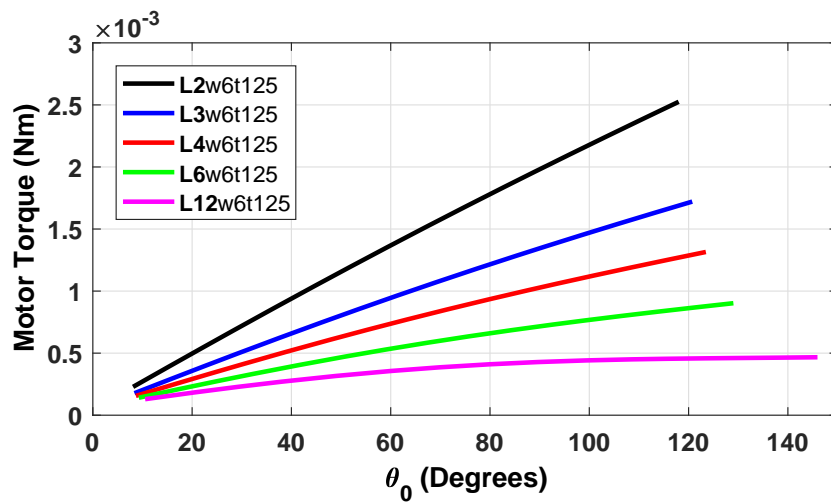


Figure 7.5: Input crank torque (T_{in}) versus end slope (θ_0) for 2, 3, 4, 6 and 12 mm long Kapton[®] PI film.

7.1.3 Width

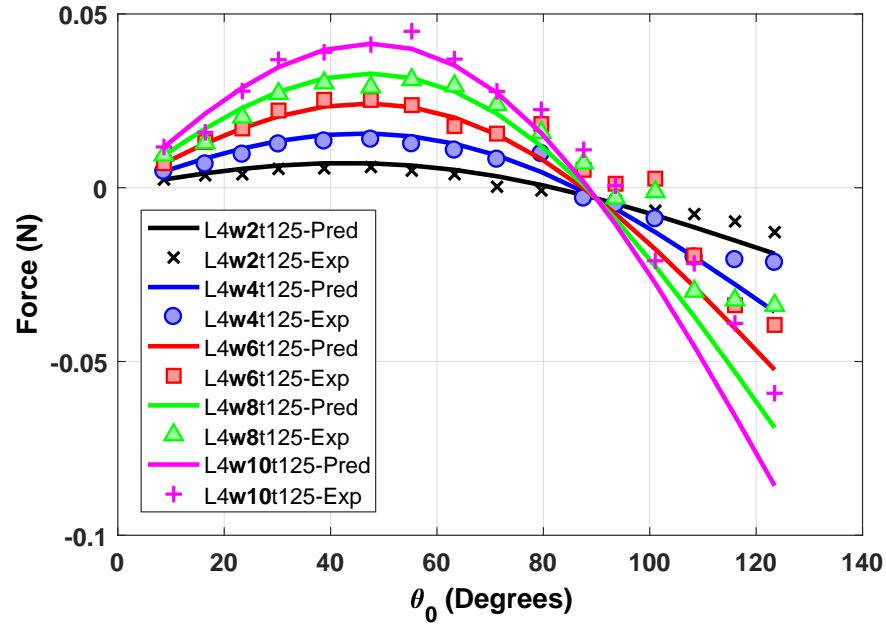


Figure 7.6: Vertical force (P) versus end slope (θ_0) for 2, 4, 6, 8 and 10 mm wide Kapton[®] PI film.

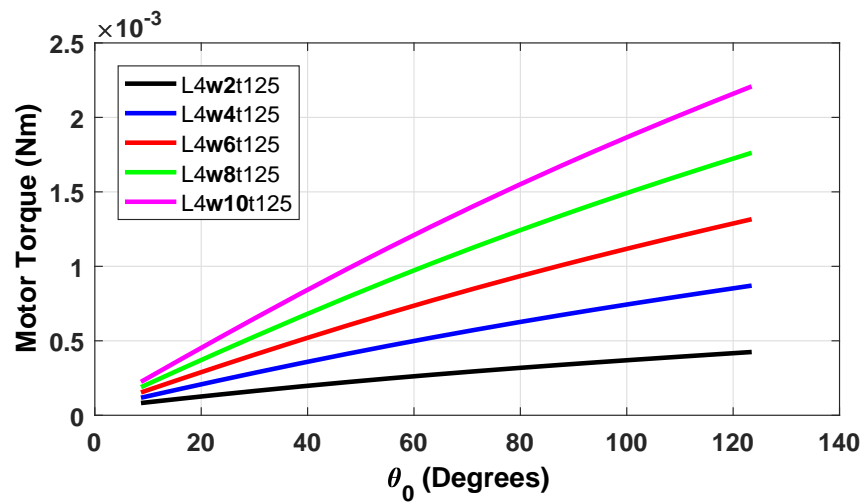


Figure 7.7: Input crank torque (T_{in}) versus end slope (θ_0) for 2, 4, 6, 8 and 10 mm wide Kapton[®] PI film.

For the same length (L) and thickness (t), but varying the parameter width (b), 2, 4, 6, 8 and 10 mm wide specimens are used. It is observed that the applied vertical force linearly increases with the width that can be seen in Figure 7.6, which yields similar results to varying the parameter thickness. By referring to the moment of inertia of a rectangular cross-section beam equation $I = \frac{1}{12}bt^3$, we can conclude that unlike thickness the width(b) and applied moment (M_0) is linear, see Figure 7.7.

7.1.4 Vertical Point Load

Vertical external point load of 0.76, 3.08, 6.73 and 10.52 grams are subjected to the tip of the leg (D_y) with fixed thickness, width and length to observe external loads effect on the vertical force acting to the fixed end of compliant joint (P). Experimental and large deflection elliptic integral kinematic solution can be seen in Figure 7.8 for vertical force versus end slope. Here, all of the lines intersect at approximately 45° end slope. The input crank torque (T_{in}) versus end slope (θ_0) for varying vertical end loads are plotted in Figure 7.9.

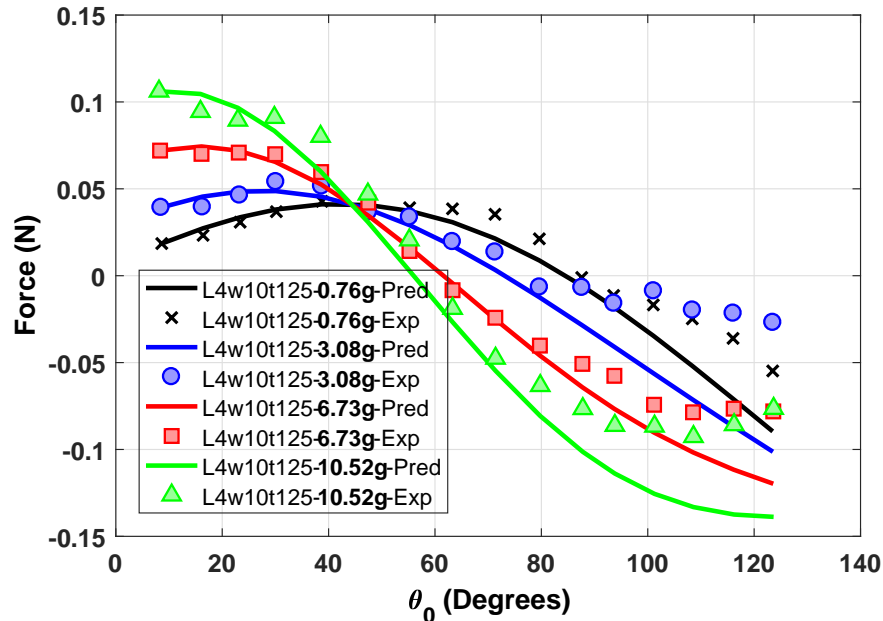


Figure 7.8: Vertical force (P) versus end slope (θ_0) for vertical loads of 0.76, 3.08, 6.73 and 10.52 grams acting on the tip of the leg.

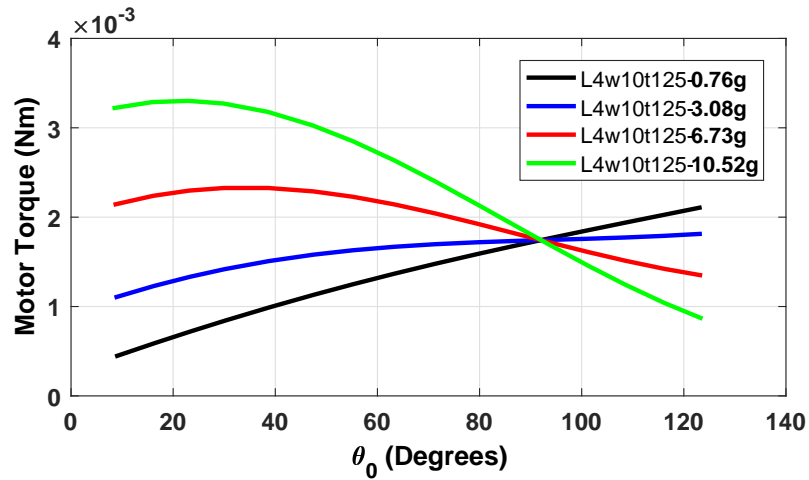


Figure 7.9: Input crank torque (T_{in}) versus end slope (θ_0) for vertical loads of 0.76, 3.08, 6.73 and 10.52 grams acting on the tip of the leg.

7.2 Torque Limit Experiment

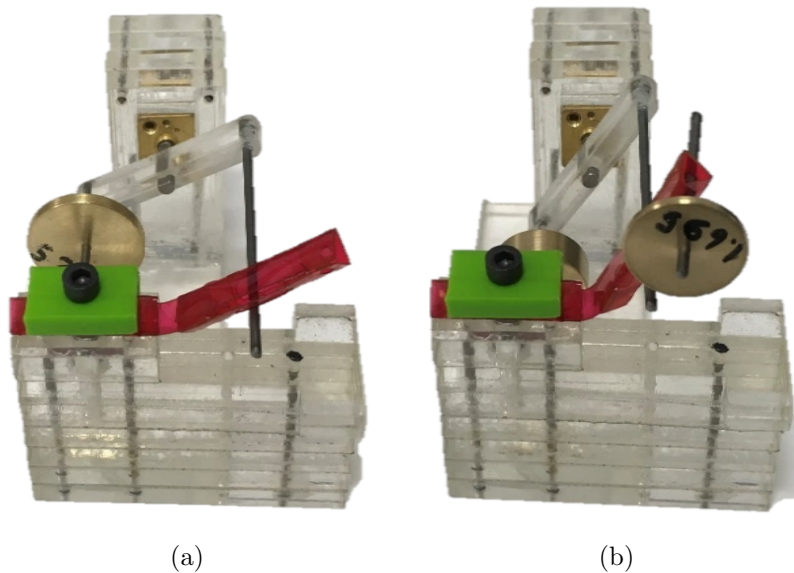


Figure 7.10: Limiting input crank torque experiment setup. (a) No load attached on the tip of the leg. (b) Vertical load attached on the tip of the leg.

In this section a test setup is used to check the validity of required limiting torque for unloaded and vertically loaded legs. Instead of a motor, a counterweight is used to create a torque on input crank, see Figure 7.10.

Table 7.1: Torque limit experimental versus large deflection kinematic prediction results when no loads acting to tip of the leg (see Figures 4.1 and 7.10(a)).

Counter Weight to Generate Torque (g)	Large Deflection Kinematic Prediction of End Slope (θ_0)	Experimental Result of End Slope (θ_0)
1.69	19.9	22
2.68	30.9	30
5.25	48.4	41
7.69	59.3	51
10.54	67.9	61
13.26	72.2	66
15.98	76.4	69

Table 7.2: Torque limit experimental versus large deflection kinematic prediction results when vertical force is applied on the tip of the leg ($Dy = 1.7g$ see Figures 4.1 and 7.10(b)).

Counter Weight to Generate Torque (g)	Large Deflection Kinematic Prediction of End Slope (θ_0)	Experimental Result of End Slope (θ_0)
3.11	Error	not enough to lift
4.89	22.0	22
5.19	25.4	25
6.29	36.4	33
8.11	50.0	43
10.15	59.2	53

7.3 Trajectory Paths of Compliant, Small-Length Flexure and Revolute Joint Mechanisms

In this section MinIAQ-I's trajectory paths for three different kinematic analysis methods are plotted and compared as seen on Figure 7.11. Kinematic analysis calculations for small-Length flexure and revolute joint mechanisms are relatively simple and straightforward to obtain a closed-form solution, but these methods have lower trajectory accuracy while compliant joint trajectories are the main concern and with the increasing joint length, trajectory accuracy drops significantly. On the other hand, while compliant joint kinematic analysis requires more time and computational power to converge to a solution, the output trajectory agrees very well with experimental results and much more faster than FEA methods [41]. Therefore compliant joint kinematic analysis compensates the solution time with satisfactory results, see Figure 7.11.

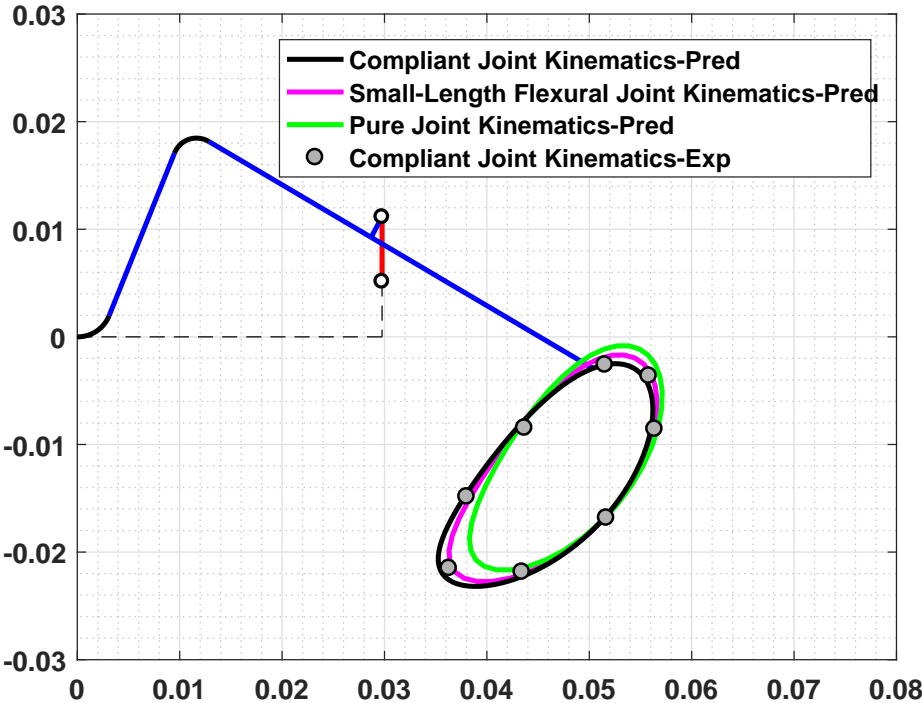


Figure 7.11: MinIAQ-I trajectory paths for compliant joint, small-length flexural joint and revolute joint kinematic analysis methods.

Chapter 8

Conclusion and Future Work

Initially, this thesis introduced a new foldable miniature quadruped robot, *MinIAQ*, manufactured from a single A4 PET sheet. In order to increase the rigidity of the main body frame, "T-shaped" folds are introduced along with tab and slot fasteners. Each leg of this robot is separately actuated by four small DC motors which lack encoders. To control the speed and position of each leg, a custom 3D encoder is introduced. The final state of the robot is untethered and weighs approximately 23 grams and walks with a speed of 0.65 Bodylengths/sec for 30 minutes with a fully charged 150 mAh LiPo single cell battery.

The main objective of this thesis was to address the challenges of compliant mechanisms used in *MinIAQ* and other miniature robotic applications, which have load carrying capacity limitations and suffer from fatigue failure under continuous cyclic loading conditions of flexure joints. To overcome these issues the flexible segments are modeled as cantilever beams that are subjected to combined loads and moment on free end and fixed from the other end. Nonlinear Bernoulli–Euler beam theory is used with the help of elliptic integrals to model these flexible segments. Elliptic integral approach is known as the most accurate to analyze large deflections of thin beams in compliant mechanisms [41], with very rapid convergence rate unlike FEA methods. Nonlinear large deflection elliptic solvers are able to give deflection, slope, moment, sectional forces and stresses

acting at any point on flexure beam. Based on this information an insight can be made about what and where is the main cause of the fraction. The vast majority of the equivalent stress acting on the flexure beam comes from the stress created from bending moment, while axial and shear stresses have small effect on the equivalent stress. This statement suggests that with the increasing thickness of the flexure beam, bending stress also increases, which reduces fatigue life but increases the load capacity. Another important parameter that effects the stress of a flexure beam is its length, which can be stated clearly by referring the beam theories.

Kinematic modeling of compliant mechanisms was done based on large deflection elliptic integrals by means of combining the loop closure and static equilibrium equations. In order to check the validity of kinematic models based on elliptic integrals, a simple single joint compliant leg mechanism was used. The results of force generated by compliant joint showed that elliptic integral kinematic solution predictions were greatly in agreement with experimental results. After that point, kinematic model of compliant joints that used in MinIAQ-I and II are done based on elliptic integrals. With these kinematic models, we obtained the trajectory of the tip of the leg, maximum load carrying capacity with respect to limiting material properties and motor torque applied to the crank. The main advantage of elliptic integral kinematic analysis is that the trajectory of the tip of the leg noticeably differs from traditional revolute joint kinematic analysis. Although it lasts longer to converge to a solution, the compliant mechanism elliptic integral kinematic analysis gives a much accurate solution. If the trajectory path is very sensitive for a compliant mechanism application (and it often is the case for miniature robots), it is vital to use elliptic solution in design stage.

By investigating the combinations of loading modes in fatigue theory, equivalent mean and equivalent alternating stresses are obtained for a cycle from the results of elliptic integral kinematic models. The number of cycles before failure is obtained from these mean and alternating stresses using the physical theory of fatigue for the mechanical fatigue behavior of polymers approach developed by Chandran [66] for Kapton[®] polyimide film.

The optimization problem is defined based on geometric parameters of joints of MinIAQ-I and II mechanisms. Multi-objective optimization algorithm requires a traditional revolute joint mechanism and replaces revolute joints with compliant joints and by changing the geometric parameters of joints and rigid links gives the desired number of cycles before failure. The key feature of the optimization algorithm is that it uses small length flexure joint theory to replace revolute joints with compliant joints at every iteration during optimization, while keeping the output trajectory path as close as to the desired path.

There is still space for improvements for the work included in this thesis. The walking performance of miniature foldable robot, MinIAQ, can be improved by adding a pad to improve the friction by increasing the surface area between the tip of the leg and ground or replacing the tip with another material that has a better friction performance. Also, a laminate of carbon fiber composite and thin polyimide film can be used as structural element instead of using thin PET films and folding them into triangular beams or "T-folds" to form rigid frames.

To further explore the failure modes of flexure hinges used in compliant mechanisms their cross-sectional shapes can be altered. In this work, only rectangular flexure beams are modeled and used in experiments. Additional investigations can be done on corner filleted, elliptic arc flexure hinges or other ways to relieve the distributed stress on the joint as a future work. Also in real life applications, compliant joints can undergo torsion moment that causes buckling in flexure segments, these nonlinearities can be further investigated. The optimization algorithm used to optimize the mechanism can take from minutes to several hours depending on the application sensitivity and number of geometric parameters due to nonlinear elliptic integral solution. Pseudo-rigid-body 3R models, can be used to speed up the process, which comprises of four rigid links joined by three revolute joints and three torsion springs, but the end results remains to be seen and may not be as accurate as elliptic integral solutions. The accuracy and time required is a trade off for this case.

Bibliography

- [1] O. Ozcan, A. T. Baisch, D. Ithier, and R. J. Wood, “Powertrain selection for a biologically-inspired miniature quadruped robot,” in *2014 IEEE International Conference on Robotics and Automation (ICRA)*, pp. 2398–2405, IEEE, 2014.
- [2] J. M. Bustillo, R. T. Howe, and R. S. Muller, “Surface micromachining for microelectromechanical systems,” *Proceedings of the IEEE*, vol. 86, no. 8, pp. 1552–1574, 1998.
- [3] J. Whitney, P. Sreetharan, K. Ma, and R. Wood, “Pop-up book mems,” *Journal of Micromechanics and Microengineering*, vol. 21, no. 11, p. 115021, 2011.
- [4] R. S. Pierre and S. Bergbreiter, “Gait exploration of sub-2 g robots using magnetic actuation,” *IEEE Robotics and Automation Letters*, vol. 2, pp. 34–40, Jan 2017.
- [5] C. Karakadioğlu, M. Askari, and O. Özcan, “Design and operation of miniaq: An untethered foldable miniature quadruped with individually actuated legs,” in *Advanced Intelligent Mechatronics (AIM), 2017 IEEE International Conference on*, pp. 247–252, IEEE, 2017.
- [6] M. Askari, C. Karakadioğlu, F. Ayhan, and O. Özcan, “Miniaq-ii: A miniature foldable quadruped with an improved leg mechanism,” in *2017 IEEE International Conference on Robotics and Biomimetics (ROBIO)*, IEEE, 2017.
- [7] A. F. Güç, M. A. I. Kalın, C. Karakadioğlu, and O. Özcan, “C-quad: A miniature, foldable quadruped with c-shaped compliant legs,” in *2017 IEEE*

- International Conference on Robotics and Biomimetics (ROBIO)*, IEEE, 2017.
- [8] A. M. Hoover, E. Steltz, and R. S. Fearing, “Roach: An autonomous 2.4 g crawling hexapod robot,” in *Intelligent Robots and Systems, 2008. IROS 2008. IEEE/RSJ International Conference on*, pp. 26–33, IEEE, 2008.
- [9] R. Wood, S. Avadhanula, R. Sahai, E. Steltz, and R. Fearing, “Microrobot design using fiber reinforced composites,” *Journal of Mechanical Design*, vol. 130, no. 5, p. 052304, 2008.
- [10] J. Rossiter and S. Sareh, “Kirigami design and fabrication for biomimetic robotics,” in *SPIE Smart Structures and Materials+ Nondestructive Evaluation and Health Monitoring*, pp. 90550G–90550G, International Society for Optics and Photonics, 2014.
- [11] C. D. Onal, R. J. Wood, and D. Rus, “Towards printable robotics: Origami-inspired planar fabrication of three-dimensional mechanisms,” in *Robotics and Automation (ICRA), 2011 IEEE International Conference on*, pp. 4608–4613, IEEE, 2011.
- [12] R. MacCurdy, R. Katzschmann, Y. Kim, and D. Rus, “Printable hydraulics: a method for fabricating robots by 3d co-printing solids and liquids,” in *Robotics and Automation (ICRA), 2016 IEEE International Conference on*, pp. 3878–3885, IEEE, 2016.
- [13] A. M. Hoover and R. S. Fearing, “Fast scale prototyping for folded millirobots,” in *Robotics and Automation, 2008. ICRA 2008. IEEE International Conference on*, pp. 886–892, Ieee, 2008.
- [14] M. Salerno, K. Zhang, A. Menciassi, and J. S. Dai, “A novel 4-dof origami grasper with an sma-actuation system for minimally invasive surgery,” *IEEE Transactions on Robotics*, 2016.
- [15] E. Vander Hoff, D. Jeong, and K. Lee, “Origamibot-i: A thread-actuated origami robot for manipulation and locomotion,” in *2014 IEEE/RSJ International Conference on Intelligent Robots and Systems*, pp. 1421–1426, IEEE, 2014.

- [16] Y. Mulgaonkar, B. Araki, J.-s. Koh, L. Guerrero-Bonilla, D. M. Aukes, A. Makineni, M. T. Tolley, D. Rus, R. J. Wood, and V. Kumar, “The flying monkey: A mesoscale robot that can run, fly, and grasp,” in *2016 IEEE International Conference on Robotics and Automation (ICRA)*, pp. 4672–4679, IEEE, 2016.
- [17] C. D. Onal, R. J. Wood, and D. Rus, “An origami-inspired approach to worm robots,” *IEEE/ASME Transactions on Mechatronics*, vol. 18, no. 2, pp. 430–438, 2013.
- [18] K. Zhang, C. Qiu, and J. S. Dai, “Helical kirigami-enabled centimeter-scale worm robot with shape-memory-alloy linear actuators,” *Journal of Mechanisms and Robotics*, vol. 7, no. 2, p. 021014, 2015.
- [19] C. D. Onal, M. T. Tolley, R. J. Wood, and D. Rus, “Origami-inspired printed robots,” *IEEE/ASME Transactions on Mechatronics*, vol. 20, no. 5, pp. 2214–2221, 2015.
- [20] M. Agheli, S. G. Faal, F. Chen, H. Gong, and C. D. Onal, “Design and fabrication of a foldable hexapod robot towards experimental swarm applications,” in *2014 IEEE International Conference on Robotics and Automation (ICRA)*, pp. 2971–2976, IEEE, 2014.
- [21] S. T. Kalat, S. G. Faal, U. Celik, and C. D. Onal, “Tribot: A minimally-actuated accessible holonomic hexapedal locomotion platform,” in *Intelligent Robots and Systems (IROS), 2015 IEEE/RSJ International Conference on*, pp. 6292–6297, IEEE, 2015.
- [22] S. Felton, M. Tolley, E. Demaine, D. Rus, and R. Wood, “A method for building self-folding machines,” *Science*, vol. 345, no. 6197, pp. 644–646, 2014.
- [23] S. G. Faal, F. Chen, W. Tao, M. Agheli, S. Tasdighikalat, and C. D. Onal, “Hierarchical kinematic design of foldable hexapedal locomotion platforms,” *Journal of Mechanisms and Robotics*, vol. 8, no. 1, p. 011005, 2016.
- [24] L. L. Howell, *Compliant mechanisms*. John Wiley & Sons, 2001.

- [25] L. U. Odhner and A. M. Dollar, “The smooth curvature flexure model: An accurate, low-dimensional approach for robot analysis,” *Proc. Robot.: Sci. Syst. VI*, pp. 137–144, 2010.
- [26] C. Sung and D. Rus, “Foldable joints for foldable robots,” *Journal of Mechanisms and Robotics*, vol. 7, no. 2, p. 021012, 2015.
- [27] A. M. Mehta and D. Rus, “An end-to-end system for designing mechanical structures for print-and-fold robots,” in *2014 IEEE International Conference on Robotics and Automation (ICRA)*, pp. 1460–1465, IEEE, 2014.
- [28] U. Saranli, M. Buehler, and D. E. Koditschek, “Rhex: A simple and highly mobile hexapod robot,” *The International Journal of Robotics Research*, vol. 20, no. 7, pp. 616–631, 2001.
- [29] S. M. Salapaka and M. V. Salapaka, “Scanning probe microscopy,” *IEEE Control Systems*, vol. 28, no. 2, pp. 65–83, 2008.
- [30] D. Rugar and P. Hansma, “Atomic force microscopy,” *Physics today*, vol. 43, no. 10, pp. 23–30, 1990.
- [31] Q. Yu and F. Zhi-jing, “Simulation and experiment of nano-positioning compliant mechanism for motion reduction,” *Nanotechnology and Precision Engineering*, vol. 5, no. 1, 2007.
- [32] D. E. Soltero, B. J. Julian, C. D. Onal, and D. Rus, “A lightweight modular 12-dof print-and-fold hexapod,” in *2013 IEEE/RSJ International Conference on Intelligent Robots and Systems*, pp. 1465–1471, IEEE, 2013.
- [33] L. L. Howell, S. P. Magleby, and B. M. Olsen, *Handbook of compliant mechanisms*. John Wiley & Sons, 2013.
- [34] L. L. Howell and J. N. Leonard, “Optimal loading conditions for non-linear deflections,” *International journal of non-linear mechanics*, vol. 32, no. 3, pp. 505–514, 1997.
- [35] L. L. Howell and A. Midha, “Parametric deflection approximations for end-loaded, large-deflection beams in compliant mechanisms,” *Journal of Mechanical Design*, vol. 117, no. 1, pp. 156–165, 1995.

- [36] T. E. Shoup and C. W. McLarnan, “On the use of the undulating elastica for the analysis of flexible link mechanisms,” *Journal of Engineering for Industry*, vol. 93, no. 1, pp. 263–267, 1971.
- [37] C. Kimball and L.-W. Tsai, “Modeling of flexural beams subjected to arbitrary end loads,” *Journal of Mechanical Design*, vol. 124, no. 2, pp. 223–235, 2002.
- [38] G. L. Holst, G. H. Teichert, and B. D. Jensen, “Modeling and experiments of buckling modes and deflection of fixed-guided beams in compliant mechanisms,” *Journal of Mechanical Design*, vol. 133, no. 5, p. 051002, 2011.
- [39] K. Bisshopp and D. Drucker, “Large deflection of cantilever beams,” *Quarterly of Applied Mathematics*, vol. 3, no. 3, pp. 272–275, 1945.
- [40] A. Banerjee, B. Bhattacharya, and A. Mallik, “Large deflection of cantilever beams with geometric non-linearity: Analytical and numerical approaches,” *International Journal of Non-Linear Mechanics*, vol. 43, no. 5, pp. 366–376, 2008.
- [41] A. Zhang and G. Chen, “A comprehensive elliptic integral solution to the large deflection problems of thin beams in compliant mechanisms,” *Journal of Mechanisms and Robotics*, vol. 5, no. 2, p. 021006, 2013.
- [42] A. Saxena and S. Kramer, “A simple and accurate method for determining large deflections in compliant mechanisms subjected to end forces and moments,” *Journal of Mechanical Design*, vol. 120, no. 3, pp. 392–400, 1998.
- [43] K. Mattiasson, “Numerical results from large deflection beam and frame problems analysed by means of elliptic integrals,” *International journal for numerical methods in engineering*, vol. 17, no. 1, pp. 145–153, 1981.
- [44] H.-J. Su, “A load independent pseudo-rigid-body 3r model for determining large deflection of beams in compliant mechanisms,” *Proceedings of ASME IDETC/CIE (43260)*, pp. 109–121, 2008.

- [45] Y.-Q. Yu, S.-K. Zhu, Q.-P. Xu, and P. Zhou, “A novel model of large deflection beams with combined end loads in compliant mechanisms,” *Precision Engineering*, vol. 43, pp. 395–405, 2016.
- [46] Y.-Q. Yu, Z.-L. Feng, and Q.-P. Xu, “A pseudo-rigid-body 2r model of flexural beam in compliant mechanisms,” *Mechanism and Machine Theory*, vol. 55, pp. 18–33, 2012.
- [47] H.-J. Su, “A pseudorigid-body 3r model for determining large deflection of cantilever beams subject to tip loads,” *Journal of Mechanisms and Robotics*, vol. 1, no. 2, p. 021008, 2009.
- [48] V. K. Venkiteswaran and H.-J. Su, “A three-spring pseudorigid-body model for soft joints with significant elongation effects,” *Journal of Mechanisms and Robotics*, vol. 8, no. 6, p. 061001, 2016.
- [49] A. Midha, S. G. Bapat, A. Mavanthoor, and V. Chinta, “Analysis of a fixed-guided compliant beam with an inflection point using the pseudo-rigid-body model concept,” *Journal of Mechanisms and Robotics*, vol. 7, no. 3, p. 031007, 2015.
- [50] C. A. Mattson, L. L. Howell, and S. P. Magleby, “Development of commercially viable compliant mechanisms using the pseudo-rigid-body model: case studies of parallel mechanisms,” *Journal of Intelligent Material Systems and Structures*, vol. 15, no. 3, pp. 195–202, 2004.
- [51] G. Chen, B. Xiong, and X. Huang, “Finding the optimal characteristic parameters for 3r pseudo-rigid-body model using an improved particle swarm optimizer,” *Precision Engineering*, vol. 35, no. 3, pp. 505–511, 2011.
- [52] I. A. Ramirez, *Pseudo-Rigid-Body Models for Approximating Spatial Compliant Mechanisms of Rectangular Cross Section*. University of South Florida, 2014.
- [53] T. Hill and A. Midha, “A graphical, user-driven newton-raphson technique for use in the analysis and design of compliant mechanisms,” *Journal of Mechanical Design*, vol. 112, no. 1, pp. 123–130, 1990.

- [54] R. Miller, “Numerical analysis of a generalized plane elastica,” *International Journal for Numerical Methods in Engineering*, vol. 15, no. 3, pp. 325–332, 1980.
- [55] R. P. Chase Jr, R. H. Todd, L. L. Howell, and S. P. Magleby, “A 3-d chain algorithm with pseudo-rigid-body model elements,” *Mechanics Based Design of Structures and Machines*, vol. 39, no. 1, pp. 142–156, 2011.
- [56] N. Tolou and J. Herder, “A seminanalytical approach to large deflections in compliant beams under point load,” *Mathematical Problems in Engineering*, vol. 2009, 2009.
- [57] L. Campanile and A. Hasse, “A simple and effective solution of the elastica problem,” *Proceedings of the Institution of Mechanical Engineers, Part C: Journal of Mechanical Engineering Science*, vol. 222, no. 12, pp. 2513–2516, 2008.
- [58] R. Frisch-Fay, “Applications of approximate expressions for complete elliptic integrals,” *International Journal of Mechanical Sciences*, vol. 5, no. 3, pp. 231–235, 1963.
- [59] L. V. King, *On the direct numerical calculation of elliptic functions and integrals*. Cambridge University Press, 2016.
- [60] P. F. Byrd and M. D. Friedman, *Handbook of elliptic integrals for engineers and physicists*, vol. 67. Springer, 2013.
- [61] J. E. Shigley, *Shigley’s mechanical engineering design*. Tata McGraw-Hill Education, 2011.
- [62] P. G. Forrest, *Fatigue of metals*. Elsevier, 2013.
- [63] A. Whelan and J. Craft, *Developments in Plastics Technology?3*. Springer Science & Business Media, 2012.
- [64] J. Sauer and G. Richardson, “Fatigue of polymers,” *International journal of fracture*, vol. 16, no. 6, pp. 499–532, 1980.
- [65] W. Glaeser, *Materials for tribology*, vol. 20. Elsevier, 1992.

- [66] K. R. Chandran, “Mechanical fatigue of polymers: A new approach to characterize the s n behavior on the basis of macroscopic crack growth mechanism,” *Polymer*, vol. 91, pp. 222–238, 2016.
- [67] DuPont, “Dupont kapton summary of properties,” 2017.
- [68] R. L. Norton, *Design of machinery: an introduction to the synthesis and analysis of mechanisms and machines*. McGraw-Hill Professional, 2004.
- [69] R. C. Juvinall and K. M. Marshek, *Fundamentals of machine component design*, vol. 83. John Wiley & Sons New York, 2006.
- [70] G. N. Vanderplaats, *Numerical optimization techniques for engineering design: with applications*, vol. 1. McGraw-Hill New York, 1984.
- [71] M. Gen and R. Cheng, *Genetic algorithms and engineering optimization*, vol. 7. John Wiley & Sons, 2000.
- [72] S. S. Rao and S. S. Rao, *Engineering optimization: theory and practice*. John Wiley & Sons, 2009.
- [73] L. L. Howell and A. Midha, “A method for the design of compliant mechanisms with small-length flexural pivots,” *Journal of mechanical design*, vol. 116, no. 1, pp. 280–290, 1994.

Appendix A

Optimized Parameters of MinIAQ Mechanism

A.1 MinIAQ-I Optimization

Input Parameters:

$$\begin{array}{llll} J_1J_2 = 20.3 \text{ mm} & J_2E = 22.15 \text{ mm} & EI = 2.18 \text{ mm} & \\ EF = 24.85 \text{ mm} & J_1H = 29.76 \text{ mm} & GH = 5.15 \text{ mm} & GI = 6 \text{ mm} \end{array}$$

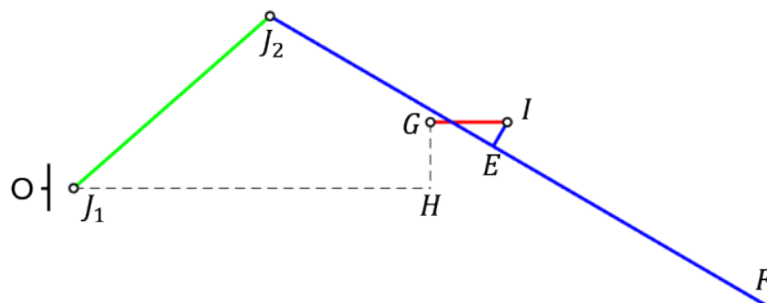


Figure A.1: Input mechanism of MinIAQ-1.

$$lb = \{3 \ 0.7 \ 3 \ 0.7\} \text{ mm}$$

-lower bounds

$$ub = \{6 \ 15 \ 6 \ 15\} \text{ mm}$$

-upper bounds

$x_0 = \{3.1 \ 1 \ 3.1 \ 1\}$ mm	-initial values
$t = 75 \mu\text{m}$	-thickness
$E = 2.5 \text{ GPa}$	-Youngs Modulus
$\sigma_u = 231 \text{ MPa}$	-Ultimate Tensile Strength
$\sigma_e = 50 \text{ MPa}$	-Endurance Limit
$Fy = 10 \text{ gram}$	-Maximum Load

Optimized Parameters:

$AH = 30.253 \text{ mm}$	$GH = 5.150 \text{ mm}$	$BC = 19.195 \text{ mm}$	
$DE = 21.538 \text{ mm}$	$DF = 46.388 \text{ mm}$	$EI = 2.180 \text{ mm}$	$GI = 6 \text{ mm}$

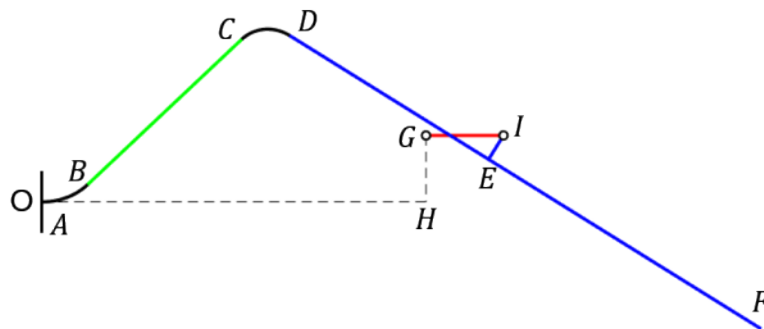


Figure A.2: Optimized compliant mechanism of MinIAQ-1.

$w_1 = 6 \text{ mm}$	$L_1 = 0.987 \text{ mm}$	-Joint 1 Parameters
$w_2 = 6 \text{ mm}$	$L_2 = 1.223 \text{ mm}$	-Joint 2 Parameters

A.2 MinIAQ-II Optimization

Input Parameters:

$J1J2 = 25.05 \text{ mm}$	$J2E = 19.20 \text{ mm}$	$EI = 2.18 \text{ mm}$	
$EF = 34.90 \text{ mm}$	$J1H = 34.76 \text{ mm}$	$GH = 5.15 \text{ mm}$	$GI = 5.1 \text{ mm}$

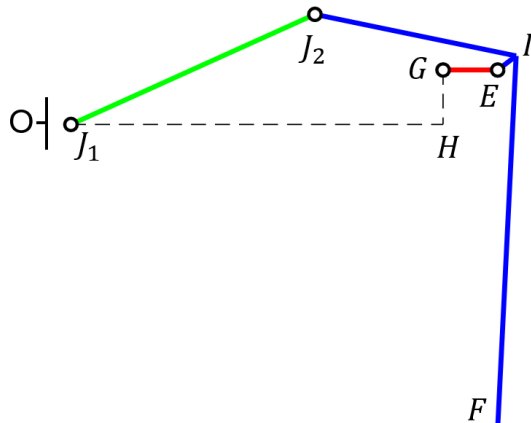


Figure A.3: Input mechanism of MinIAQ-2.

$lb = \{3 \ 0.7 \ 3 \ 0.7\}$ mm	-lower bounds
$ub = \{6 \ 15 \ 6 \ 15\}$ mm	-upper bounds
$x0 = \{3.1 \ 1 \ 3.1 \ 1\}$ mm	-initial values
$t = 75 \ \mu\text{m}$	-thickness
$E = 2.5 \ \text{GPa}$	-Youngs Modulus
$\sigma_u = 231 \ \text{MPa}$	-Ultimate Tensile Strength
$\sigma_e = 50 \ \text{MPa}$	-Endurance Limit
$Fy = 10 \ \text{gram}$	-Maximum Load

Optimized Parameters:

$AH = 35.110 \ \text{mm}$	$GH = 5.150 \ \text{mm}$	$BC = 24.093 \ \text{mm}$	
$DE = 18.593 \ \text{mm}$	$EF = 34.900 \ \text{mm}$	$EI = 2.180 \ \text{mm}$	$GI = 5.10 \ \text{mm}$

$w_1 = 5.797 \ \text{mm}$	$L_1 = 0.700 \ \text{mm}$	-Joint 1 Parameters
$w_2 = 5.797 \ \text{mm}$	$L_2 = 1.214 \ \text{mm}$	-Joint 2 Parameters

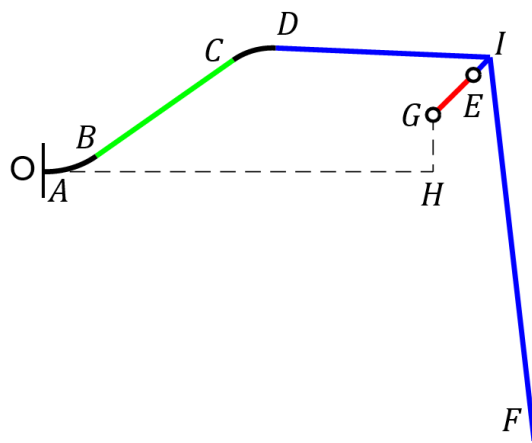


Figure A.4: Optimized compliant mechanism of MinIAQ-2.